University of Catania

Department of Civil Engineering and Architecture

National Doctoral Course in Defense Against Natural Risks and Ecological Transition of Built Environment

XXXVIII Cycle

PhD thesis

GETI: GEological-geoTechnical Index for Natural Risks Assessment with a Multi-Hazard Approach, Applied to Linear Infrastructure

PhD student: Nadia Salvatore

November 30, 2025

Supervisor: Prof. Alessandro Pagliaroli[2]

Co-supervisors: Prof. Kyle Rollins[3], Prof. Giuseppe Brando[2], Prof. Alberto Pizzi[2], Prof. Sara Amoroso[2]

Doctoral Course Coordinator: Prof. Massimo Cuomo[1]

[1]University of Catania - Department of Civil Engineering and Architecture

[2]University “G. d’Annunzio” of Chieti-Pescara – Department of Engineering and Geology

[3]Brigham Young University of Provo (UT) - Department of Civil and Construction Engineering

ABSTRACT

This thesis introduces the Geological-Geotechnical Index (GETI), a novel tool for multi-hazard risk assessment of linear infrastructures, particularly road and highway bridges and viaducts. GETI employs a Probabilistic Graphical Model (PGM), combining Bayesian Network (BN) and Fault Tree Analysis (FTA) to evaluate seismic hazards and their secondary effects. The index considers earthquakes as the primary hazard, with secondary effects including landslides/rockfall, soil liquefaction/lateral spreading, and ground shaking. These secondary hazards are treated as acting simultaneously on structures, with distinguishable and non-overlapping effects. The hybrid BN-FTA model allows for the maintenance of effect independence and the application of conditional probability to calculate expected structural damage during seismic events. GETI is not a risk index in sensu stricto, as it uses a fixed earthquake scenario based on prescribed peak ground acceleration or acceleration response spectra associated with a selected return period. The index aims to provide infrastructure managers with an effective tool for assessing seismic risk from a multi-hazard perspective and establishing priorities for mitigation actions. Two case studies were used to test GETI's functionality: a viaduct in Avezzano, Italy, and the Cherry Hill Interchange in Farmington, Utah, USA. These studies demonstrated the index's applicability under different conditions and knowledge levels, as well as its sensitivity to changing ground conditions. The case studies revealed that GETI can effectively highlight individual hazard contributions to total earthquake-induced damage, allowing for easy identification of predominant impacts on structures. The index also proved capable of quantifying damage probability reductions resulting from vulnerability mitigation interventions. Limitations of the current GETI formulation include its applicability only to seismic hazards and the assumption of independent damaging effects acting simultaneously. Future developments aim to address these issues and extend the index to a true multi-hazard context. Despite these limitations, GETI achieves its goal of determining expected damage percentages during earthquakes while accounting for secondary effects. The index provides an effective tool for network managers to assess seismic risk and prioritize mitigation actions for linear infrastructure.

LIST OF ABBREVIATIONS

B

BEM	Boundary Element Method
BN	Bayesian Network

C

CIDH	Cast-In-Drilled-Hole
CISS	Cast-In-Situ
CPT	Cone Penetration Test
CRM	Complex Response Method
CRR	Cyclic Resistance Ratio
CSR	Cyclic Stress Ratio
CTI	Compound Topographic Index

D

DPT	Dynamic Penetration Test
DSHA	Deterministic Seismic Hazard Analysis
DTM	Digital Terrain Model

E

EAD	Expected Annual Damage
EAL	Expected Annual Losses
EDP	Engineering Demand Parameters
EL	Equivalent Linear
EMKZ	Extended Modified Konder-Zelasko model
ESA	Effective Stress Analysis
ETR	Energy Transfer Ratio

F

FD	Frequency Domain
FDM	Finite Difference Method
FE	Finite Element
FEM	Finite Element Method
FS	Safety Factor
FTA	Fault Tree Analysis

G

GETI	Geological-geoTechnical Index
GM	Ground Motion
GWT	Ground Water Table

H

HS	Hazard Score

I

IM	Intensity Measure

L

L	Landslides
LDI	Lateral Displacement Index
LiDAR	Light Detection And Ranging
LPI	Liquefaction Potential Index
LQ	Soil liquefaction
LS	Lateral spread

M

MKZ	Modified Konder-Zelansko model
MR	Masing Rules
MRDF	Modulus Reduction and Damping Curve Fitting
MSF	Magnitude Scaling Factor

N

NEHRP	National Earthquake Hazards Reduction Program
NL	Non-Linear
NMR	Non Masing Rules

P

PDF	Probability Density Function
PGA	Peak Ground Acceleration
PGD	Permanent Ground Displacement
PGM	Probabilistic Graphical Model
PSHA	Probabilistic Seismic Hazard Analysis

R

R	Rockfall
RC	Reinforced Concrete
RVT	Random Vibration Theory

S

S	Ground seismic motion
SLV	Ultimate Limit State
SoVI	Social Vulnerability Index
SPT	Standard Penetration Test

T

TD	Time Domain
TE	Top Event
TSA	Total Stress Analysis

U

UIUC	University of Illinois at Urbana-Champaign

W

WFZ	Wasatch Fault Zone

NOTATION

C

C_U	Coefficient of uniformity

D

D_h	Horizontal displacement
D_H	Damage derived from horizontal displacement
δ_{LQ}	Expected value of liquefaction-induced vertical settlements
D_{LQ}	Damage derived from liquefaction-induced vertical settlements
δ_L	Expected value of landslide-induced horizontal displacement
δ_{LS}	Expected value of liquefaction-induced lateral spreading
δ_R	Expected value of falling block velocity
D_r	Relative density
D_R	Damage derive from rockfall impact
δ_S	Expected value of PGA
D_S	Damage derived from ground shaking

G

G/G_0	Normalized shear stiffness

K

K_σ	Overburden correction factor

M

M_0	Seismic Moment
m_b	Body-wave Magnitude (short period)
m_B	Body-wave Magnitude (long period)
M_L	Local Magnitude (Richter)
M_S	Surface-wave Magnitude
M_W	Moment Magnitude

N

$(\mathrm{N}_1)_{60}$	Normalized standard penetration test blow count
$(\mathrm{N}_1)_{60cs}$	Normalized standard penetration test equivalent clean sand blow count
N_{DPT}	Dynamic penetration test blow count
N_{spt}	Standard penetration test blow count

P

P_L	Probability of liquefaction

Q

q_{c1N}	Normalized cone penetration test blow count
$(\mathrm{q}_{c1N})_{cs}$	Normalized cone penetration test equivalent clean sand blow count

R

r_d	Shear stress reduction coefficient
R_e	Epicentral Distance

S

σ_v	Total vertical stress
σ_v'	Effective vertical stress

V

V_S	Shear-wave Velocity

INDEX

1. INTRODUCTION

The assessment of risk from natural hazards on linear infrastructure, such as road and highway bridges and viaducts, represents a complex challenge for professionals in the field, due both to the unpredictable nature of the phenomena and the need for a multidisciplinary approach. Regulations currently in force in Italy and abroad tend to use risk analysis models that evaluate each hazard individually, in a generic way and without taking into account the possibility of interactions between phenomena. In recent years, however, several studies have highlighted and described the phenomenon of the "cascading effect", in which the occurrence of a primary hazard triggers further events, secondary hazards, which can interact with each other in ways that may aggravate or mitigate their impacts on the built environment. Natural hazards such as earthquakes, landslides, and floods cause significant damage to the global transport network every year, both in terms of direct structural damage and in terms of economic losses resulting from disruptions to freight and routine transport services. In this context, a proper risk assessment of linear infrastructures, carried out from a multi-hazard perspective and thus accounting for interactions among hazards present in a given area, emerges as a necessity, enabling proper planning for mitigation interventions and optimizing resources by reducing both costs and damages.

Starting from these considerations and the study of cascading effects in a multi-hazard analysis framework, still limited to natural phenomena, this research project decided to focus on the development of a geological-geotechnical index, GETI, for the assessment of risk from natural hazards on road and highway bridges and viaducts. Due to the complexity of a multi-hazard approach that also considers cascading effects, the index's development focused exclusively on seismic risk and its secondary effects. This allowed for the creation of a statistical model that is sufficiently simple to be understood and validated through selected case studies, to be used as a starting point for developing, in the future and with further studies, a general model that truly serves as a multi-hazard analysis tool, taking into account all possible primary hazards and the secondary hazards that may be triggered by them. The main objective in developing this index is to provide road and highway network managers with an effective tool for assessing the likelihood of natural hazards and their possible effects on linear structures, enabling them to prioritize and plan mitigation measures, with potential savings in economic resources, while also taking into account secondary effects that, with currently used methodologies, are not considered.

This work is part of the Italian national Doctorate course in Defense Against Natural Risks and Ecological Transition of Built Environment, XXXVIII cycle, and aims to develop new defense strategies against natural hazards, specifically to be applied to linear infrastructure. Considering the lack of a multi-hazard approach in current regulations, the index was developed to account for possible interactions among natural hazards, rather than simply overlaying single risk assessments carried out for each macro-group of phenomena.

The thesis is organized into five chapters, with the first serving as an introduction to the work carried out. The second chapter, which is mainly bibliographic in nature, presents a state of the art review of risk indices and multi-hazard concepts, both in general and as applied to linear structures, culminating in the definitions of risk, multi-hazard, vulnerability, and exposure that are later used in the development of GETI. Additionally, this chapter aims to show the knowledge gap that the research underpinning this thesis seeks to address, the existing foundations it builds upon, and the aspects in which it is innovative. The third chapter, which is the core of the thesis, illustrates the logical flow of GETI and all the methods used to arrive at the definition of the index itself and the statistical model that represents it. Furthermore, it provides the methods present in the literature and considered most suitable for Level 1 screening and Level 2 analyses. The fourth chapter, dedicated to discussion and conclusions, summarizes the fundamental aspects of the work and highlights its strengths as well as unresolved issues, referring possible solutions and future extensions to later developments.

2. LITERATURE REVIEW

2.1. Concept of Multi-Hazard

Since the GETI index is based on the theoretical framework of Multi-Hazard, it is crucial to provide a clear definition of this term. Additionally, it is important to specify that this work focuses solely on natural hazards.

2.1.1. General Definitions

The term “hazard” has been described by UNISDR (2009) as a *dangerous phenomenon, substance, human activity or condition that may cause loss of life, injury or other health impacts, property damage, loss of livelihoods and services, social and economic disruption, or environmental damage*. The Intergovernmental Panel on Climate Change (IPCC) (IPCC, 2022), defined “hazard” as *the potential occurrence of a natural or human-induced physical event or trend that may cause loss of life, injury, or other health impacts, as well as damage and loss to property, infrastructure, livelihoods, service provision, ecosystems and environmental resources*.

Following this, a definition of “natural hazards” may be a *natural process or phenomenon that may cause loss of life, injury or other health impacts, property damage, loss of livelihoods and services, social and economic disruption, or environmental damage*, considering natural hazards as a sub-set of all hazards (UNISDR, 2009). The term encompasses both dangerous events and the conditions that might cause them in the future, covering a broad spectrum of physical phenomena like earthquakes, tsunamis, landslides, floods, volcanic eruptions, and more (Gill and Malamud, 2014).

Natural hazard events are characterized by their magnitude or intensity, the speed at which they occur, their duration, and the area they impact. According to the classification by the Integrated Research on Disaster Risk (IRDR) program of the International Council of Science (ICSU), these events can be divided into six categories: Geophysical hazards, which include phenomena like earthquakes, landslides, and tsunamis, are hazards originating from the solid earth or geological processes; Hydrological hazards, which result from the presence, movement, and distribution of both surface and underground freshwater and saltwater, encompass events such as avalanches and floods; Meteorological hazards are associated with short-term, small- to medium-scale extreme weather and atmospheric conditions that can last from minutes to several days; Climatological hazards are linked to long-term, medium- to large-scale atmospheric processes involving climate variability over periods ranging from intra-seasonal to multi-decadal; Biological hazards include outbreaks of diseases and infestations by insects or animals; Extraterrestrial hazards are caused by asteroids, meteoroids, and comets as they approach Earth, enter its atmosphere, or impact the planet, as well as changes in interplanetary conditions that affect Earth's magnetosphere, ionosphere, and thermosphere. (ICSU, 2012; Gill and Malamud, 2014). They can be categorized as either rapid onset events, such as earthquakes, flash floods, and landslides, or slow onset phenomena, like sea level rise, increasing temperatures, and droughts (Tosun and Howlett, 2021).

2.1.2. Multi-hazard Overview

When addressing multiple hazards simultaneously, the term "multi-hazard" is frequently employed, as noted in Kappes et al. (2011, 2012). This bibliographic review seeks to provide a comprehensive definition of the term and has been extensively utilized in this section of the thesis. From this, an initial definition emerged: the "all-hazards-at-a-place" concept, which involves identifying all potential hazards (Hewitt and Burton, 1971). This encompasses all natural or man-made conditions that could potentially cause damage to exposed assets within a specified area.

The notion of "multi-hazard" first appeared in the United Nations Agenda 21 for sustainable development (UNCED, 1992) and was later defined by Kappes (2011) as *the totality of relevant hazards in a defined area*. Here, "relevant" refers to hazardous processes that inflict a certain level of damage, contingent on the area's specific geological and social conditions, the study's focus, and the infrastructure's significance and characteristics. Conversely, a hazard causing damage below a certain threshold is deemed insignificant. Greiving et al. (2006) expanded on this by defining "relevant" hazardous processes as those with a significant likelihood of occurring in the designated area. In this context, events with an extremely low probability of occurrence, such as meteorite impacts, are excluded. Over the past decade, the limitations of studies that focus solely on a single hazard have been highlighted (e.g., Kappes et al., 2012; Gill and Malamud, 2014). Indeed, when various hazards interact, their combined impact can surpass the effects of each hazard when considered individually. Therefore, hazards should be viewed not as isolated processes but as multiple interconnected ones, recognizing that, in certain cases, one hazard may trigger or interact with other hazardous phenomena (e.g., rockfalls or liquefaction induced by seismic activity) (Gill and Malamud, 2014; Zaghi et al., 2016).

Gill and Malamud (2014) undertook an extensive global literature review to clarify the potential interactive relationships among twenty-one natural hazards, which they categorized into six groups: geophysical, hydrological, shallow Earth, atmospheric, biophysical, and space hazards. Through this process, they developed a Hazard Interaction Matrix by considering four distinct interaction categories: those where a hazard is triggered (cascade effect), those that increase the probability of a hazard, those that decrease the probability of a hazard, and events involving the spatial and temporal coincidence of natural hazards (e.g., an earthquake occurring during a strong rainstorm; while these events are not causally linked, their simultaneous occurrence represents a multi-hazard scenario).

The authors assembled global evidence into a 21 x 21 matrix (Fig. 2.1) that highlights 90 interactions among natural hazards out of a possible 441. These interactions encompass both triggered relationships and scenarios where one hazard heightens the likelihood of another. The matrix's vertical axis lists the primary hazards (rows 1 to 21, EQ to IM), which are the initial hazards that either trigger or modify the probability of another hazard occurring. The horizontal axis displays these same hazards as potential secondary hazards (columns A to U, EQ to IM), representing the hazards that are either triggered or have an increased probability of occurring. Each cell in the matrix is divided diagonally into two triangles. Shading in the upper-left triangle of a cell indicates that the primary hazard might trigger the secondary hazard.

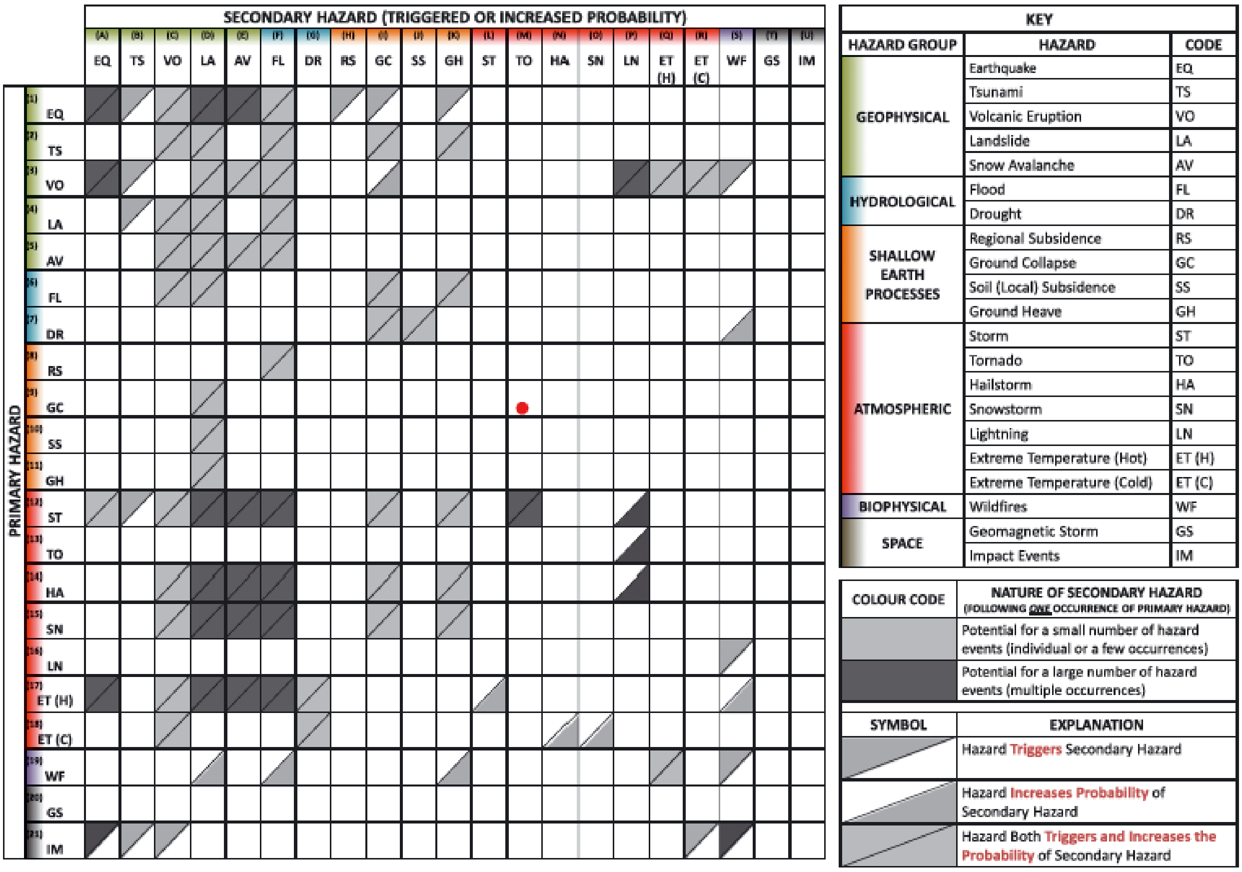

Fig. 2.1: Identification of interactions between hazards involves a 21 × 21 matrix, where primary hazards are listed vertically and secondary hazards horizontally. These hazards are coded as detailed in the key. The matrix highlights instances where a primary hazard might trigger a secondary hazard (upper left triangle shaded) and where it might increase the likelihood of a secondary hazard occurring (bottom-right triangle shaded). If both triangles are shaded, it signifies that the primary hazard can both trigger and raise the probability of a secondary hazard. Additionally, relationships are categorized based on whether a primary hazard can trigger or heighten the probability of multiple occurrences of a secondary hazard (dark grey) or just a few or single occurrences (light grey). Hazards are classified into geophysical (green), hydrological (blue), shallow Earth processes (orange), atmospheric (red), biophysical (purple), and space/celestial (grey). Footnotes provide more details on some of these relationships (Gill and Malamud, 2014).

In a given cell, shading the lower-right triangle indicates that the primary hazard may increase the likelihood of the secondary hazard. Both triangles can be shaded for a single primary-secondary hazard pair. Among the 90 interactions identified in this 21 × 21 matrix, 63 (70%) represent scenarios where a primary hazard can trigger and elevate the probability of a secondary hazard, 15 (17%) where a primary hazard can trigger but not increase the likelihood of a secondary hazard, and 12 (13%) where a primary hazard can increase the probability of a secondary hazard without triggering it. Light-grey shading suggests that the primary hazard might trigger only a few instances of the secondary hazard. For example, a landslide might trigger just one tsunami, and a volcanic eruption might lead to a single episode of climatic change. Dark-grey shading indicates that the main hazard has the capacity to initiate numerous secondary hazards (multiple instances). For instance, an earthquake, intense storm, or snowmelt event might lead to thousands of separate landslides. It is noted that 66 (73%) out of the 90 interactions are likely to result in a small number of hazard events (individual or a few instances), while 24 (27%) have the potential to cause a large number of hazard events (multiple instances). According to the authors, a limitation of the visualization presented in Figure 2.1 is its restriction to scenarios where a single primary hazard leads to one or more secondary hazards. The matrix is not designed to handle situations where two primary hazards combine to initiate or heighten the likelihood of a secondary hazard, such as when drought and lightning occur simultaneously, increasing the risk of wildfires.

In addition to using Figure 2.1 to demonstrate how natural hazards can interact, with one event triggering another, it can also be employed to identify a network of hazard interactions similar to a cascade effect. This means that a series of hazards are triggered sequentially or simultaneously due to successive triggering processes. By examining Figure 2.1, one can trace the row of the initial primary hazard to uncover potential secondary hazards. Each of these secondary hazards can then be considered as the next primary hazard, capable of triggering further (tertiary) hazards. This analysis of potential cascade or domino effects can assist in conducting a comprehensive hazard assessment and determining possible mitigation strategies. When a primary hazard occurs, it alters environmental parameters across various parts of the geosystem, such as the atmosphere, biosphere, lithosphere, and hydrosphere. These changes in environmental parameters, including pore-water pressures, soil shear strength, surface water discharge, atmospheric aerosol concentration, confining pressures, and ground elevation above sea level, can increase the likelihood of a specific secondary hazard or push it past a critical threshold, thereby triggering it. The term "mechanism" is used here to describe the process by which a primary hazard induces environmental changes that either trigger a secondary hazard or heighten its probability. For example, as depicted in Figure 2.1, an earthquake (row 1, EQ) can trigger a landslide (column D, LA) by causing seismic shaking that alters the soil's shear stress and strength, leading to mass movement due to gravitational forces.

Given that the matrix is derived from empirical data, the authors themselves acknowledged that the analysis might not be comprehensive and may not fully capture the actual effects a primary hazard can have on the environment and, consequently, on other hazards. For instance, consider rows 12 (ST) and 17 (ET(H)) versus column A (EQ) in Figure 2.1: it is well-established in the literature (Yeats et al., 1997; Kramer and Stewart, 2025) that endogenous phenomena, such as earthquakes, cannot be influenced by exogenous events, like extreme weather conditions such as storms or high ground temperatures. This observation highlights a poor characterization of these correlations, indicating a lack of information and case studies, which could explain the authors' error in considering endogenous phenomena as being triggered or enhanced by exogenous ones. Despite this, the work by Gill and Malamud (2014) remains a valuable resource for understanding the complexity of interactions between natural hazards.

The interactions between hazards have been classified by several authors, such as Tilloy et al. (2019) and Wang et al. (2020). The first study categorizes the interconnections between hazards into five distinct types: Independence, where hazards occur simultaneously without any interdependence or triggering effects; Triggering (cascading), where a primary hazard initiates secondary hazards; Change conditions, where one hazard alters the state of another by modifying environmental conditions; Compound hazards (association), which involve different hazards arising from the same primary event but not as primary and secondary hazards; and Mutual exclusion (negative dependence), where two natural hazards may show negative dependence or be mutually exclusive, such as heavy rain and fire. A similar classification was proposed by Wang et al. (2020), dividing hazards into three categories: Mutually amplified, which includes natural hazards that trigger technological emergencies, human-induced, disaster chain, and domino effect; Mutually exclusive; and Non-influential. It is interesting to consider the definition of mutually amplified natural hazards as a “disaster chain,” in which one or more primary hazards (called “parent disasters”) lead to the occurrence of secondary hazards. These concepts were well synthesized by López-Saavedra and Martì (2023) in the following diagram (Fig. 2.2).

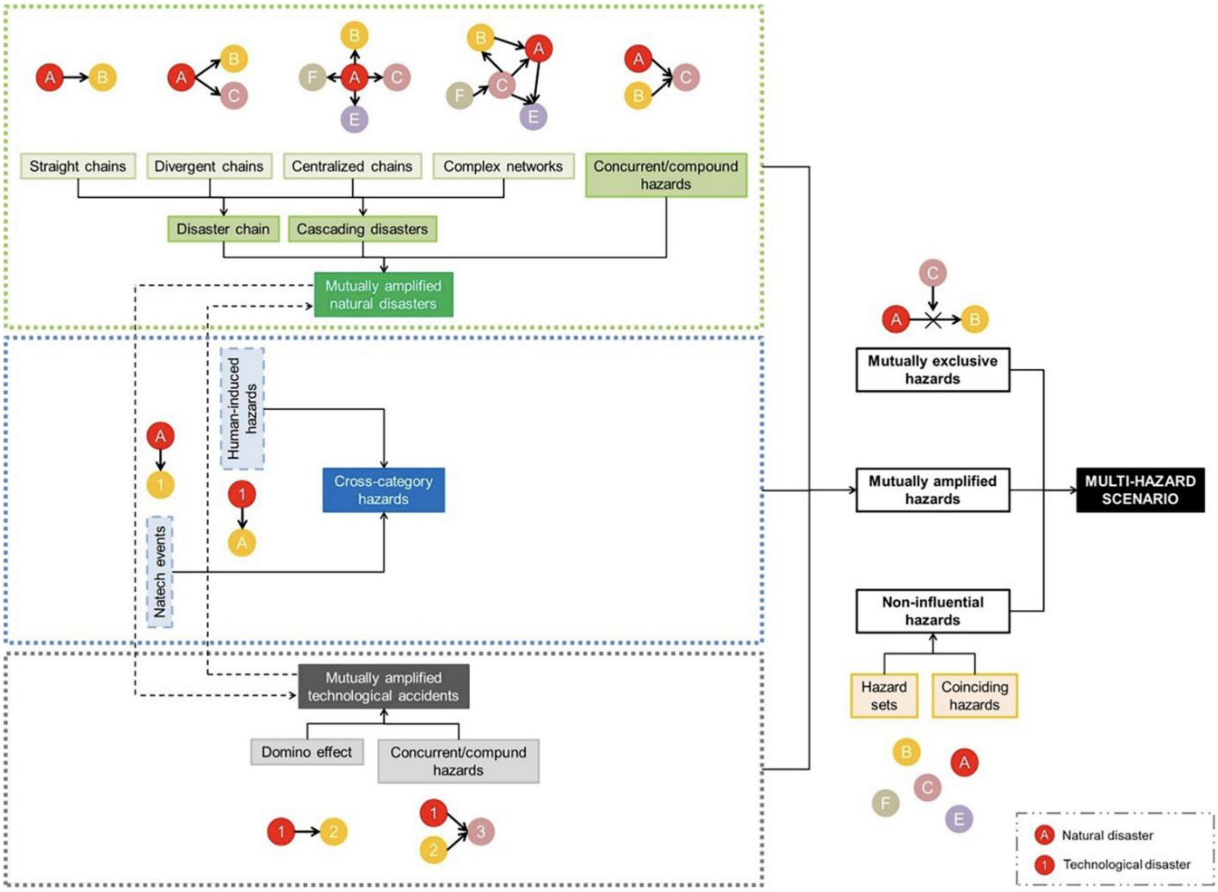

Fig. 2.2: Schematic representation of the existing terminology for hazard relationships by López-Saavedra and Martì (2023).

In this classification, the concept of multi-hazard is linked to the existence of a network (chain, tree or complex) that can describe the relationships between hazards, giving a useful model for analyze a multi-hazard scenario from a statistical point of view (e.g., Bayesian Network, Fault Tree analysis).

2.2. Multi-hazard Risk Assessment at the Regional Scale

2.2.1. Definitions

Another fundamental step in structuring the GETI index was the definition of the concept of risk applied to linear structure in multi-hazard view. Following the UNISDR Report (UNISDR, 2017), the term "Risk" can be defined as *the combination of the probability of an event and its negative consequences.* In the IPCC Report (IPCC, 2022), risk is defined as *the potential for adverse consequences for human or ecological systems, recognizing the diversity of values and objectives associated with such systems*. Another interesting definition for this term was proposed by Greiving at al. (2006), considering risk as *the likelihood of occurrence (or probability) of a hazard, which is defined by (a) the potential sources of risk (e.g. industrial, flooding, transportation) and the contextual nature of the risk itself (high or low consequence); and (b) a probabilistic estimate based on the* *frequency of occurrence (e.g. 100-year flood, 5% risk)*. Given this, the "Risk assessment" can be defined as *a methodology to determine the nature and extent of risk by analyzing potential hazards and evaluating existing conditions of vulnerability that together could potentially harm exposed people, property, services, livelihoods and the environment on which they depend* (UNISDR, 2017).

This definition introduces other two important terms to in unambiguously define: vulnerability and exposure. "Vulnerability" can be defined as *the degree of fragility of a (natural or socio-economic) system or community towards natural and technological hazards.* (Greiving et al., 2006), while the "Exposure" could be defined as *the presence of people; livelihoods; species or ecosystems; environmental functions, services and resources; infrastructure; or economic, social or cultural assets in places and settings that could be adversely affected* (IPCC, 2022). Therefore, the risk analysis process must encompass: an examination of the technical aspects of hazards, including their location, intensity, frequency, and likelihood; an assessment of exposure and vulnerability, taking into account the physical, social, health, economic, and environmental factors; and an appraisal of the effectiveness of existing and alternative coping strategies in relation to potential risk scenarios (UNISDR, 2017).

Following the logical framework established by Marzocchi et al. (2012), the task of quantifying and comparing risks, especially when they may interact, is inherently challenging, making it a complex area of study. The primary difficulty arises from methodological issues; for example, risk assessments for various sources are typically conducted independently, with differing methods and resolutions in terms of time and space. In most instances, only qualitative estimates of risk levels are available. This approach to risk evaluation has significant limitations: firstly, comparing risks from different sources is challenging, if not impossible; secondly, assuming risk sources are independent overlooks potential interactions among threats and the so-called "cascade" effects. In practice, this implies that a potential multi-hazard risk index could exceed the simple sum of individual risk indices calculated by treating each source as independent. According to the author, multi-hazard risk assessment aims to tackle these two issues by employing a consistent time-space framework, a uniform metric for evaluating losses, and considering potential interactions among hazards, both in terms of probabilistic hazard and vulnerability. Another challenge for multi-hazard risk assessment, which it shares with traditional risk analysis, stems from epistemological issues related to the nature of scientific knowledge. For instance, risk assessment involves integrating complex concepts such as hazard source identification and assessment, and vulnerability evaluation; each concept carries implicit assumptions and modeling methodologies that can propagate uncertainties, which should not be ignored but must be coherently integrated into the final assessment. Lastly, another obstacle for multi-hazard risk assessment is the lack of a common terminology among scientists from different disciplines; in some cases, scientists dealing with various types of risks assign different meanings to the same term (Marzocchi et al., 2012).

2.2.2. Qualitative Indices

Continuing in consideration of the regional/local scale, risk assessment in multi-hazard framework can be intended both as qualitative and quantitative measure. The first case encompasses the National Risk Index, developed by the U.S. Department of Homeland Security (FEMA, 2023), which is defined as the product of the Expected Annual Loss (EAL) and the Social Vulnerability Index (SoVI), divided by the community resilience score. This index, even if qualitative, attempts to quantify the impact of all natural hazards that can impact the United States region related to social vulnerability, also indented as the resilience of infrastructure. The vulnerability of linear infrastructure, such as road bridges/viaducts, is considered in this more extensive concept and has not been analyzed in detail.

According to the methodology proposed by FEMA, the composite EAL value is determined by combining the EALs values for each hazard type. A composite Risk Index can be calculated using the same methodology as the composite EAL, normalizing the EAL, SoVI, and community resilience scores to a range from 0 (lowest possible value) to 100 (highest possible value) to facilitate their combination (Zuzak et al., 2022). Subsequently, a composite, multi-hazard risk index score is computed, representing the risk of a community for all hazard types, relative to all other communities at the same level, expressed in a five-category qualitative rating, ranging from ”very low” to ”very high”.

2.2.3. Quantitative Indices

To make a step over, quantitative indices can be considered. In this approach, the output data of the natural risk assessment is not a superimposition of the warning classes derived for each phenomenon, but a quantification in mathematical terms of the impact of natural hazards on a certain region, considering the vulnerability of structures to each hazard. An example is the hazard score (HS) proposed by Odeh (2002) for risk assessment from a multi-hazard perspective. The index considers each individual hazard that could affect a given area and quantifies it through the average number of events per year (frequency score), percentage of subregions or the average impact in square miles of the event considered (scope score), and level of intensity (intensity score).

The HS is calculated using the following equation:

$$HS = F \cdot S \cdot I \tag{2.1}$$

where F is the frequency score; S the scope score; I the intensity score.

To compute the multi-hazard score, the HS values calculated for each identified hazard in the area were aggregated. The resulting HS is a continuous measure owing to the multiplicity of the classified input scores. One limitation of this approach is that it does not provide information on the spatial distribution of hazards or risks to communities at this level. Furthermore, this method considers only multiple hazards as the sum of the individual hazards.

A few years later, Dilley et al. (2005) proposed a simple multi-hazard index composed of single-hazard analyses. Hazards were investigated through the integration of historical event data and modeling techniques. The final index value is derived from the sum of the individual hazard indices, which falls within the range of 8 to 10. The limitation of this index value is the fact that it is a semi-quantitative one, because the risk is expressed in warning classes, even if the analysis is conducted using a statistical approach and natural hazards are deducted from historical data. However, the hazard spatial distribution is considered, even if the contribution of each phenomenon is not connected to the others.

The probability of occurrence of an hazard that can be triggered or enhanced by another hazard is traying to be converted into equations by Marzocchi et al. (2012), starting with the assumption that, in case of two hazards occurs at the same time in an given area, vulnerability can be considered as the probability of occurrence of the hazard 1 given the hazard 2, as in equation:

$$H_1 = p(E_1) = p(E_1|E_2)p(E_2) + p(E_1|\overline{E_2})p(\overline{E_2}) \tag{2.2}$$

where $\overline{E_2}$ represent the case of not occurring of the hazard 2. The total risk is determined by multiplying the annual probability of occurrence associated with a hazard that may trigger or exacerbate the initial hazard, vulnerability (calculated as the expected damage multiplied by the average number of buildings damaged at that level), and exposure (the probability of casualties among people living inside the building), with each risk calculated separately. As the authors themselves point out, the analysis was confined to the interaction between two hazards due to the complexities involved in the calculations. Furthermore, this approach provides the risk value for each hazard that may occur in a specific area, rather than a cumulative risk associated with all potential hazards.

In summary, quantitative indices offer a continuous standardization of diverse and not directly comparable parameters, allowing for the quantification of differences between hazard levels rather than merely ranking them, as is the case with qualitative indices. This approach, while still limited to addressing hazards individually, helps overcome one of the limitations of qualitative indices.

2.3. Multi-hazard Risk Assessment at the Infrastructure Scale

Shifting focus from a regional perspective to the infrastructure scale, it becomes essential to define key terms differently, given that this research primarily concentrates on linear infrastructure, such as bridges and viaducts, for both roads and railways. In this context, *Risk* refers to the likelihood of an adverse event impacting transportation facilities, thereby affecting the performance of the transportation system according to the agency's objectives. In bridge management, the primary concern is the potential failure of the bridge to function as anticipated (NCHRP, 2016). The relevance of risk assessment in linear infrastructure is well demonstrated in literature (e.g., Koks et al., 2019). Transport infrastructure are exposed to natural hazards all over the world, as it is highlighted in Figure 2.3. It is possible to notice that the most part of the industrialized and emerging countries are struggling with an extensive exposure of their transport infrastructure to natural hazards.

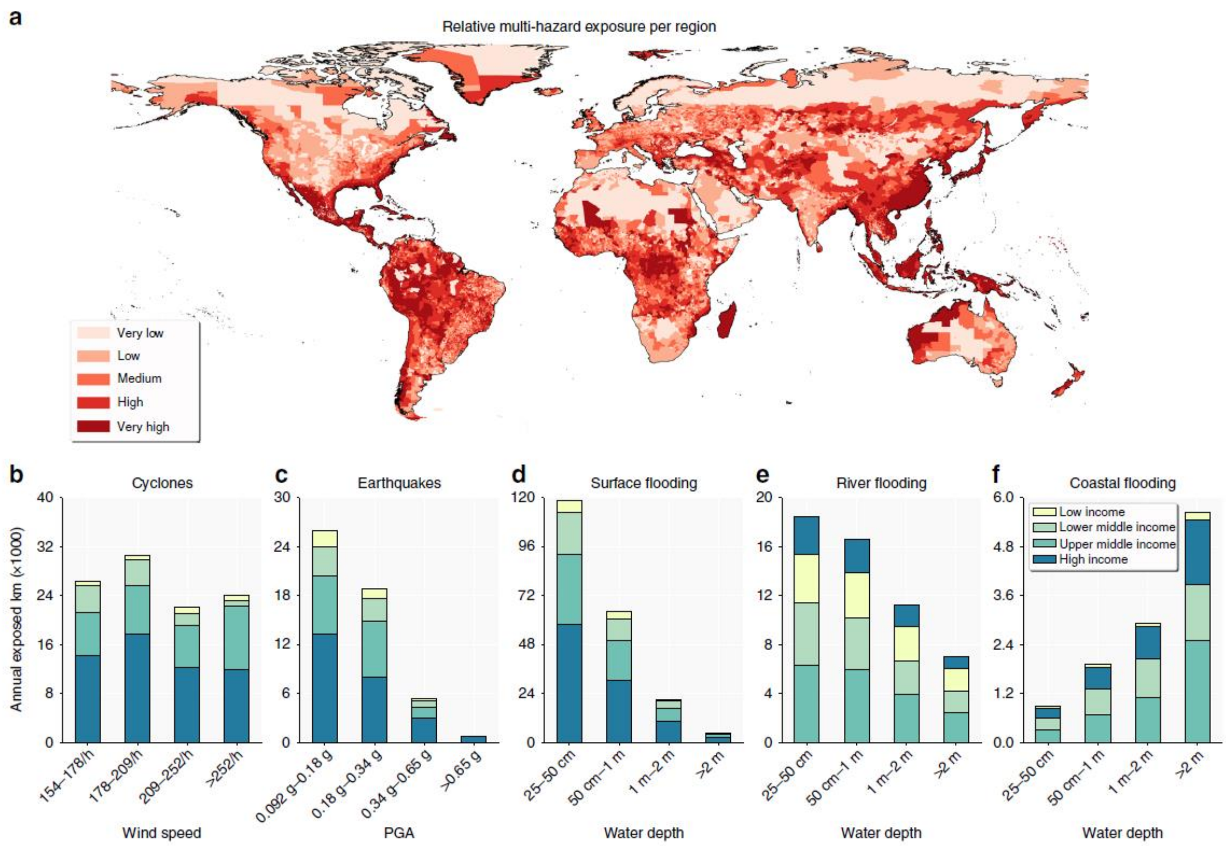

Fig. 2.3: Global multi-hazard transport infrastructure exposure. Panel a illustrates the exposure levels for each global region, categorized by 20th percentiles. Panels b–f depict the exposure for the four income groups, broken down by hazard type and intensity band (from Koks et al., 2019).

The occurrence of natural hazards can lead to significant economic losses, as estimated by Koks et al. (2019). These estimates focus on the direct consequences of damage to roads and railways, excluding losses from transport delays, fatalities, and the cascading effects on the local economy. Consequently, the authors estimate that the Expected Annual Damage (EAD) from natural hazards affecting transport infrastructure worldwide ranges from 3.1 to 22 billion USD.

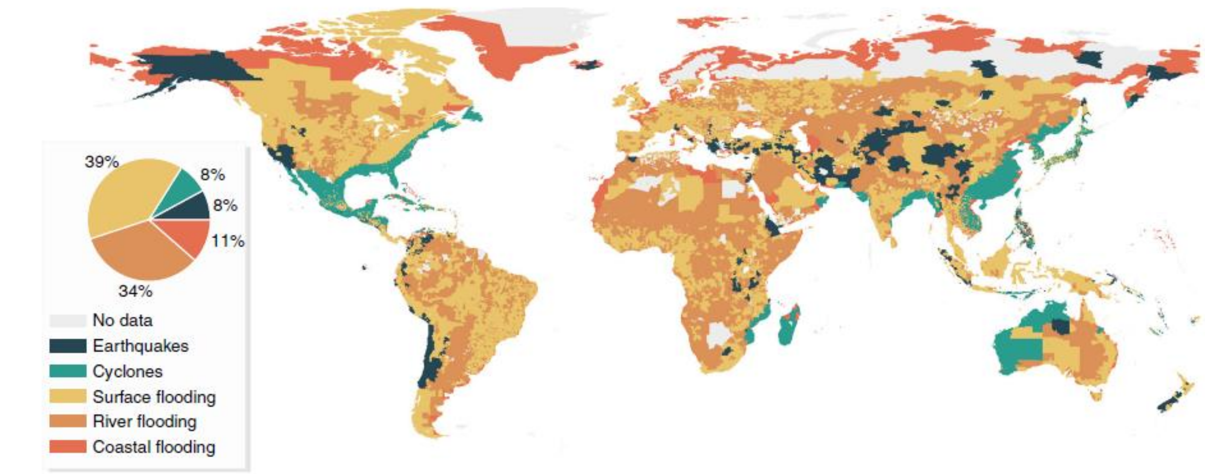

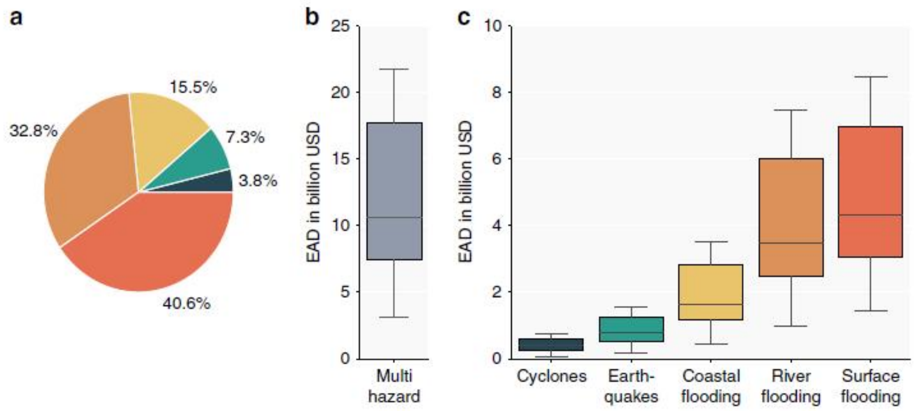

Fig. 2.4. The upper part of the figure shows the location of the hazards causing the highest transport infrastructure exposure in each region; the pie chart shows the relative percentage of land area, excluding areas with insufficient data, where that specific hazard causes the highest exposure. a) relative distribution of the total EAD to infrastructure assets among the different hazards; b) calculated range of total multi-hazard global EAD; c) calculated range of the EAD per hazard. The lower and upper whiskers in b) and c) represent, respectively, the lowest 25% of the calculated EAD's and the highest 25% of the calculated EAD's (from Koks et al., 2019).

Figure 2.4a illustrates the predominant hazard in each region. It is crucial to note that, in most cases, two or more hazards can occur simultaneously or trigger one another, thereby amplifying the damage effects. Figure 2.4b presents the distribution of EAD values categorized by different types of hazards. In this study, the concept of "multi-hazard" is defined as the total economic loss resulting from the combined effects (understood as the sum) of the considered hazards. The potential loss may be increased by the complex interactions among hazards, underscoring the importance of approaching the issue from a genuine multi-hazard perspective.

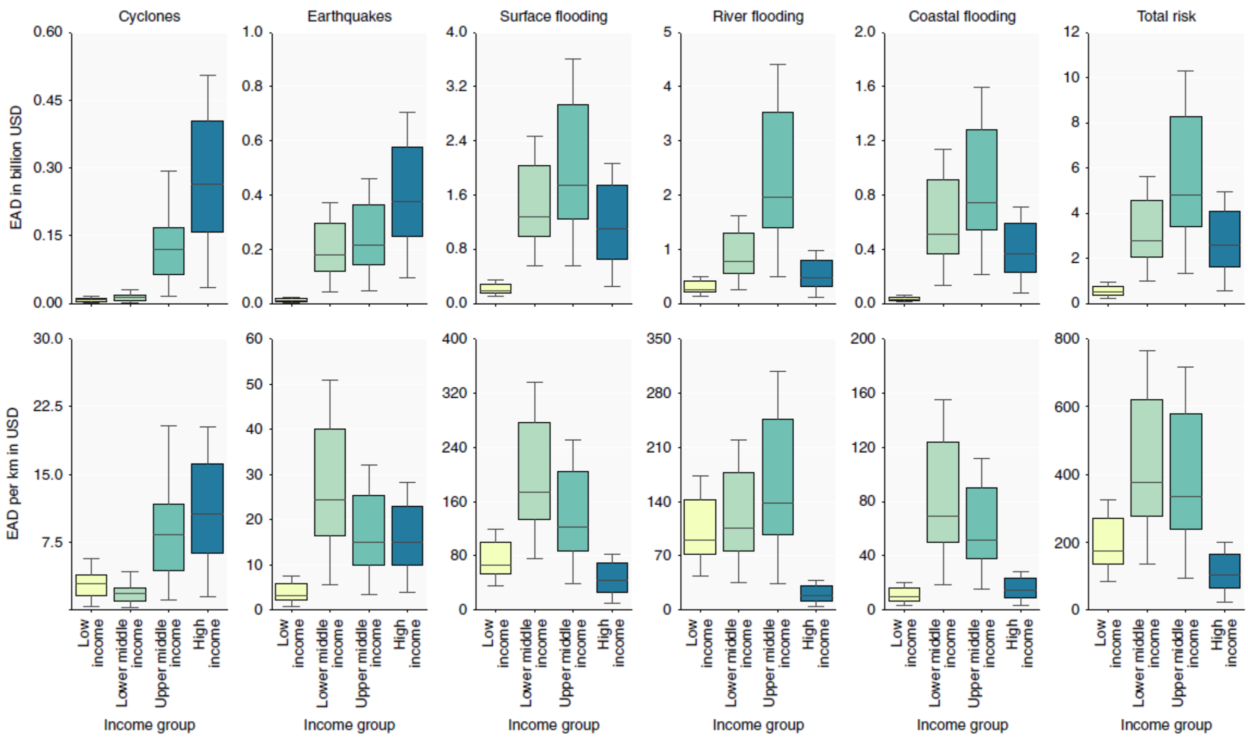

Fig. 2.5. Expected annual damages per hazard. The upper row of boxplots presents the absolute EAD for each individual hazard and, in the right-most boxplot, the total multi-hazard EAD per kilometer. The lower and upper whiskers represent, respectively, the lowest 25% of the calculated EAD's and the highest 25% of the calculated EAD's for each income level (from Koks et al., 2019).

An additional crucial aspect is the impact of earthquake hazards on transport infrastructure. As illustrated in Figures 2.4 and 2.5, earthquakes are among the most significant natural threats to linear infrastructure. However, it is essential to recognize that the secondary effects of earthquakes, such as tsunamis, are not included within the "earthquake" category, which may lead to an underestimation of the total potential loss. Therefore, considering the possible effects of an earthquake not just as the primary hazards (shaking, ground cracks) but also as the cumulative impact of its secondary effects (e.g., liquefaction, landslides), could increase the EAD value and highlight the importance of this hazard in the assessment of natural hazards affecting transport infrastructure.

Within the transport infrastructure system, bridges and viaducts are a critical component. In 2003, the Blue Ribbon Panel on Bridge and Tunnel Security estimated that the total cost of a critical bridge outage due to natural disasters could exceed $10 billion, taking into account the impact on people's lives, job losses, and reconstruction efforts (BRP, 2003). Clearly, proper maintenance of road bridges and viaducts, along with thorough risk assessment, is essential. Additionally, prioritizing safety measures and maintenance is crucial for the cost-effective management of linear infrastructure (FHWA, 2009; Hwang et al., 2001).

2.3.1. Qualitative Indices

Considering this evidence, multi-hazard risk assessment in linear infrastructure presents a relatively new challenge for decision-makers. Consequently, governments worldwide have developed guidelines to standardize procedures in such studies. In this context, the Italian Guidelines for risk classification and management, safety assessment, and structural health monitoring of existing bridges, established by the Ministero delle Infrastrutture e delle Mobilità Sostenibili (MIMS, 2022), serve as an example of a qualitative risk index.

This framework utilizes a multilevel approach consisting of four stages: Level 0 involves a document-based examination of the infrastructure and its surrounding area; Level 1 includes a field survey focused on geological-geomorphological observations of the site, along with an assessment of structural defects and general maintenance conditions; and Level 2 comprises an analysis of the data collected from Levels 0 and 1, resulting in a "warning class" assigned based on five possible qualitative judgments (High, Medium-High, Medium, Medium-Low, and Low, as shown in Fig. 2.7). This classification considers four types of risks—Structural and Foundation Risk, Seismic Risk, Landslide Risk, and Hydraulic Risk—to prioritize infrastructure that requires more detailed analyses for implementing effective mitigation measures.

Each type of risk was assessed independently, incorporating the findings from the defectivity analysis. The primary emphasis is on landslides and hydraulic hazards, while the seismic hazard assessment is confined to a qualitative evaluation based on peak ground acceleration (PGA) and the moment magnitude (M_W) anticipated in the area. Infrastructure classified from "medium" to "high" is subjected to levels 3 and 4, which involve a more detailed evaluation in accordance with the Italian building code (NTC, 2018), and in certain cases, to a level 5, applied exclusively to a specific type of infrastructure. Consequently, the "warning class" derived from Levels 1 and 2 is assessed and revised as necessary, supported by quantitative analyses that incorporate data from new surveys and monitoring activities.

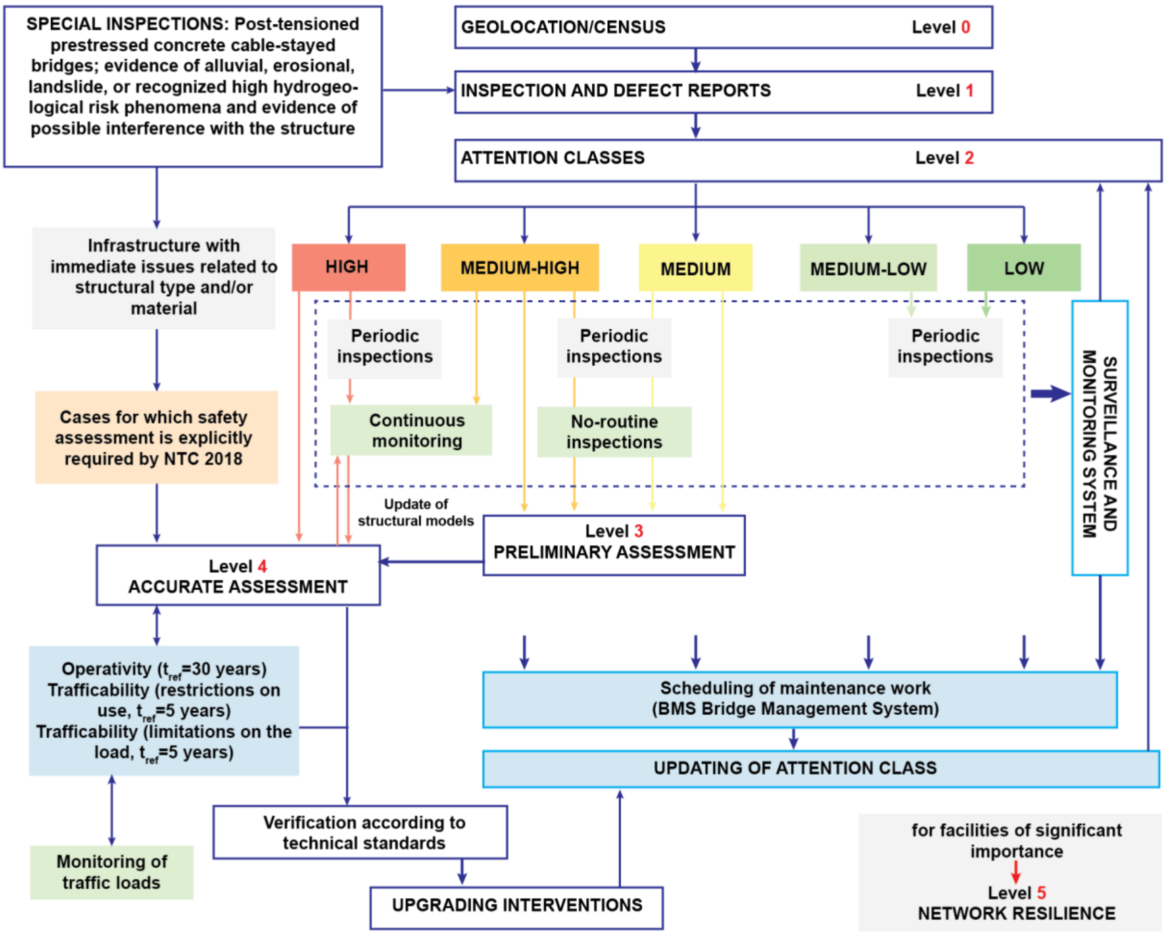

Fig. 2.7. Logic flow chart of the Italian Guidelines for risk classification and management, safety assessment, and monitoring of existing bridges (modified from MIMS, 2022).

In summary, qualitative indices typically establish intensity and frequency thresholds to categorize hazards into a set number of predefined classes. This approach aids in comparing hazards, albeit within a qualitative framework such as "high hazard." Consequently, this methodology enables the creation of hazard maps by overlaying classification results for individual hazards, taking into account the highest hazard class when multiple scenarios of the same or different processes overlap (Kappes et al., 2012).

For instance, the Italian Guidelines for risk classification and management, safety assessment, and monitoring of existing bridges (MIMS, 2022) highlight the shortcomings of this approach. The impact of natural hazards on infrastructure might be underestimated because hydraulic, seismic, and landslide/rockfall hazards are treated as isolated phenomena, without considering the dynamics of the "cascade effect" and, consequently, other hazards that may trigger or influence them. This has become particularly evident in recent decades, as natural hazards stemming from earthquakes and climate change have significantly affected the Italian region. Consider, for example, a road bridge near Rotella (Ascoli Piceno, Italy), which was severely damaged by an earthquake-induced landslide during the 6.5 Norcia earthquake of 2016 and remains inaccessible (CSRS16, 2023). Similarly, a road bridge near Ozzanello (Parma, Italy) collapsed during intense rainfall in October 2023 due to the load from the Sporzana river flood (IRPI, 2023). Furthermore, the analyses of Levels 0, 1, and 2 are largely influenced by the overlap of warning classes related to natural hazards with those related to structural defectivity, obscuring a clear understanding of the potential impact of natural hazards on the structure in question. In essence, in the initial stages of analysis, the structure's behavior under the influence of natural phenomena is not adequately assessed.

2.3.2. Quantitative indices

The risk score in the risk assessment procedure proposed by Highways England in the Design Manual for Roads and Bridges CS450 Inspection of Highway Structures (CS450, 2021) is defined as a semi-quantitative index. Figure 2.8 illustrates the logical flow of the risk assessment for bridges, viaducts, tunnels, and other highway structures. As shown, the objective is to determine the principal inspection interval and, consequently, the maintenance schedule for the structure in question, as previously observed with the Italian guidelines (§2.3.1).

Maintenance inspections are conducted with similar criteria seen before for the Italian national guidelines (§2.3.1), than the risk is defined as:

$$Risk = f(P, S, D, C) \tag{2.3}$$

Where P is the probability or likelihood of an event; S is the severity or consequence of an event; D is the ability to detect a hazard or failure; and C is the ability to control, respond or intervene. The parameters needed for the determination of risk are structure type, environment, inspection/assessment, conditions, and consequences, and they all derived from the data stored by the agencies, including projects and inspections record.

A risk score is proposed as an indicator of relative risk to aid in determining suitable intervals between principal inspections. The risk assessment scoring tables are divided into five categories, each containing several criteria with multiple attribute options, each assigned a score based on the risk level. A lower score indicates a higher risk, while a higher score suggests a lower risk. The risk scores for each category's attributes are summed to produce the actual risk score for that category. In cases where data are unavailable or cannot be obtained, a cautious approach should be taken by using the lowest available score. Consequently, for a structure with numerous unknown variables, it is likely that the recommended interval for principal inspections will remain at 6 years. In all instances where the attribute results in a risk score of “Inspection to remain at 6 years” it signifies that, regardless of the final adjusted risk score, the nature of the attribute necessitates a 6-year interval between principal inspections.

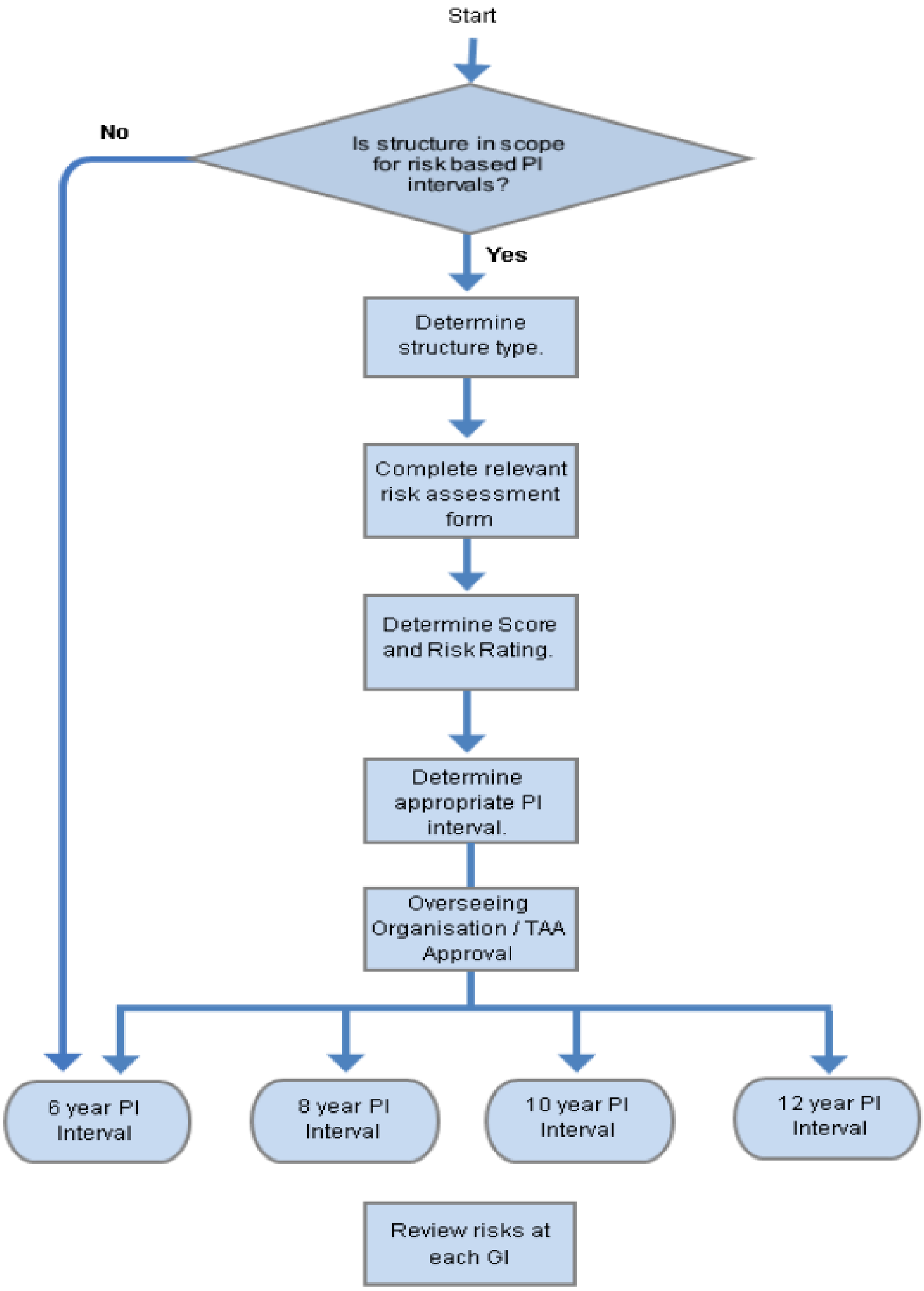

Fig. 2.8. Logic flow of risk assessment in the guidelines for inspection of highway structure (from CS450, 2021)

The risk score (A) for each category is then analyzed against the maximum possible risk score (M) for the category and weighting (W) to produce the adjusted risk score (S) for the particular category, as in Eq. 2.4.

$$S = \frac{A}{M} \cdot W \tag{2.3}$$

Each of the categories are weighted according to their relative importance, as reported in CS450 (2021), Tab. A.8. The sum of the adjusted risk scores (Eq. 2.4) forms the total risk score (T) of between 0 and 100.

$$T = \sum S \tag{2.4}$$

Once the total risk score is calculated, it can be used to determine the risk rating for the structure (high, medium, low, or very low), based on the type of structure (see Tab. from A.14 to A.19 in CS450, 2021). Regarding the Italian guidelines, the main issue lies in Eq. 2.4: the total risk is the sum of the considered risks, derived from individual hazards. This approach does not account for the potential interaction of multiple hazards and their impact on the structure. Another example of a risk index for road bridges is the National Cooperative Highway Research Program (NCHRP) Project 20-07 Task 378 Report, "Assessing Risk for Bridge Management," commissioned by the American Association of State Highway and Transportation Officials (AASHTO) in 2016. In this document, risk assessment is conducted using the AASHTOWare Bridge Management Software. Similar to the Italian guidelines, the first step involves gathering information about the infrastructure and the hazards that may affect it. The logical flow of this approach is illustrated in Figure 2.9.

Once a hazard scenario is established, the agency sets performance criteria, which include condition, cost, safety, mobility, and environmental sustainability. At this stage, the extent of disruption must be factored into the threshold for identifying a hazard scenario, taking into account all hazards assessed in the earlier phase. The probability of service disruption within this framework varies for each bridge, depending on its characteristics, and also changes according to the hazard scenario. Similarly, the impact of service disruption differs with each bridge, influenced by both bridge and network characteristics, and also varies by hazard scenario and performance criterion.

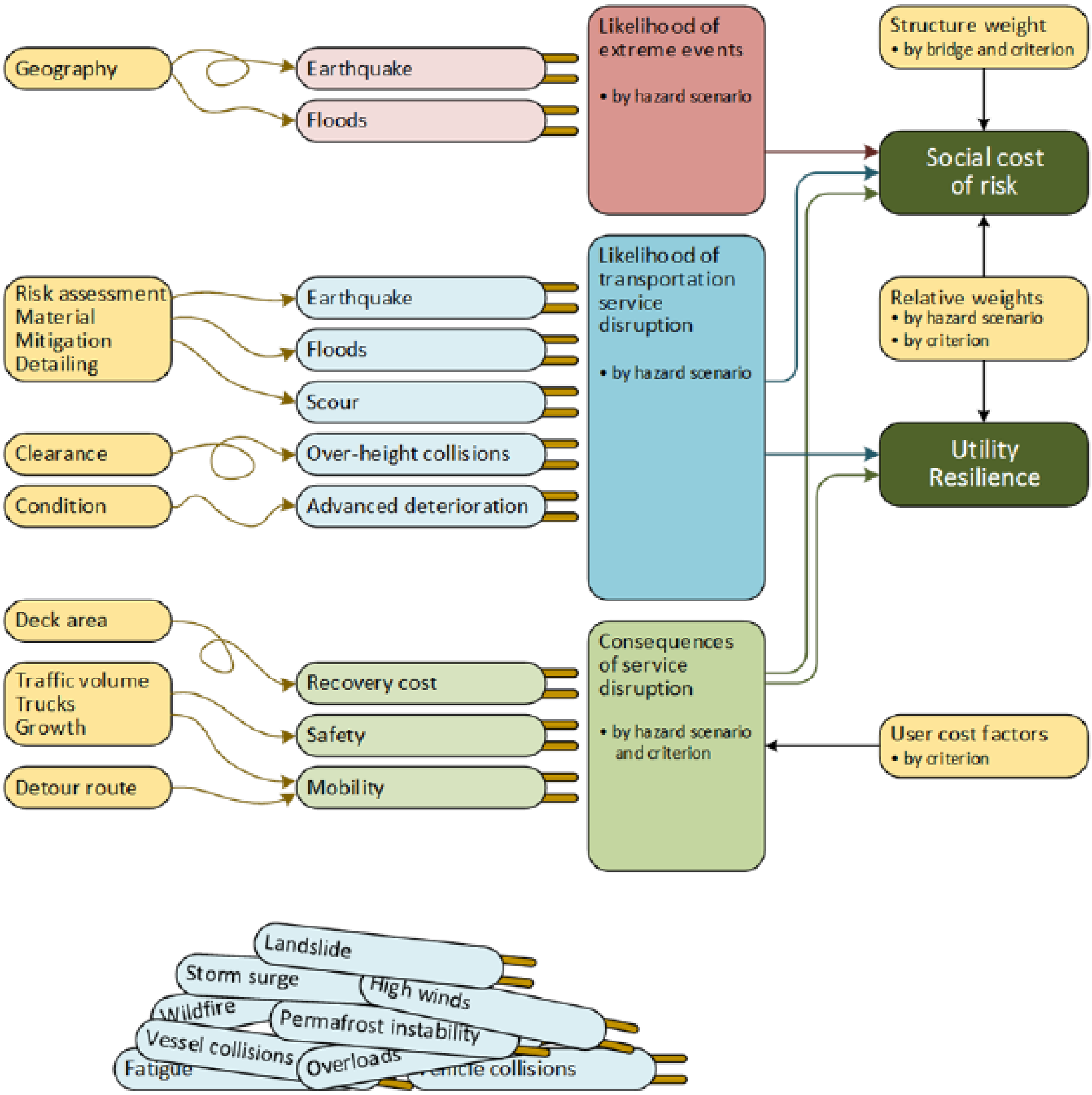

Fig. 2.9: modular approach to the risk assessment methodology proposed by AASHTO (NCHRP, 2016)

The overall probability of hazard scenario h occurring on bridge b is determined by multiplying LE_{bh} by LD_{bh}. Here, LE_{bh} signifies the probability of an extreme event of a specified magnitude, as defined by hazard scenario h, occurring on bridge b. In contrast, LD_{bh} represents the probability of a particular level of service disruption, given that the extreme event described in hazard scenario h has occurred, also estimated for bridge b. These probabilities indicate the likelihood of the described event happening within a single year. While likelihoods are expressed as scalar probabilities, agencies might prefer to categorize them, for instance, as ranges of return intervals. Consequences are quantified economically: CQ_{bhc} represents the consequence, calculated in dollars for each disruption event, related to performance criterion c on bridge b, given the occurrence of the service disruption outlined in hazard scenario h. Consequences vary by hazard scenario and performance criterion. Similar to likelihoods, consequence estimates can also be expressed as ranges.

By taking natural hazards into account, this method requires data acquisition through geographic analysis techniques, such as catalogues and GIS databases available for various extreme natural events, including earthquakes, landslides, high winds, floods, wildfires, and extreme temperatures. For each identified hazard, with the probability of occurrence for a given scenario, AASHTOWare BrM assists in calculating the likelihood of service disruption as a percentage, also considering, when available, the historical record of damage from the specific hazard. At the conclusion of the process, after evaluating the economic and societal impacts of the structure's collapse, the probability of service disruption is used for mitigation planning to adopt cost-effective measures and reduce the likelihood of the structure being severely damaged by the identified hazards. In both CS450 (2021) and NCHRP (2016), it is evident that natural hazards are assessed individually in risk assessments, and their interactions are not evaluated. The potential issues arising from this approach are summarized in the previous paragraph (§ 2.3.1).

3. METHODS

Because of the complexity of the natural system, as highlighted in chapter 2 of this thesis, a simplified approach was adopted to facilitate the development of the GETI index. Consequently, accounting for all primary natural hazards occurred in Italy and reported in historical and geological records (e.g., Fiore and Ottaviani, 2018), only seismic risk is considered in this study, and the susceptibility of a specific area to ground seismic motion amplification (S), soil liquefaction (LQ), landslides (L), and rockfall (R) is evaluated as a secondary effect of an earthquake (e.g., Schnabel et al., 1972; Idriss and Boulanger, 2008; Keefer, 1984).

Thus, GETI index uniquely accounts for the “cascade effect” of seismic hazard and offers a viable method for comprehensively assessing infrastructure exposure. The GETI is based on the multi-hazard concept related to the occurrence of secondary phenomena directly or indirectly related to the primary hazard taken into account (Fig. 3.1).

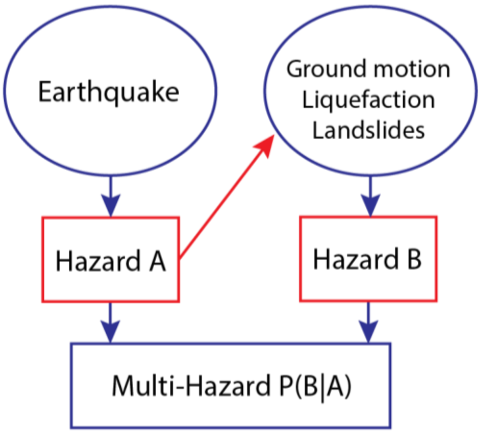

Fig. 3.1. Schematization of the multi-hazard concept, modified from Gill and Malamud (2014)

Thus, the GETI is formulated as the conditional probability of damage to linear infrastructure caused by an earthquake (primary hazard) and its subsequent effects (secondary hazards). This simplification facilitates a more comprehensive understanding of the index's functionality, thereby easing its application to ongoing case studies. Future applications will extend the index to encompass other natural hazards. The GETI is crafted as a quantitative multi-hazard index, conceptualized at two levels of analysis. It can be defined as the probability of damage associated with linear infrastructure, particularly bridges and viaducts. The logical progression leading to the GETI is illustrated in Fig. 3.2:

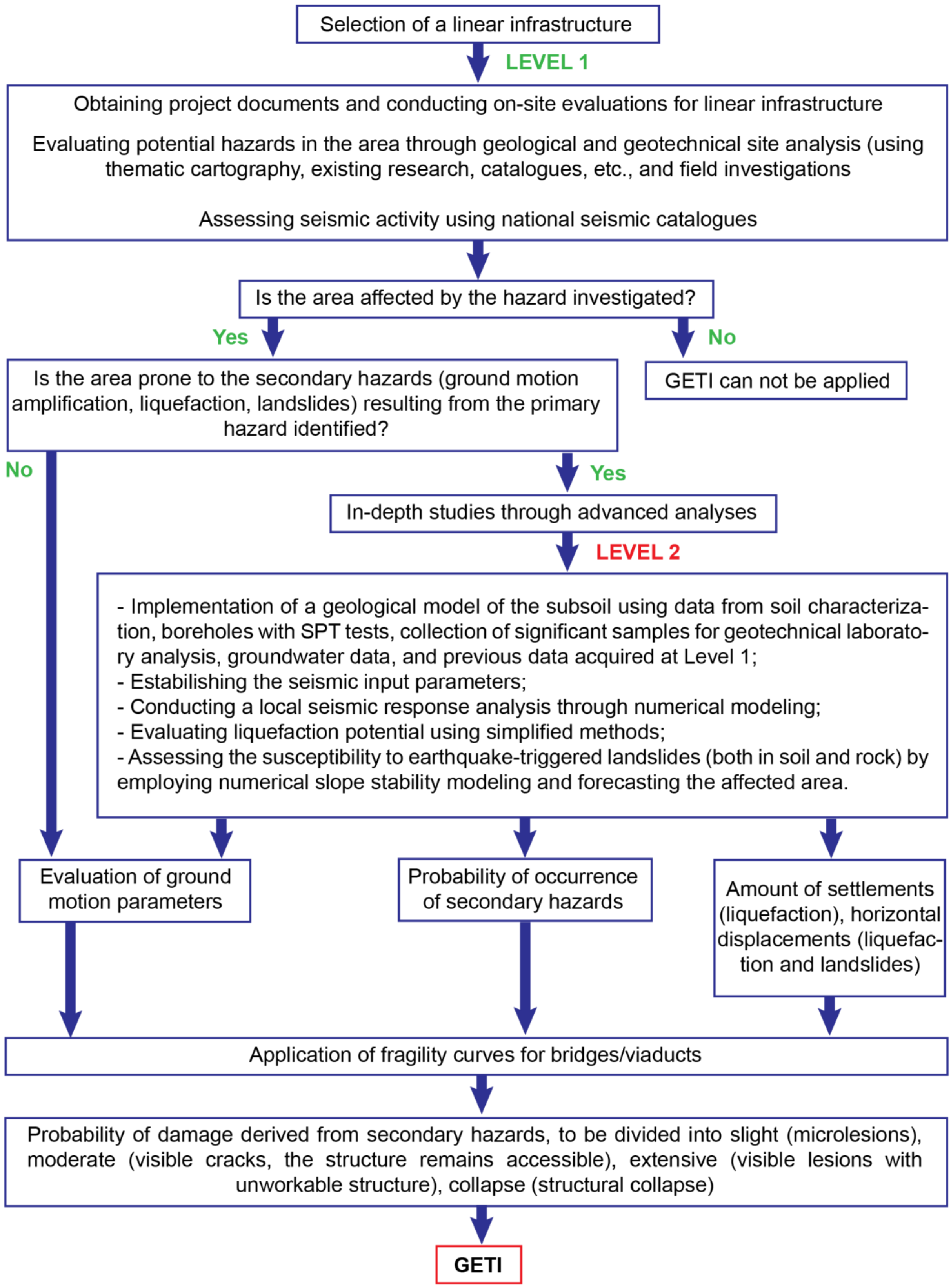

Fig. 3.2. Logic flow of the GETI index considering only its application to seismic risk assessment

3.1. Methods in Analysis: Level 1

The objective of the Level 1 is to acquire all the information and data available from design schemes, geological and seismic catalogues, previous studies conducted in the selected area, and after to verify them, if it is possible, with field surveys. This first level is crucial to create the basic knowledge to correctly approach the in-depth studies in Level 2, and to reduce as much as possible the uncertainty in determination of GETI.

3.1.1. Criteria for applicability of the index

The selection of the liner infrastructure to evaluate is crucial to correctly apply the GETI. In this first simplified version, only road bridges and viaducts are considered, but the application of the index can be extended to other linear structure, such as pipelines, or even dams. The availability of fragility curves developed for the selected structure and the considered hazard is crucial for the applicability of the index.

Because of the structure of the index, the applicability of GETI is directly connected to the availability of information about the structural scheme of the infrastructure and the geological and geotechnical frameworks of the site. The lack of information and data from design schemes, previous studies or catalogues can be compensated by acquiring data directly in Level 2 of analysis. Even if this approach can well supply to the absence of knowledge, it could be very expensive and make the index not so easy to use and effective instrument for stakeholders. So, in the selection of the structure is crucial to consider the balancing between the availability of information and data from previous studies, and the direct acquisition of missing data.

3.1.2. Literature Review and Analysis

From a multi-hazard perspective, the initial level of the logical process for calculating the GETI index aims to examine the susceptibility of a specific area to natural hazards that may impact the linear structure located therein. The first step, Level 1, begins with a thorough review of existing literature, including scientific studies, reports, maps, and other relevant documents. This review aims to identify the potential hazards that threaten the area under consideration, in this case only considering the occurrence of an earthquake and its secondary effects, such as soil liquefaction, ground shaking, landslides.

3.1.2.1. Active faults and earthquakes

Recognizing hazardous conditions in a specific area requires an understanding of the processes that lead to such hazards. Comprehending seismic phenomena involves the plate tectonic theory, which describes the Earth's cold and rigid upper layer, the crust, as being divided into "plates" that move over the asthenosphere due to convective motions. The interactions between these plates, whether convergent, divergent, or strike-slip, create stress at depth, which over geological time causes the crust to deform (e.g., folds) and eventually break (e.g., faults). These phenomena occur not only at the boundaries of major plates but also in intra-plate areas, such as the Somalian rifting, or regions influenced by micro-plates between major plate movements, like Italy (e.g., Twiss and Moores, 2007). The movement of plates results in collisions that elevate mountain chains or divergence that extends and thins the crust until drifting occurs. The stress at depth generates fractures on various scales, from micro to plate boundaries. If sliding occurs along these fractures, regardless of scale, they are termed faults. Fractures and faults form according to the orientation of the stress generated by tectonic movements, providing valuable insights into their geological history.

Faults can be divided in three categories, depending on the orientation of the relative displacement of the two sliding blocks, named hanging-wall and footwall: dip-slip, where the movement is parallel to the dip of the slip surface, which include normal faults (the hanging-wall moves down relative to the footwall) and reverse faults (the hanging-wall moves up relative to the footwall); strike-slip, where the movement is parallel to the strike of the slip surface; oblique-slip, where the movement in oblique to the dip and the strike of the slip surface, as illustrated in Fig. 3.3 (e.g., Twiss and Moores, 2007)).

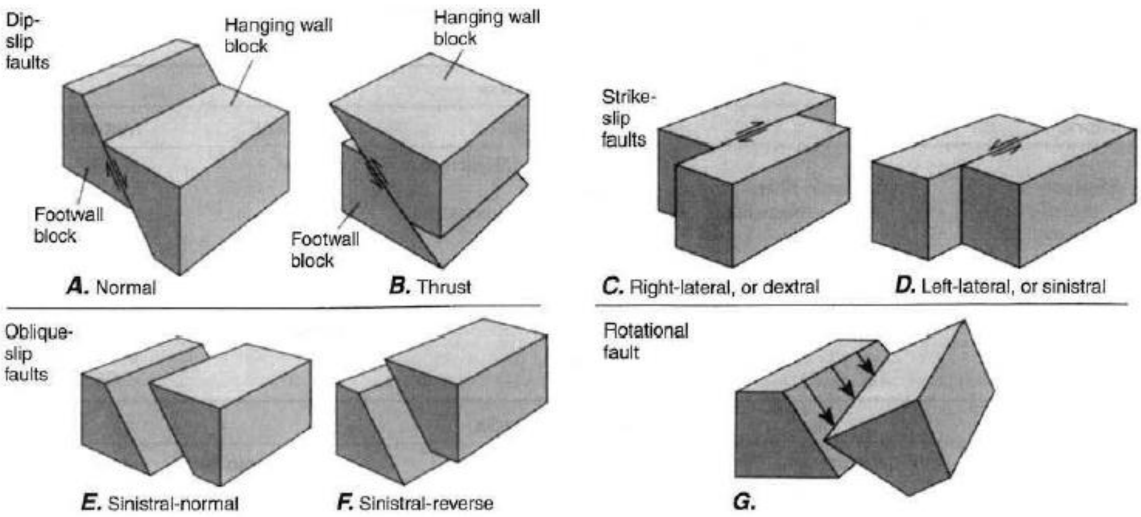

Fig. 3.3. Classification of faults, from Twiss and Moores (2007).

Rocks therefore have the ability to respond to stress fields acting at depth with ductile deformation, until they reach the limit of brittle deformation, thus leading to fracture. An earthquake occurs when the stress-state at depth caused the rupture of a rock block, with the release of the most part of the energy accumulated as elastic strain (Elastic Rebound Theory). This energy is mostly released as heat, and only a small amount is released as seismic body waves, which travel from the breaking point at depth (hypocenter) to the surface. The point upon the ground corresponding to the hypocenter is named epicenter, and faced the maximum value of ground shaking intensity, since the path of the seismic waves is radiant and it means that they energy content will decrease as the distance from the source increases (e.g,: Stein and Wysession, 2003; Lay and Wallace, 1995).

More in detail, the waves are characterized by a *wavelength*, defined as the maximum distance between two successive crests; an *amplitude*, meant as the maximum displacement of a particle from an equilibrium position when as the waves passed through; and a *period*, defined as the time that one wavelength takes to pass (Fig. 3.4).

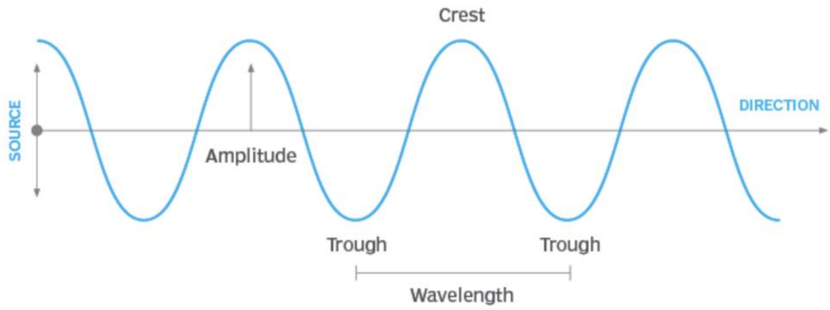

Fig. 3.4. Schematic description of a sound wave. https://www.techtarget.com/whatis/definition/sound-wave

The number of wavelength which passes a point per unit of time, by means the reciprocal of the period, defined the *frequency*. The wave, as mentioned above, travel through the Earth as an expanding sphere, that means that the amplitude is inversely proportional to the square of the radius of the sphere, and as a consequence, of distance from the source. In addition, for the Huygen's principles, every point on a wavefront is a source of new spherical waves (Fig. 3.5).

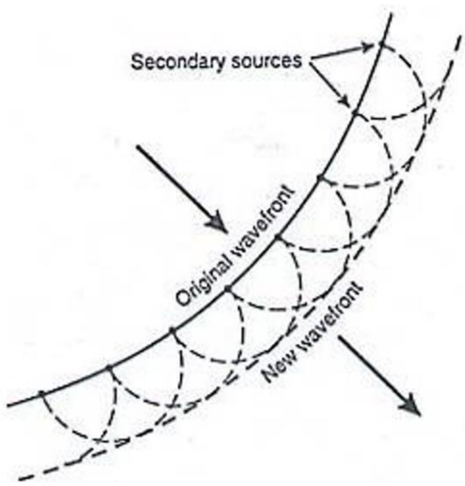

Fig. 3.5. Schematic representation of Huygen's principles (from Reynolds, 1997)

An amount of energy is lost when the seismic waves travels through the Earth layers, due to the energy dissipation derived from the non-perfectly elastic behavior of the rocks and to the refraction caused by irregularities (waves scattering) (e.g., Yeats et al., 2007). The reduction in amplitude of a seismic wave with the distance is called *attenuation*, and can be described by the equation:

$$P(R, f) = Z(R)exp\left(\frac{-\pi f R}{Q(f)V_{S,crust}}\right) \tag{3.1}$$

Where: $V_{S,crust}$ is the velocity of the shear wave propagating through the crust; f is the frequency of the shear wave; R is the path length of the shear wave from the source; $Q(f)$ is a crustal quality factor related to both material damping and wave scattering.

The body waves, which can travel through the inner part of the Earth, can be divided in P (primary o compressional) and S (secondary o shear) waves (Fig. 3.6). P-waves travel through solids and fluids, causing compression and successive dilation in the materials they pass, without significant permanent deformation. S-waves cause shear deformation in the materials through they travel, and for this reason cannot propagate through fluids. They can be divided into two type, depending on the path of the particles: SV, when the particles movement is in the vertical plane, and SH, when the particles move in the horizontal plane (e.g., Lay and Wallace, 1995; Kramer and Stewart, 2025).

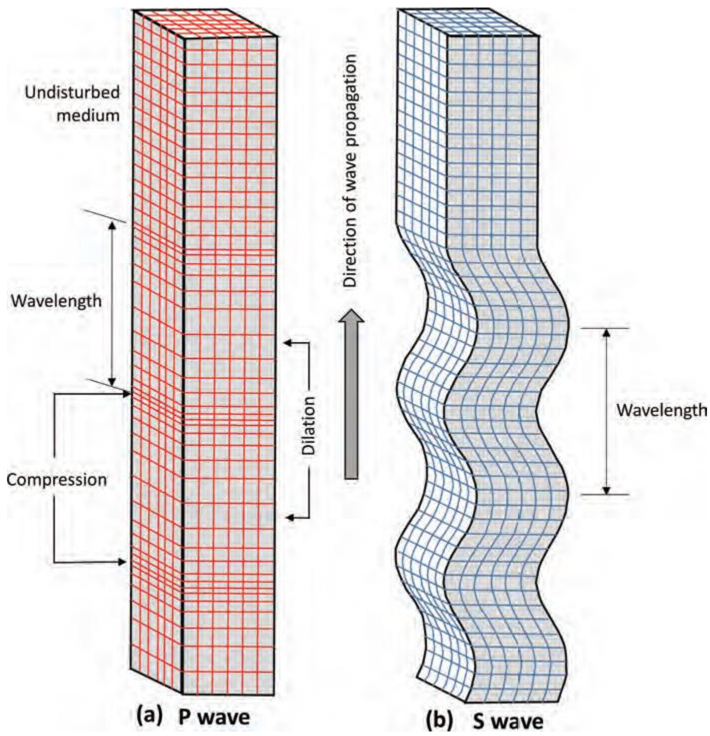

Fig. 3.6. Schematic description of the deformation produced by (a) P waves and (b) S waves (from Kramer and Stewart, 2025)

Surface waves are generated through the interaction between body waves and the Earth's surface, and they are named for their characteristic of abruptly diminishing amplitude with increasing depth. Due to the specific interactions needed for their formation, surface waves become more noticeable at greater distances from the earthquake's origin. When the distance exceeds approximately twice the Earth's crust thickness, surface waves typically dominate in producing the strongest ground motions, rather than body waves. The most relevant surface waves are Rayleigh waves, produced by the interaction between P- and SV-waves with the Earth surface, and the Love waves, generated by the interaction between SH-waves with a surficial layer of soft material overlying a stiffer deposit. The Rayleigh waves show both vertical and horizontal particles motion, while Love waves have not vertical component of the particles motion (Fig. 3.6).

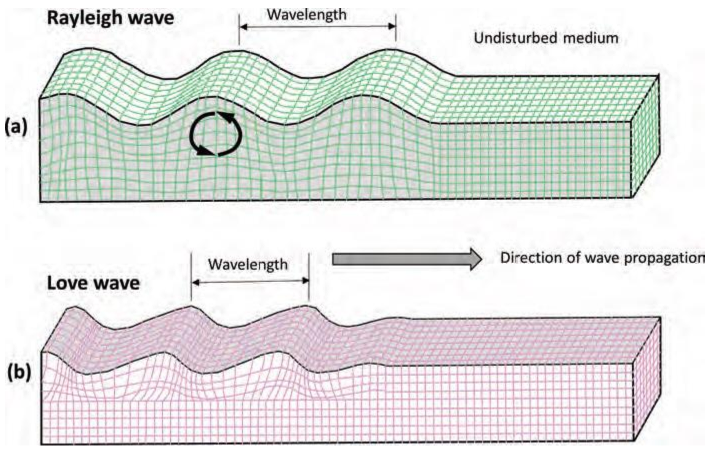

Fig. 3.7. Schematic description of the deformation produced by (a) Rayleigh waves and (b) love waves (from Kramer and Stewart, 2025)

Various magnitude scales are commonly used, each tailored to measure a specific type of seismic wave within a designated frequency range using a particular instrument. The scales predominantly employed in Western countries, listed in the order of their development, include the local magnitude (M_L), also called Richter magnitude, surface-wave magnitude (M_S), body-wave magnitude, divided in m_b for short period and m_B for long period, and moment magnitude (M_W or *M*). The moment magnitude scale, introduced by Kanamori in 1977 and further refined by Hanks and Kanamori in 1979, represents the most recent advancement and fundamentally differs from its predecessors. Unlike earlier scales that rely on the peaks recorded in seismograms, the M_W scale is based on the seismic moment (M_0) of an earthquake. The seismic moment is defined as:

$$M_0 = DA\mu \tag{3.2}$$

The average displacement across the entire fault surface is denoted by , while represents the fault surface area, and indicates the average shear rigidity of the rocks affected by the fault. The value of is derived from observed surface displacements or from displacements on the fault plane reconstructed through instrumental or geodetic modeling. The area is calculated by multiplying the length by the estimated depth of the ruptured fault plane, as indicated by surface rupture, aftershock patterns, or geodetic data. This approach assumes that the rupture area is rectangular. Consequently, the seismic moment more accurately reflects the energy released at the source, rather than relying on the effects of that energy on one or more seismographs located at a distance from the source. Moment magnitude is derived from the seismic moment using the Hanks and Kanamori (1979) relation for southern California.

$$M_W = \frac{2}{3}\log M_0 - 10.7 \tag{3.3}$$

The moment magnitude is represented by M_W, while the seismic moment is denoted by M_0. The seismic moment scale was created to address the issue of saturation found in other magnitude scales and is commonly employed to characterize major earthquakes (e.g., M_S > 8) (e.g., McCalpin et al., 2009).

Another fundamental seismic parameter is the Peak Ground Acceleration (PGA). The PGA for a given component of ground motion is simply the largest (absolute) value of acceleration. PGA and other Intensity Measures (IMs) for horizontal-component ground motions are often expressed in a manner that recognizes both horizontal directions of shaking (e.g., east-west and north-south). Horizontal accelerations have commonly been used to describe ground motions because of their natural relationship to the lateral inertial forces that tend to cause damage to structures; indeed the largest dynamic forces induced in certain types of structures (i.e., very stiff and elastic structures) are closely related to the horizontal PGA. Peak accelerations can also be related (e.g., Worden et al., 2012) to earthquake intensity, although such relationships are more efficiently defined in terms of peak velocity. Such correlations, while far from precise, can be useful for estimating PGA when only intensity information is available, as in the case of earthquakes that occurred before ground motion recording instruments were available (pre-instrumental earthquakes) (e.g., Kramer and Stewart, 2025).

In earthquake engineering, vertical accelerations have not been studied as extensively as horizontal ones. This is primarily because the safety margins against gravity-induced static vertical forces in structures generally provide adequate resistance to the dynamic forces generated by vertical accelerations during seismic events. The vertical-to-horizontal PGA ratio, or V/H ratio, is significantly affected by distance. It averages around one near the earthquake source but decreases to values between approximately 1/2 and 2/3 for fault distances exceeding about 50 km (Bozorgnia and Campbell, 2016).

Ground motions with high peak accelerations are often, though not always, more damaging than those with lower peak accelerations. However, extremely high peak accelerations occurring over a very brief duration often result in minimal damage. Several earthquakes have produced peak accelerations exceeding 0.5 g without causing significant harm because these accelerations occurred at very high frequencies compared to the fundamental frequencies of structures, and the shaking was short-lived. PGA is most effective for short, rigid structures or situations where the inertia of the ground itself is the main concern. For more flexible systems, PGA is generally not relied upon alone and is often supplemented with additional data to better assess the destructive potential of ground motions (i.e., while PGA can be predicted, it is neither efficient nor sufficient for forecasting the response of such systems) (e.g., Kramer and Stewart, 2025).

As previously noted, a fault's capacity to generate earthquakes depends on a compatible stress field aligning with the fault's kinematics. Consequently, not all existing faults are active. Moreover, an active fault may accommodate deformation through minimal and continuous movements, known as creep, which do not produce earthquakes. Therefore, the initial step in the analysis involves identifying active, seismogenic faults at both local and regional levels that could potentially impact specific infrastructure. By utilizing previously published studies and national catalogs, it is possible to determine if the area in question is prone to earthquakes and their potential magnitude, as well as the expected PGA value available in the literature, derived from deterministic or probabilistic methods (e.g., Seismic Hazard Maps with a fixed scenario, or fault-based Probabilistic Seismic Hazard Analysis – PSHA – studies).

In Deterministic Seismic Hazard Analysis (DSHA), seismic risks at a location are evaluated by considering the most severe possible scenario or *worst scenario*, without accounting for the likelihood of its occurrence over time, the duration of exposure, or the facility's design lifespan. This assessment involves using seismic source parameters, such as location and magnitude, in conjunction with the site's specific conditions, through algorithms that simulate physical processes. The resulting hazard estimates inherently include uncertainties due to the variability in the input parameters of the scenario, but not from an infinite array of scenarios. Essentially, DSHA assumes that a significant earthquake will occur close enough to impact the site and then focuses on determining the potential consequences of such an earthquake (e.g., Kramer and Stewart, 2025; McCalpin et al., 2009).

To evaluate ground shaking, the site's motion is determined by identifying the single source most likely to generate the strongest shaking in the area. Typically, this is the largest active fault closest to the location, known as the "controlling fault" for ground motions. However, in regions with few faults, the controlling source might be a random earthquake occurring very close to the site, not associated with any known fault. Since a DSHA is time-independent, the recurrence interval and slip rate of the controlling source are not considered; only its maximum (or characteristic) magnitude and proximity to the site are relevant for calculating ground shaking. The ground motion at the site is determined by inputting the maximum earthquake magnitude from the controlling source and the distance from the fault to the site into an attenuation equation (e.g., Kramer and Stewart, 2025; McCalpin et al., 2009).

Hazards from surface faulting and ground failure are managed through a deterministic approach. When faults are identified at a site, their risks are assessed based on their location and the maximum potential surface displacement they could cause in the future. Ground failure is evaluated by applying the maximum ground shaking at the site, along with its uncertainties, to equations that physically relate ground motion to liquefaction and landsliding (e.g., Kramer and Stewart, 2025; McCalpin et al., 2009).

PSHA provides a method for assessing seismic hazards by incorporating uncertainties related to earthquake size and location, recurrence rates, and the variability of ground motion characteristics across various magnitude and distance scenarios. Unlike DSHA, which estimates ground motions based on a specific earthquake scenario defined by a single magnitude-distance pair, PSHA considers contributions from all possible magnitude and distance combinations. It also encompasses the full range of ground motions that each combination can produce, with each possibility weighted by its likelihood of occurrence. As a result, PSHA eliminates the arbitrary decisions required in DSHA and offers a more comprehensive and objective depiction of seismic hazards (e.g., Kramer and Stewart, 2025; McCalpin et al., 2009).

In PSHA, the seismic risks at a specific location are defined as the most intense effects expected to occur, with a given probability of being surpassed, within a time period that matches the facility's design lifespan or a specified annual probability. These hazards are assessed by using seismic source parameters, such as location, magnitude, and frequency, along with the site's location and conditions, through a series of algorithms that connect the magnitude–frequency of all possible seismic sources to the distance from the site and the site's conditions. The calculated hazards include uncertainties from both the time-independent input parameters used in DSHA and the time-dependent characteristics of seismic sources, like recurrence interval and slip rate. Essentially, a PSHA estimates the likelihood of earthquakes occurring near the site and then evaluates the impacts of all these potential earthquakes (e.g., Kramer and Stewart, 2025; McCalpin et al, 2009).

Time-dependent models are utilized for all piecewise rectangular faults, even when the last rupture dates are unknown (Field, 2015). In contrast, large ruptures on faults are depicted using time-independent Poisson models, which are generally regarded as less precise. For off-fault areal sources, which are not associated with any specific known fault, location-specific Gutenberg-Richter a parameter values are derived from observed seismicity rates within areal source zones. Earthquake rates for all source types are evaluated to maintain regional moment balance, incorporating a range of geological, geodetic, and seismological data (e.g., Kramer and Stewart, 2025; McCalpin et al., 2009).

For the past two decades, the debate over the most effective method for forecasting future risks has persisted. DSHA is frequently regarded as a straightforward technique, and in many respects, it is. When applied to structures where failure could have catastrophic consequences, such as nuclear power plants and large dams, DSHA is often seen as providing a clear framework for evaluating "worst-case" ground motions for a specific scenario. However, the DSHA process involves several subjective decisions that can significantly affect the calculated IMs, leading to a "worst-case" condition that is poorly and often inconsistently defined (e.g., Kramer and Stewart, 2025; Mc Calpin et al., 2009). DSHA has been criticized for being overly conservative in design, as its "worst-case" hazards might have a very low likelihood of occurring. Engineers have pointed out that designing facilities with short design lifespans for such low-probability hazard scenarios can be extremely costly and may not be justified, especially if the facility's failure poses minimal risk to life or safety.

Similarly, the PSHA has encountered criticism for a variety of reasons. Some critiques argue that the algorithms used in PSHA do not accurately capture the physical processes that govern earthquake generation. Furthermore, it has been observed that significant historical earthquakes have produced ground motions exceeding those predicted by a PSHA at the same location (Kramer and Stewart, 2025; McCalpin et al, 2009).

3.1.2.2. Site effects and ground motion amplification

Once that it has been ascertained that the studied area is prone to the occurrence of an earthquake (the primary hazard), the subsequent step is to analyze the susceptibility to its secondary effects: ground motion amplification (site response), soil liquefaction, and landslide/rockfall occurrence. It appears to be clear that the likelihood of a given area to seismic hazard is mostly given by the surficial potential effects of an earthquake, which derive from the intensity and the frequency of the ground shaking. Thus, in this first screening phase of the index it must be also defined a threshold value of PGA, the exceedance of which can be considered as the potential of a given area to be prone to this hazard.

The effects of the occurrence of an earthquake on the ground are strictly correlated to the local soil conditions, as it is well documented literature (e.g., Crespellani and Facciorusso, 2010; Kramer and Stewart, 2025). This correlation was recognize since the past centuries, observing the distribution of damage after the occurrence of strong earthquakes, and was then scientifically approached and explained in the last decades (e.g., Pagliaroli , 2018).

One of the most representative example of the meaning of site effects is the M_W 8.0 (followed by a M_W 7.6 aftershock) Michoacan (Mexico) earthquake, which was one of the most deadliest earthquakes in the world history (https://earthquake.usgs.gov/learn/today/index.php?month=9&day=19&submit=View+Date). The earthquake derived from the subduction of the Cocos plate under the Caribbean plate, with an hypocenter located near the west coast of Mexico (Fig. 3.8).

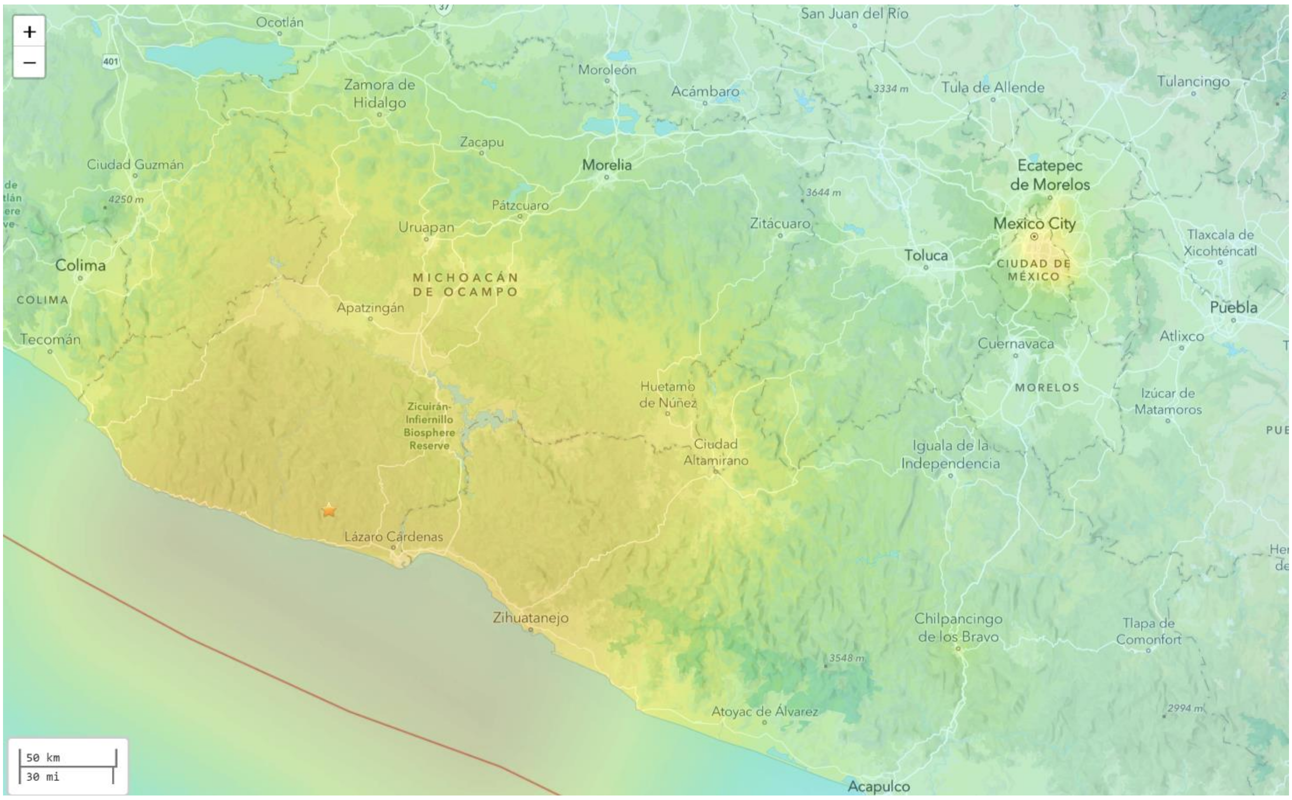

Fig. 3.8. Modified Mercalli Intensity (MMI) distribution map of the M_W 8.0 Michoacan earthquake (https://earthquake.usgs.gov/earthquakes/eventpage/usp0002jwe/map). The orange star represents the epicenter of the earthquake; the red line the trace of the boundary between the Cocos plate and the Caribbean plate; the shaded areas represents MMI values, ranging from about 7.5 (red) to 2.5 (blue). It is possible to notice that Mexico City, 370 km far from the epicenter, felt a MMI comparable with areas very close to the west coast.

During the earthquake, a 0.2 g PGA value was observed in the epicentral area and, unexpectedly, in the central part of Mexico City, 370 km far from the epicenter, despite of the attenuation laws and the evidences collected in the rest of the country, at the same distance. Over the years, numerous experimental and theoretical findings have conclusively shown that the primary cause of the 1985 disaster in Mexico City was significant local amplification, resulting from a very thin, extremely soft clay layer at the surface. Additionally, the basin's shape, which was once a lake, introduces two-dimensional effects due to the contrast between the rocks and the lacustrine sediments (e.g. Chávex-García and Bard, 1994; Mayoral et al., 2019).

Stratigraphic and topographic amplification, and basins effects (Fig. 3.9) are the objective of the site response analysis. Stratigraphic amplification occurs when the ground motion parameter (i.e., PGA) increases in value comparing the measure at the plain bedrock to the measure at the observed site. This effect can be determined by the contrast in V_S value between a seismic bedrock (rocks or deposits which present a $V_S \geq 800$ m/s) and soft deposits ($V_S < 800$ m/s), such as loose or poor densified sands, lacustrine silt and clays, and so on.

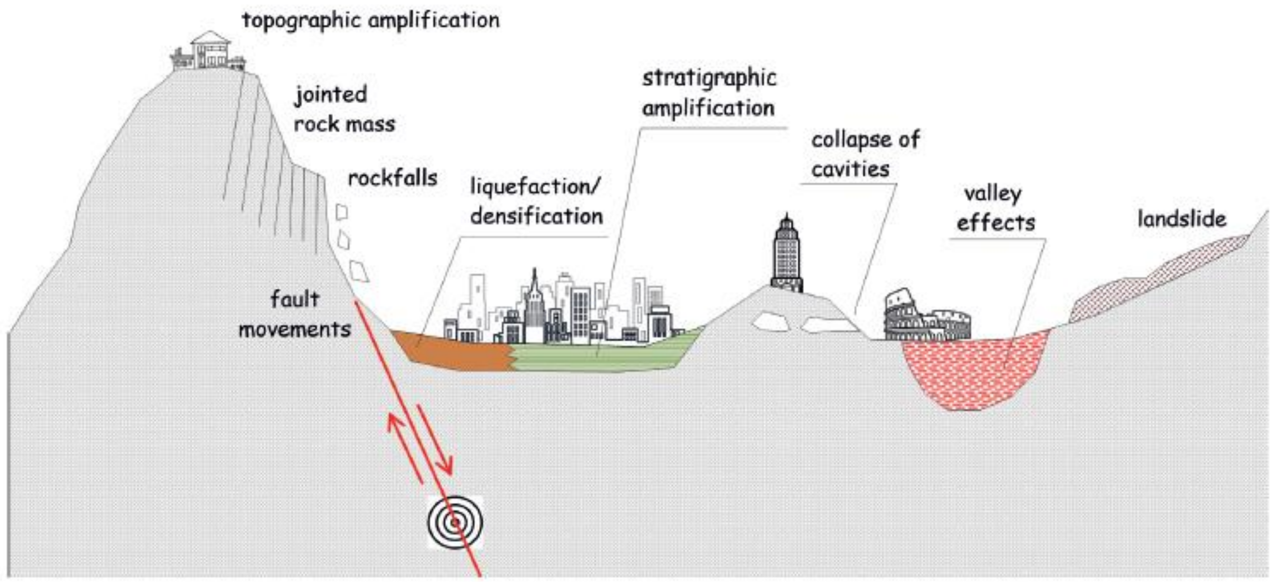

Fig. 3.9. Site effects during an earthquake. Black circles represent the hypocenter; Red arrows represent the relative motion of the faulted blocks (Pagliaroli, 2018).

Ground motion amplification can occurred even at bedrock, due to the shape of the site, as illustrated in Fig. 3.11. For instance, ridges and slopes can focus seismic energy at resonant frequencies, leading to localized amplification of ground motion. These phenomena typically occur at high frequencies where a portion of the wavelength (about 1/4–1/6) aligns approximately with the size of the morphological feature, such as the horizontal width of a slope or half the width of a ridge (Kramer and Stewart, 2025).

Basins effects consist in the amplification of the seismic signal caused by the contrast between the “walls” of the basin with the infill sediments. It happens when the alluvial deposits composing the basin have a slower V_S than surrounding basement rocks, that can lead to a reflection/refraction phenomena of the seismic waves, which generate surface waves that travel along the basin, with an increase of the ground motion parameters.

3.1.2.3. Soil Liquefaction

As a primary screening method, utilizing available maps and catalogues is advantageous for identifying ground motion amplification effects and employing geological-geotechnical criteria to assess liquefaction susceptibility. Soil liquefaction during an earthquake refers to the loss of strength and stiffness, leading to deformations in soil deposits. This phenomenon can be explained by the tendency of loose sands, gravels with more than 30% sand content, and non-cohesive silts to contract under the cyclic load imposed by earthquake shaking. If the soil is saturated and unable to drain, the normal stress transfers from the solid matrix to the pore water, causing a buoyancy effect on the grains. The surface effects of liquefaction at depths of no more than 20 meters can cause damage due to vertical and horizontal ground settlements, more so than the manifestations themselves, such as sand boils (Idriss and Boulanger, 2008; Roy and Rollins, 2022). According to national building design codes (e.g., NTC, 2018), it is important to clarify that an area is considered susceptible to soil liquefaction if the groundwater table is within the first 15 meters from the surface; if the subsoil within the first 20 meters is composed of non-cohesive, granular loose deposits; and if the expected PGA value exceeds 0.1 g in free field conditions.

The behavior of liquefaction can be evaluated on a regional scale by considering historical, geological, and compositional factors. For example, if an area has previously experienced soil liquefaction due to earthquakes, it can be considered susceptible to such events. In this regard, examining past paleoliquefaction studies can help identify evidence of historical liquefaction. Additionally, deposits prone to liquefaction are found within a limited range of geological settings and ages. Saturated fluvial, colluvial, and aeolian deposits, along with alluvial fans and plains, are vulnerable to liquefaction. Holocene deposits are more likely to undergo liquefaction compared to Pleistocene soils, while liquefaction in deposits older than the Pleistocene is extremely rare. This can be attributed to compositional factors: only coarse-grained, non-plastic saturated soils can generate sufficient pore pressure under cyclic loading to liquefy (e.g., Kramer and Stewart, 2025).

In the initial stage of GETI, the susceptibility of a given area to liquefaction can also be assessed using seismic microzonation study maps. These maps indicate, particularly for structures within a municipality's boundaries, areas likely to experience liquefaction during a specified seismic event. These insights are drawn from literature reviews in level 1 seismic microzonation studies and from in situ and geophysical tests in level 2, which offer the most accurate understanding of subsoil behavior. The literature presents various methods for estimating liquefaction probability, both from a point-based perspective (e.g., Idriss and Boulanger, 2008) and an area-based perspective, such as the *Global model for liquefaction potential* proposed by Zhu et al. (2017), which utilizes spatial data to assess an area's susceptibility to liquefaction. In this approach, the effects of earthquake loading are approximated using the PGA_M, derived from the PGA value from ShakeMaps or ground motion prediction equations, normalized to a M_W 7.5 with the equation proposed by Youd et al. (2001) for the Magnitude Scaling Factor (MSF).

The probability of liquefaction manifestation is then computed as:

$$P(X) = (1 + e^{-X})^{-1} \tag{3.4}$$

Where X is a set of geospatial variables, defined by the equation 3.2:

$$X = 24.10 + 2.067 \ln(PGA_M) + 0.355CTI - 0.4784 \ln(V_{S30}) \tag{3.5}$$

Where CTI is the compound topographic index proposed by Moore et al., 1991, and can be considered as a metric of potential ground wetness (steady-state, or based on variables that remain relatively constant over time); CTI models water flow accumulation as a function of upstream contributing area and slope (calculated by percent rise). V_{S30} is the average shear-wave velocity for the upper 30-m depth and is estimated from topographic slope. Both can be derived from thematic maps available in literature in the most part of the world. If this too simplified model seams to work with an acceptable approximation in coastal areas (e.g., Zhu et al., 2015, 2017; Maurer 2017), it appears that it is not the same in the internal areas (Zhu et al., 2017), such as intramountain basins. Further studies are required to better understand the applicability of the method, but it may be a good compromise for a first screening in soil liquefaction assessment in coastal areas.

If geotechnical information on the characteristics of the subsoil (e.g., Atterberg limits) are available, it is possible to assess the susceptibility to liquefaction in a given area using the abaci inspired by the Chinese criteria proposed by Wang et al. (1979), which considered as prone to liquefaction soil characterized by: a clay content (particles smaller than #200 sieve) <15% by weight; a liquid limit of 35%; a natural moisture content > 0.9 times the liquid limit. These methods are a reasonable first screening in liquefaction assessment. As an example, in Figure 3.10 abaci by a) Andrews and Martin (2000), b) Bray and Sancio (2006), and c) Idriss and Boulanger (2008) are reported. It is important to highlight that those methods require detailed sampling of the first 20 m of the subsoil and geotechnical laboratory tests to be effective in assessing the susceptibility to soil liquefaction of a given area, and that they cannot substitute the evaluation through in-situ tests-based simplified methods (e.g., Idriss and Boulanger, 2008).

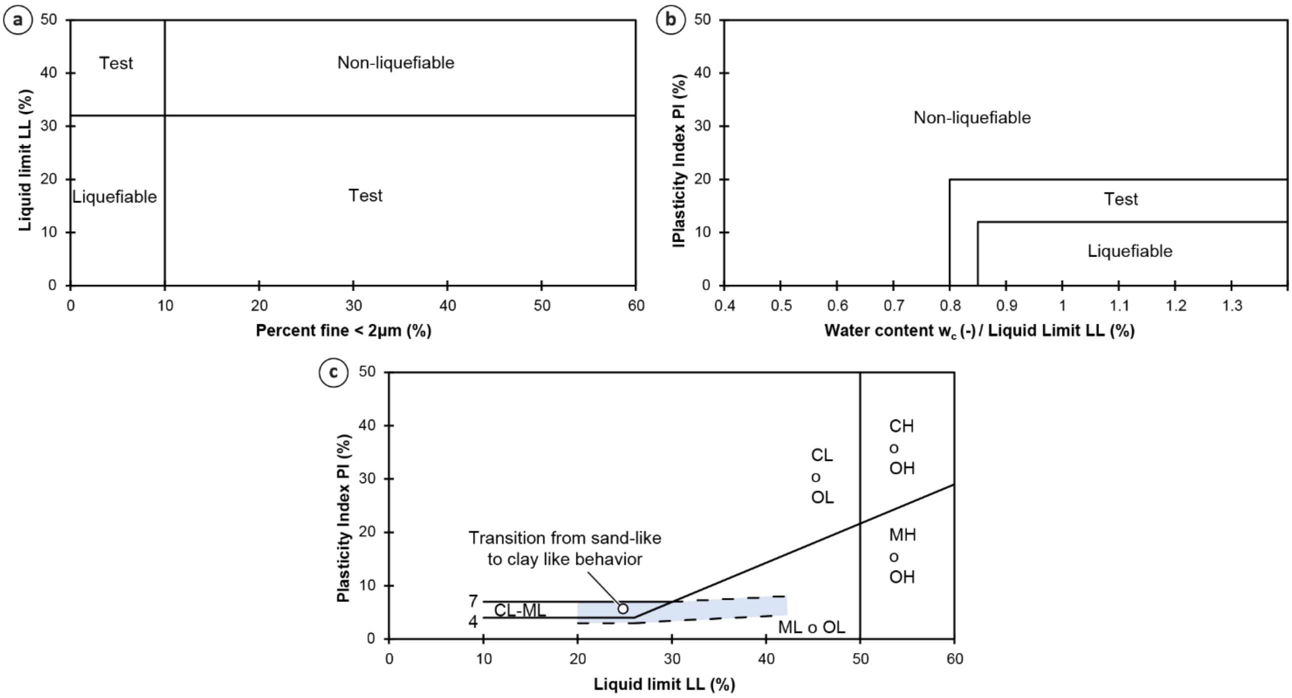

Fig. 3.10. Preliminary screening abaci for liquefaction assessment using Atterberg limits. Modified from: a) Andrews and Martin (2000); b) Bray and Sancio (2006); c) Idriss and Boulanger (2008).

In addition, several authors developed relationships to predict the maximum epicentral distance at which liquefaction features might be observed as a function of earthquake magnitude. Ambraseys (1988) plotted the epicentral distance of liquefied sites (R_e) in kilometers versus the moment magnitude (M_w), considering a worldwide dataset and developed the relationship:

$$M_w = -0.31 + 2.65 \times 10^{-8} \times (R_e * 10^5) + 0.99 \times \log(R_e * 10^5) \quad (3.6)$$

Later Galli (2000) proposed a bounding equation based on an Italian catalogue of historical earthquakes (CPTI 1999, period 1900-1990), using the surface-wave magnitude M_s:

$$M_s = 1.5 + 3.1 \log(R_e) \quad (3.7)$$

Furthermore, Castilla & Audemard (2007) proposed a boundary curve derived from a worldwide database of sand-blows as a function of the moment magnitude for the earthquakes:

$$M_w = 2.44 \log(R_e) + 1.95 \quad (3.8)$$

More recently, Maurer et al. (2015) proposed a new regression curve based on the New Zealand historical earthquakes and related paleoliquefaction, incorporating the information available from Ambraseys (1988) given by:

$$M_w = -0.26 + 2.4 \times 10^{-7.58} \times (R_e \times 10^{4.98}) + 0.96 \times \log(R_e \times 10^{5.02}) \quad (3.9)$$

All these boundary curves are plotted in Figure 3.11, together with the worldwide gravel liquefaction data points (Salvatore et al., 2022) that approximately follow the regression curve proposed by Maurer et al. (2015).

Although current national and international regulations (e.g., NTC18, 2018) consider only soils with grain sizes ranging from fine to coarse sands to be susceptible to liquefaction (Fig. 3.11), the historical presence of liquefaction phenomena in gravelly (Rollins et al., 2021; Salvatore et al., 2022) and non-plastic silty (Boncio et al., 2018; Boncio et al., 2020) deposits has been well documented in the literature.

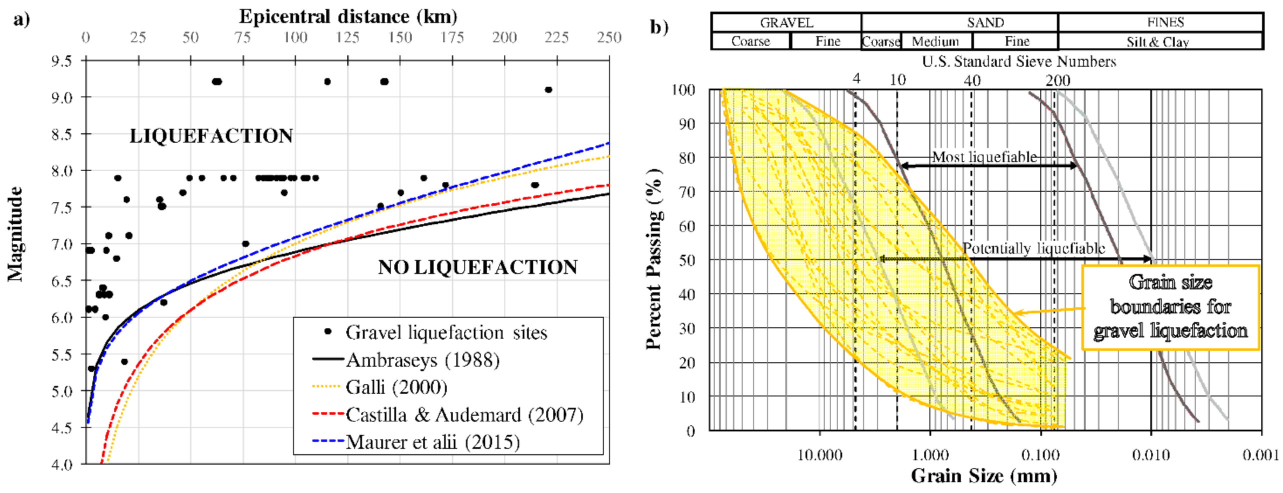

Fig. 3.11. – (a) Chart of magnitude vs. epicentral distance to gravel liquefaction sites and available reference correlations (Ambraseys, 1988; Galli, 2000, Castilla & Audermard, 2007, Maurer et alii, 2015); and (b) Gradation curves of liquefied gravelly soils (dashed yellow lines, modified after Rollins et alii, 2021). The chart proposes grain size boundaries for gravel liquefaction in comparison with the grain size ranges proposed by Tsuchida & Hayashi (1971) for the most susceptible soils to liquefaction and potentially susceptible soils to liquefaction using a coefficient of uniformity $C_U > 3.5$. From Salvatore et al. (2022)

It is crucial to recognize that conducting geotechnical laboratory assessments of gravelly and sandy soils has consistently posed challenges due to the difficulty in obtaining undisturbed or partially disturbed samples with a sufficiently large diameter to be representative. Since 1968, Blevins et al. introduced a method involving the use of liquid nitrogen to freeze soil that is too loose or coarse, a technique that has been refined by various researchers and remains in use alongside the reconstitution of gravelly or sandy soil samples (e.g., Lo Presti et al., 2006) for laboratory testing. Unfortunately, these methods are costly, and the transition in stress conditions from the field to the lab often impacts the results (Cao et al., 2013). In this context, for liquefaction analyses of coarse-grained soils, simplified approaches have been devised that link soil penetration resistance with liquefaction susceptibility (e.g., Idriss and Boulanger, 2008; Rollins et al., 2021). Additionally, methods based on soil behavior during shear wave passage are also employed. (e.g., Andrus and Stokoe, 2000; Rollins et al., 2022).

3.1.2.4. Landslides

Landslides, also known as mass movements or mass wasting, are phenomena of ground instability that occur when volumes of soil, rock, or debris move down a slope under the force of gravity, generally as a result of a combination of factors including geological and geomorphological conditions, weather conditions, seismic activity, volcanic eruptions, coastal or river erosion, and human activities (e.g., . Kefeer, 2002). Moving to landslides assessment, the susceptibility of an area to landslides due to the earthquake shaking obviously first relates to its morphological framework: e.g., if the infrastructure is located on a wild plain, the area can be considered not prone to this kind of phenomena. Slopes become unstable when the shear stresses required to maintain equilibrium reach or exceed the available shearing resistance on some potential failure surface. When an earthquake occurs, even moderately stable slope can fail due to the effect of the ground shaking (e.g. Kefeer, 2002; Kramer and Stewart, 2025).

There are many types of landslides that can be activated by an earthquake (Fig. 3.12): disrupted soil slides are the most common; soil slumps, soil block slides, and soil avalanches are abundant in historical record; soil falls and rapid soil flows are moderately common; subaqueous landslides and slow earth flows are uncommon (Kefeer, 2002).

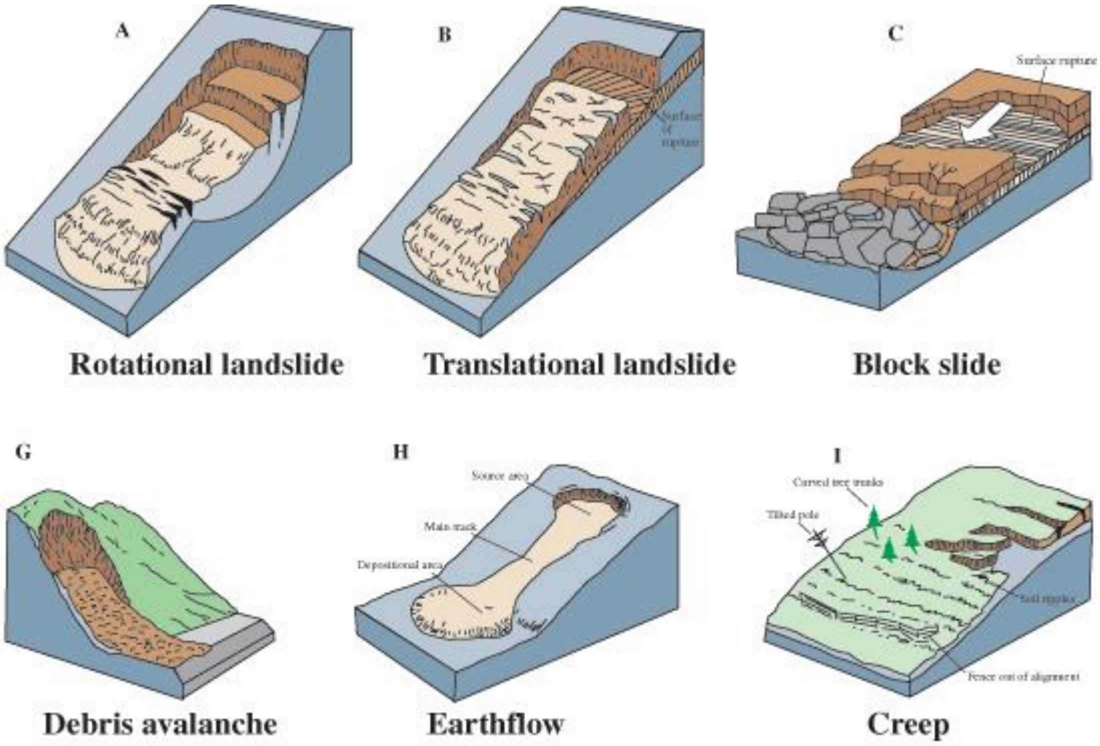

Fig. 3.12. Schematic illustration of the major types of landslide movement. From https://pubs.usgs.gov/fs/2004/3072/fs-2004-3072.html

The stability of a slope is influenced by many causes, such as geological and hydrological conditions, or topography. In the first level of analysis, it is possible to derive the susceptibility of an area to landslide from literature and catalogues, considering the presence of a slope, its distance from the infrastructure, the slope angle, the stratigraphy, as well as previous landslides/rockfall affecting the same slope. It is also useful to use magnitude-distance relation to better constrain the influence of the ground shaking on slope stability.

3.1.2.5. Rockfall

Among the landslide types described in the classification by Varnes (1978) and subsequent authors, rockfalls constitute a potentially very dangerous form of slope failure. However, the level of associated risk can vary significantly depending on the context in which the landslide occurs and the specific characteristics of the event. By definition, a rockfall occurs when a mass of variable size detaches from a slope, generally one that is steep to sub-vertical, along a surface where only minimal shear deformation takes place, and descends downward through free fall, bouncing, or rolling, depending on the geometry of the slope. Such movements can range from rapid to extremely rapid and may or may not be preceded by smaller displacements that lead to the progressive detachment of the mass from its source on the affected slope (Piattelli, 2024).

There are many types of rockfall that can be activated by an earthquake (Fig.3.13): rockfalls and rock slides are the most common; rock slumps are moderately common; rock block slides, and rock avalanches are uncommon (Kefeer, 2002).

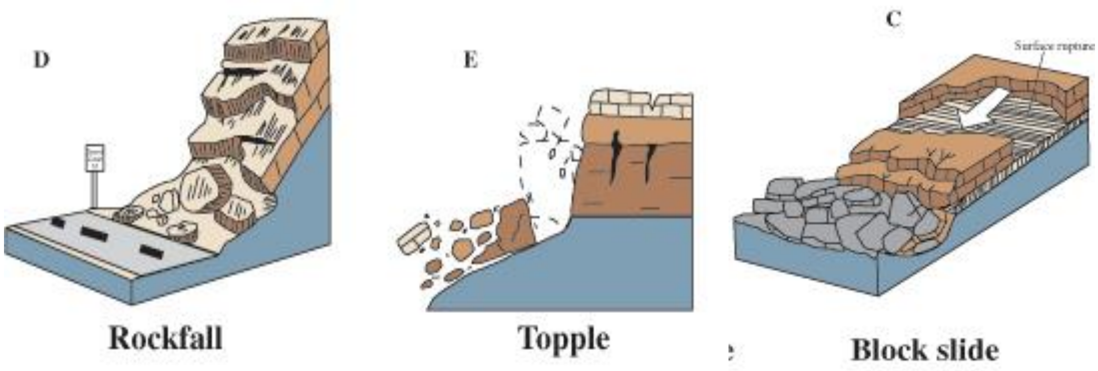

Fig. 3.13. Schematic illustration of the major types of rockfall movement. From https://pubs.usgs.gov/fs/2004/3072/fs-2004-3072.html

Regarding the initiation of this type of landslide, the lack of static constraints is essential for a slope to undergo instability. The failure kinematics can vary based on the characteristics of the discontinuity systems within the rock mass. Movements typically manifest as planar or wedge failures, where sliding occurs along a discontinuity that dips in the same direction as the slope or along two intersecting discontinuities that dip in the same direction as the slope, respectively. In contrast, for overhanging blocks, failure kinematics might involve shear failure with a sub-vertical detachment or flexural failure, the latter happening when the overhanging block is mainly horizontally oriented. The rock masses involved in landslide movements can display a wide range of volumes and geometric characteristics, depending on the failure kinematics and the geometric features of the existing discontinuities (Piattelli, 2024).

At Level 1, geotechnical tests and laboratory analyses are not required. However, it is essential to conduct surveys to compare the data from the literature with the actual conditions of the area. The output data should evaluate potential susceptibility to the considered hazards without estimating the probability of their occurrence. If the area is susceptible to one or more hazards, it is necessary to proceed to Level 2 analyses.

3.2. Methods in Analysis: Level 2

3.2.1. Site Response Analysis

Site response analysis can be conducted through one-dimensional (1D) or two-dimensional (2D) numerical modeling (contingent on the surficial and buried morphological characteristics of the area driving the potential bi-dimensional effects on ground motion amplification) utilizing available computational codes, as reported by Pagliaroli (2018). The input parameters for site response analyses (subsoil model including stratigraphy and geotechnical properties of the soil, such as V_S, nonlinear stiffness (G/G_0), and damping curves) can be derived from previous studies identified in Level 1 and new tests conducted in Level 2.

Today, there are numerous computer programs available for conducting numerical ground response analyses. Table 3.1 highlights some of the most commonly used ones in Italy and globally, detailing their key features such as geometry, analysis method and domain, and constitutive models. For more advanced site response codes and comprehensive information, Regnier et al. (2016) offers insights from a recent international benchmark on numerical simulations. The choice of modeling geometry (1D or 2D/3D) should be based on the complexity of the bedrock's shape, soil stratification, and topography. Another consideration is selecting the analysis method and the corresponding constitutive relationships for soil behavior. Essentially, two analysis methods can be employed to address soil nonlinearity (Table 3.1): the equivalent linear method, which involves iterative analyses assuming visco-elastic soil behavior, or a true nonlinear approach. The latter requires addressing additional factors such as the model for the skeleton curve, criteria for loading-unloading-reloading behavior, total stress or effective stress analysis approach, and models for pore water pressure generation and dissipation.

Table 3.1. Main computer codes for site response analysis

Geom	Code	Analysis domain (numer. scheme)	Analysis method	Constitutive model	TSA/ESA	Reference
1D	SHAKE	FD (CRM)	EL	Visco-elastic	TSA	Schnabel et al. (1972)
	SHAKE91					Idriss and Sun (1991)
	ProSHAKE					EduPro Civil System (1998)
	EERA					Bardet et al. (2000)
	STRATA	FD (RVT-CRM) *				Kottke and Rathje (2008)

	DEEPSOIL	FD (CRM)				DeepSoil V7.1 (2024)
		TD (FDM)	NL	Hyperbolic EMKZ + MR/NMR	TSA-ESA	
	DMOD2000	TD (FEM)		MKZ + MR		Matasovic and Ordonez (2010)
2D	QUAD4	TD (FEM)	EL	Visco-elastic	TSA	Idriss et al., (1973)
	QUAD4M					Hudson et al. (1994)
	LSR2D					https://www.stacec.com
	QUAKE/W				TSA-ESA	www.geo-slope.com
	BESOIL	FD (BEM	L		TSA	Sanò (1996)
2D/3D	FLAC	TD (FDM)	NL	Hysteretic +MR/ Elastoplastic	TSA-ESA	www.itascacg.com
	PLAXIS	TD (FEM)		Elastoplastic		www.benteley.com
	ABAQUS					www.3ds.com
	GEFDyn					Aubry and Modaressi (1996)
	OpeenSees			Hyperbolic/ Elastoplastic		http://opensees.berkeley.edu/

Legend:
BEM=Boundary Element Method
CRM=Complex Response Method (transfer functions)
EL=Equivalent Linear
EMKZ= Extended Modified Konder-Zelasko Model
ESA=Effective Stress Analysis
FD=Frequency Domain
FDM=Finite Difference Method
FEM= Finite Element Method
L=Linear
MR=Masing Rules
NL=Nonlinear
NMR=Non Masing Rules
RVT=Random Vibration Theory method
TD=Time Domain
TSA=Total Stress Analysis

* allowing randomization of site properties (Monte Carlo method)

The equivalent linear approach can lead to significant errors in the numerical evaluation of site response when dealing with high levels of soil nonlinearity, such as soft layers or high-intensity input motions. According to the literature, a maximum threshold of 0.1% in terms of maximum shear strain is recommended for the applicability of this method (Kaklamanos et al., 2013). Beyond this threshold, true nonlinear analyses become necessary..

Advanced elasto-plastic nonlinear models are capable of accurately representing behavior at significant strain levels, including the formation of plastic deformations, soil shear strength, and the accumulation of pore pressure (e.g., Pisanò and Jeremic 2014). These models are characterized by essential components such as yield surfaces, flow rules, and hardening/softening laws, with phase interactions being modeled using a generalized consolidation theory applicable to dynamic conditions (e.g., Sica, 2001). Despite their comprehensiveness, the practical application of these models is often hindered by the numerous constitutive parameters and the intricate calibration processes, which sometimes require unconventional laboratory equipment. Consequently, more simplified nonlinear models, like those in the hyperbolic soil model family, are frequently employed for nonlinear simulations (e.g., DEEPSOIL V7.1, 2024). Hyperbolic models necessitate defining the skeleton curve and establishing criteria for loading-unloading-reloading behavior. For changes in pore water pressure during seismic events, semi-empirical models (i.e., power water pressure generation relationships) can be used alongside hyperbolic models working in total stress.

In this study, nonlinear analyses were executed using hyperbolic models incorporated into the Deepsoil software. These analyses were carried out under total stress conditions, which means the effects of pore water pressure generation and dissipation on seismic response were not taken into account. Deepsoil (DEEPSOIL V7.1, 2024) is a tool for one-dimensional site-response analysis, mainly used for nonlinear (NL) time-domain analysis, with or without pore pressure generation. For nonlinear analysis, a multi-degree-of-freedom lumped model is used, where each layer is represented by a mass, a nonlinear spring, and a dashpot for viscous damping. The soil response is derived from a constitutive model that describes cyclic behavior. To represent the initial stress-strain backbone curve, Deepsoil employs an updated version of the Modified Kondner Zelasko (MKZ) model proposed by Matasovic (1993); additionally, a general quadratic/hyperbolic (GQ/H) model (Groholski et al., 2016), which explicitly considers soil strength, is available for the backbone curve. Deepsoil applies both the standard and a modified version of the extended Masing rules (Masing, 1926) to simulate the unloading-reloading branches. To simulate soil damping at low strain levels where hyperbolic models predict near-zero damping, Deepsoil offers several options. Besides the two-control frequencies full Rayleigh formulation (Verrucci et al., 2022), it includes an extended Rayleigh formulation (Park and Hashash, 2004), which requires the user to define four control frequencies, thereby broadening the frequency range with minimal damping variation. Additionally, a frequency-independent damping formulation is available (DEEPSOIL V7.1, 2024).

In this study the extended MKZ model with Non-Masing rules and frequency independent damping was employed. The Modified Kondner Zelasko model, known as MKZ, is a constitutive model based on a modification of the hyperbolic model first suggested by Kondner (1963) that uses a hyperbolic shear stress-strain relationship according to the following equation:

$$\tau = \frac{G_0\gamma}{1+\beta\left(\frac{\gamma}{\gamma_r}\right)^s} \tag{3.10}$$

where G_0 is the initial shear modulus, τ is the shear stress, γ is the shear strain. while β, s, and γ_r are the model parameters to be determined by fitting the normalized shear modulus and damping curves. Moreover, Deepsoil extends the MKZ through the "pressure-dependent hyperbolic model" proposed by Hashash and Park (2001) allowing the reference strain confining to be pressure-dependent (i.e. depending on the effective vertical stress). The non Masing rules are based on the application of the Modulus Reduction and Damping Curve Fitting developed by University of Illinois (MRDF-UIUC) reduction factor $F(\gamma_m)$.

The input motion is applied as acceleration time histories at the outcropping bedrock. We utilized natural accelerograms, chosen by comparing the tectonic regime with that of the studied area. Additional seismological parameters, such as source-to-site distance, are generally necessary for selecting input accelerograms applied at the seismic bedrock. The data output provides a PGA profile with depth and other relevant ground motion parameters, such as accelerograms or acceleration response spectra at the ground surface or foundation depth, quantifying the seismic action on the structure while considering ground motion amplification phenomena (Fig. 3.15).

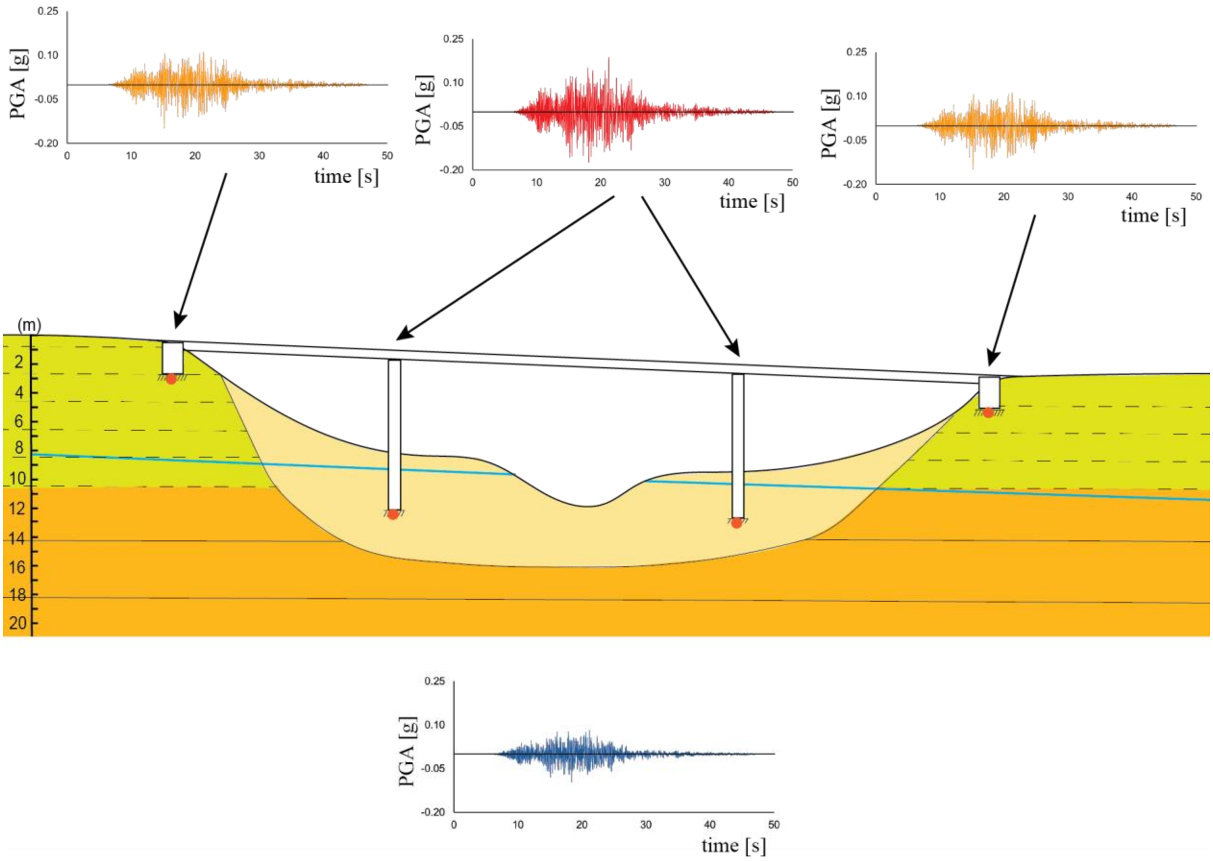

Fig. 3.15. Sketch of a 2D site response analysis of a bridge crossing a valley filled by alluvial soils showing typical results of ground motion at the foundations level. The blue accelerogram represents the seismic input

at bedrock for an assigned seismic scenario (defined by a certain probability of occurrence/return period), red and orange accelerograms the ground motion at the foundations level. Yellow and orange polygons represent stratified consolidated deposits, while light-yellow depicts loose deposits.

3.2.2. Soil Liquefaction Assessment

It is well established that traditional sampling methods fall short in generating a sufficient number of high-quality samples to ensure the reliability of cyclic strength measurements. Consequently, the likelihood of soil liquefaction due to seismic events can be assessed using simplified approaches that rely on in-situ testing. These tests may involve directly measuring the soil's resistance to penetration, such as through the Standard Penetration Test (SPT), Cone Penetration Test (CPT), or Dynamic Penetration Test (DPT). Alternatively, they can measure the Shear Waves Velocity (V_S) within the top 20 meters below the surface, as outlined by Idriss and Boulanger (2008).

While the existing national building design codes, such as NTC18 (2018), delineate the limits of soil susceptibility to liquefaction by focusing solely on the particle size range of sands (Fig. 3.16), it is widely recognized in the literature that gravelly and silty soils can also undergo liquefaction under specific conditions (Rollins et al., 2021; Salvatore et al., 2022; Boncio et al., 2018, 2020). Consequently, grain size alone is not a reliable parameter for evaluating soil liquefaction susceptibility.

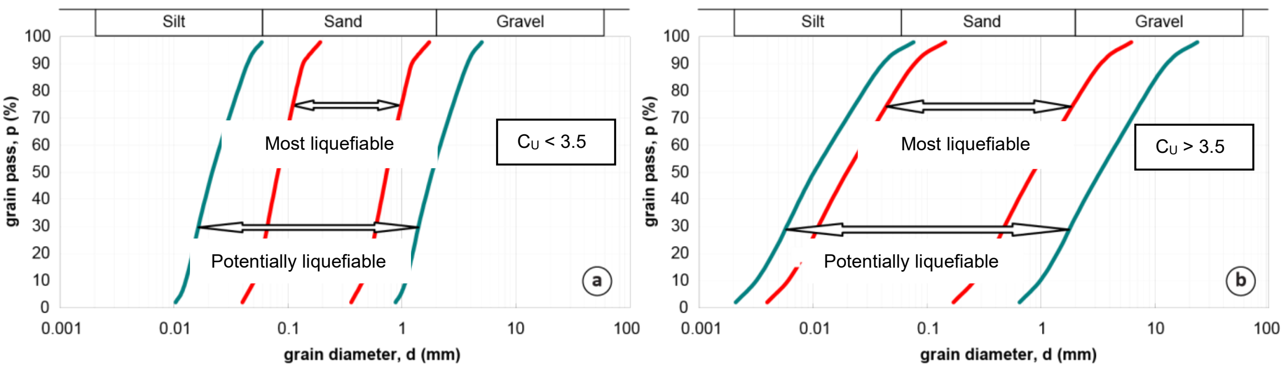

Fig. 3.16. Grain size boundaries charts for soil liquefaction, considering a) a coefficient of uniformity < 3.5 and b) > 3.5. Modify from Tsuchida and Hayashi (1981).

Apart from these considerations, the first step is to identify the predominant grain size between non cohesive silt, sand and gravel, to better focus the analysis using methods developed for sandy (e.g., Idriss and Boulanger, 2008; Andrus and Stokoe, 2000), silty (e.g., Andrews and Martin, 2000; Idriss and Boulanger, 2008), and gravelly (e.g., Rollins et al., 2021; Rollins et al., 2022) soils. As input data, this approach requires the expected M_W value, PGA value at the surface (including ground motion amplification), depth of the Groundwater Table (GWT), stratigraphy, geotechnical properties of the soil. Depending on the simplified method selected for the analysis, the mechanical parameters necessary for the analysis are V_S, standard penetration test blow count (N_{spt}), dynamic penetration test blow count (N_{DPT}), or soil resistance measured by cone penetration test (q_c) values derived from in situ tests.

In simplified methods, the cyclic resistance ratio (CRR), representing the soil's ability to withstand liquefaction. According to the "simplified procedure" by Seed and Idriss (1971), the cyclic stress ratio (CSR), indicating the seismic demand on a soil layer, is calculated based on the ratio of total (σ_v) to effective (σ_v') vertical stresses, multiplied by the PGA and the shear stress reduction coefficient (r_d) proposed by Liao and Whitman (1986), which describing the ratio of cyclic stresses for a flexible soil column to the cyclic stresses for a rigid soil column (Eq. 3.11).

$$\mathrm{CSR} = 0.65 \cdot (\sigma_{v0}/\sigma_{v0}') \cdot PGA \cdot r_d \tag{3.10}$$

Youd and Idriss (2001) introduced the MSF to adjust the CSR to a standard magnitude of 7.5 ($\mathrm{CSR}_{7.5}$), serving as a "proxy" for the effects of duration on liquefaction triggering. To address high effective overburden stress, they incorporated the overburden correction factor (K_σ), which depends on the effective vertical stress (σ_v') and relative density (D_r), to further modify the cyclic stress ratio to $\mathrm{CSR}_{7.5,1\,atm}$ (Eq. 3.11).

$$\mathrm{CSR}_{7.5} = CSR/(MSF \cdot K_\sigma) \tag{3.11}$$

This led to the definition of the liquefaction threshold value, known as the safety factor against liquefaction (FS), as the ratio of CRR to $\mathrm{CSR}_{7.5,1\,atm}$ (Eq. 3.12).

$$\mathrm{FS} = CRR/CSR_{7.5,1\,atm} \tag{3.12}$$

The SPT or CPT-based method is often effective in accurately assessing the liquefaction potential of sandy soils and loose gravel with low penetration resistance, after applying a correction factor (e.g., Kokusho & Yoshida, 1997). However, when penetration resistance is higher, the results may be less reliable. In such cases, it can be challenging to determine whether the increased blow count is due to larger particles or a denser material (Cubrinovsky et al., 2018; Rollins et al., 2021). This issue can be addressed by employing geophysical measurements using shear wave velocity (V_S), as proposed by Andrus & Stokoe (2000) and Rollins et al. (2022). Nonetheless, research indicates that the V_S thresholds for triggering liquefaction might be greater for gravels compared to sands (e.g., Rollins et al., 2022), and that V_S measurements pertain to small strains, whereas liquefaction occurs at medium to high strains, which are better defined by penetration tests (e.g., Mayne et al., 2009). Although the parameter is directly linked to the small strain shear modulus and thus measures stiffness at small strains, it remains valuable as an indicator of liquefaction resistance because, like penetration resistance, it is similarly affected by void ratio, confining stress, stress history, and geological age (Youd and Idriss, 2001).

Youd and Idriss (2001) introduced a method for evaluating liquefaction in sandy soils by normalizing the SPT blow count (N_{SPT}) or CPT resistance measured q_c to an overburden pressure of 100 kPa

(~1 atm) and adjusting for hammer energy, borehole diameter, rod length, and sampler type. The normalized parameter, $(\mathrm{N}_1)_{60}$ or q_{c1N}, which is the adjusted SPT blow count or CPT resistance measured, is further modified for fines content to derive the equivalent clean sand blow count, $(\mathrm{N}_1)_{60cs}$ or $(\mathrm{q}_{c1N})_{cs}$, which is then used in analyses. Later, Idriss & Boulanger (2008) revised the liquefaction assessment method from Youd & Idriss (2001), suggesting a value of r_d that varies with magnitude and an overburden correction factor, K_σ, related to (σ_v') and $(\mathrm{N}_1)_{60}$, along with an updated relation for $(\mathrm{N}_1)_{60CS}$, expanding the SPT case histories database. More recently, Boulanger & Idriss (2014) redefined the MSF equation to also consider soil properties.

Chinese engineers have developed the dynamic cone penetration test (DPT), which involves the continuous driving of a 74 mm cone by a 120 kg hammer dropped from a height of one meter, utilizing either a drilling rig or a simple SPT tripod system (Chinese Design Code, 2001). This design facilitates global applicability. In 2008, researchers from the Institute of Engineering Mechanics (IEM) employed the DPT to assess penetration resistance at gravel liquefaction sites following the MW 7.9 Wenchuan earthquake. They devised a probabilistic DPT-based method to evaluate gravel liquefaction, drawing on data from 19 sites with observed gravel liquefaction and 28 sites without visible signs of liquefaction (Cao et al., 2013). Similar to the SPT, the DPT requires hammer calibration to determine the Energy Transfer Ratio (ETR), which is the ratio of energy transferred from the hammer to the rods. This calibration is crucial for adjusting the raw DPT blow counts, recorded every 10 cm of penetration, to account for hammers with varying efficiencies and drop heights. Rollins et al. (2021) expanded the DPT database by incorporating 137 sites (80 with liquefaction and 57 without) related to 10 seismic events with magnitudes ranging from 5.8 to 9.2 across seven countries, including data from Cao et al. (2013), and recalculated the triggering curves of the liquefaction probability function.

In the study by Cao et al. (2013), the N_{120} is determined by taking the DPT resistance measured in blows per 0.3 m and multiplying it by ETR. Meanwhile, the was calculated by adding a threshold value of 1.7 to align the equation proposed by Cao et al. (2013) with theC_N value from Youd and Idriss (2001). The CSR is defined using the "simplified procedure" outlined by Seed and Idriss (1971), which incorporates the dependency of the r_d value on magnitude as per Idriss and Boulanger (2008). Rollins et al. (2021) introduced a new MSF correction factor, as well as a new logistic regression analysis was conducted to determine the probability of liquefaction occurrence, P_L. Similarly, Cao et al. (2011) made the initial effort to create probabilistic-based triggering curves for gravelly soils, analyzing 30 liquefaction sites and 17 non-liquefaction sites following the 7.9 magnitude 2008 Wenchuan earthquake. In 2022, Rollins et al. introduced a new set of curves derived from a broader data set. This expanded data set encompassed 96 liquefaction case histories and 78 non-liquefaction case histories from 17 earthquakes across 7 countries, with values ranging from 6.1 to 9.2. While these liquefaction triggering curves offer assessments based on direct field performance, they are limited by the scarcity of case histories with high and high values, which are necessary to define the upper branch of the triggering curves. The V_S-based method employs the same equations suggested by the aforementioned authors for SPT/CPT-based methods, but it incorporates a new MSF and a different regression approach to determine the P_L.

Using those methods it is possible to calculate the liquefaction potential using indices such as the Liquefaction Potential Index (LPI) proposed by Iwasaki et al. (1978), as in equation:

$$LPI = \int_0^{20} F(z)w(z)\Delta z \tag{3.13}$$

Where

$$w(z) = 10 - 0.5z \tag{3.14}$$

$$F(z) = 1 - FS \; if \; FS \leq 1 \; ; F(z) = 0 \; if \; FS > 1 \tag{3.15}$$

In considering the term "liquefaction" as the observation of the effects on the ground surface due to excess pore pressure (Δu) at depth, it is feasible to assess the likelihood of a given area to undergo liquefaction by examining the vertical settlements induced by the densification of non-cohesive granular layers within the first 20 meters of depth following the dissipation of Δu. Additionally, the horizontal displacement resulting from the reduction in shear strength on a gentle slope area, due to the increase of Δu at depth, can be evaluated. Simplified CPU-based methods developed by Zhang et al. (2002) and Zhang et al. (2004) facilitate the estimation of vertical settlements and horizontal displacement, respectively, potentially induced by soil liquefaction on the ground surface.

In Zhang et al. (2002) the vertical settlements of the ground resulting from liquefaction of surface layers are determined by correlating the values of $(q_{c1N})_{cs}$ and FS (Eq. 3.12) with the vertical deformation of the ground ε at a given depth z:

$$S = \sum_{i=1}^{j} \varepsilon_{vi} \Delta z_i \tag{3.16}$$

Where:

if $FS \leq 0.5$, $\quad \varepsilon_v = 102(q_{c1N})_{cs}^{-0.82}$ $\quad$ for $33 \leq (q_{c1N})_{cs} \leq 200$ $\quad$ (3.17a)

if $FS = 0.6$, $\quad \varepsilon_v = 102(q_{c1N})_{cs}^{-0.82}$ $\quad$ for $33 \leq (q_{c1N})_{cs} \leq 147$ $\quad$ (3.17b)

if $FS = 0.6$, $\quad \varepsilon_v = 2411(q_{c1N})_{cs}^{-1.45}$ $\quad$ for $147 \leq (q_{c1N})_{cs} \leq 200$ $\quad$ (3.17c)

if $FS = 0.7$, $\quad \varepsilon_v = 102(q_{c1N})_{cs}^{-0.82}$ $\quad$ for $33 \leq (q_{c1N})_{cs} \leq 110$ $\quad$ (3.17d)

if $FS = 0.7$, $\quad \varepsilon_v = 1701(q_{c1N})_{cs}^{-1.42}$ $\quad$ for $110 \leq (q_{c1N})_{cs} \leq 200$ $\quad$ (3.17e) if $FS = 0.8$, $\varepsilon_v = 102(q_{c1N})_{cs}^{-0.82}$ for $33 \leq (q_{c1N})_{cs} \leq 80$ (3.17f)

if $FS = 0.8$, $\varepsilon_v = 1690(q_{c1N})_{cs}^{-1.46}$ for $80 \leq (q_{c1N})_{cs} \leq 200$ (3.17g)

if $FS = 0.9$, $\varepsilon_v = 102(q_{c1N})_{cs}^{-0.82}$ for $33 \leq (q_{c1N})_{cs} \leq 60$ (3.17h)

if $FS = 0.9$, $\varepsilon_v = 1430(q_{c1N})_{cs}^{-1.48}$ for $60 \leq (q_{c1N})_{cs} \leq 200$ (3.17i)

if $FS = 1.0$, $\varepsilon_v = 64(q_{c1N})_{cs}^{-0.93}$ for $33 \leq (q_{c1N})_{cs} \leq 200$ (3.17j)

if $FS = 1.1$, $\varepsilon_v = 11(q_{c1N})_{cs}^{-0.65}$ for $33 \leq (q_{c1N})_{cs} \leq 200$ (3.17k)

if $FS = 1.2$, $\varepsilon_v = 9.7(q_{c1N})_{cs}^{-0.69}$ for $33 \leq (q_{c1N})_{cs} \leq 200$ (3.17l)

if $FS = 1.3$, $\varepsilon_v = 7.6(q_{c1N})_{cs}^{-0.71}$ for $33 \leq (q_{c1N})_{cs} \leq 200$ (3.17m)

if $FS = 2.0$, $\varepsilon_v = 0.0$ for $33 \leq (q_{c1N})_{cs} \leq 200$ (3.17n)

The liquefaction assessment is performed at the infrastructure scale (Fig. 3.17).

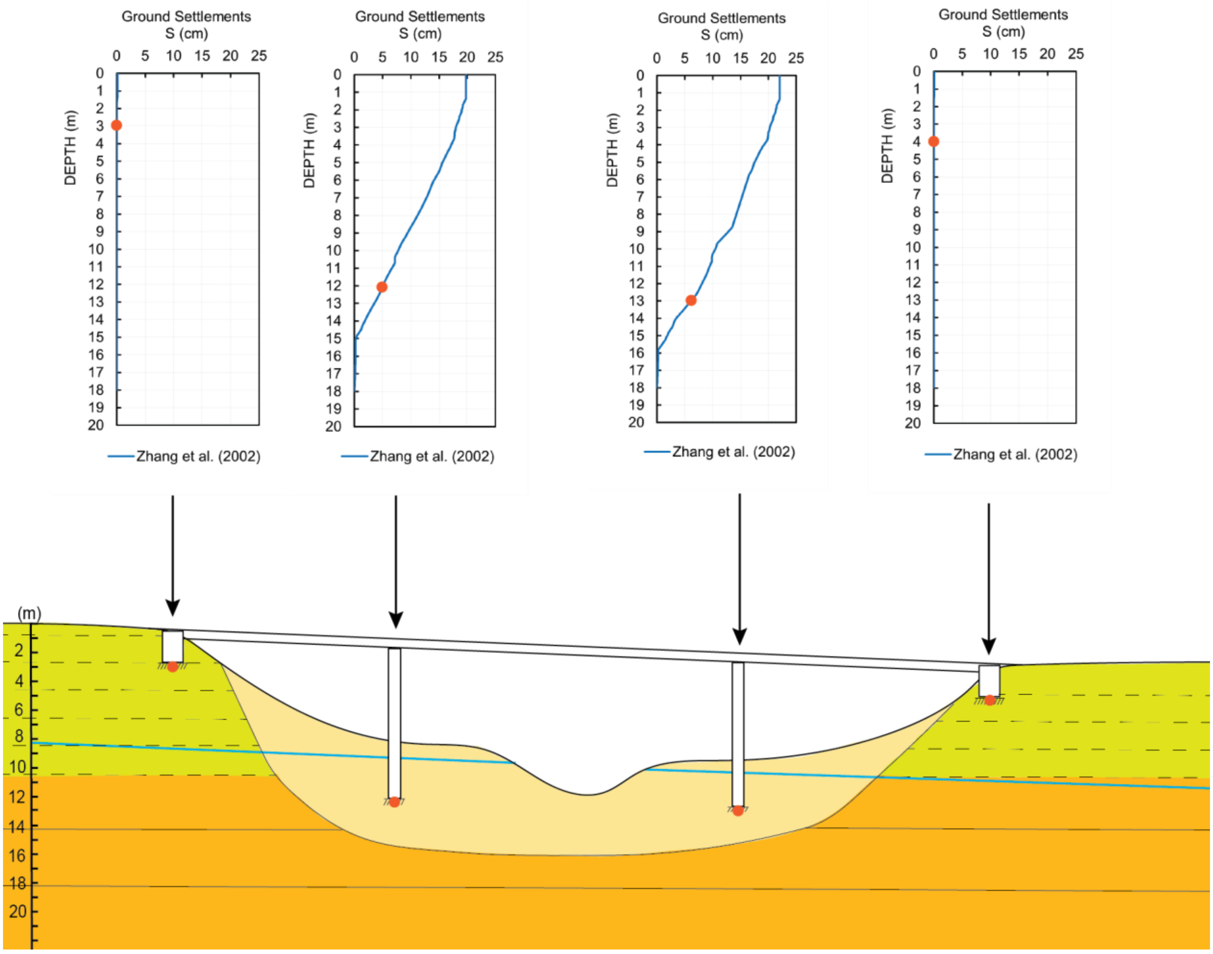

Fig. 3.17. Sketch of a bridge crossing a valley filled by alluvial soils showing typical results of liquefaction analyses in terms of permanent settlements at foundation levels. Yellow and orange polygons represent stratified consolidated deposits, while light-yellow depicts loose deposits. The cumulative ground settlements

according to Zhang et al. (2002) are plotted; orange circles depicted the foundations level; the blue line represents the ground water table.

In Zhang et al. (2004) SPT or CPT data are used to estimate the magnitude of lateral displacement associated with a liquefaction-induced lateral spread, introducing the Lateral Displacement Index (LDI) as in the following equations:

$$\mathrm{LDI} = \int_0^{z_{max}} \gamma_{max} dz \tag{3.18}$$

Where z_{max} is the maximum depth below the potential liquefiable layers, with a calculated $FS \leq 2.0$, with γ_{max} given by:

if $D_r = 90\%,\quad \gamma_{max} = 3.6 \cdot (FS)^{-1.80}$ for $0.7 \leq FS \leq 2.0$ (3.19a)

if $D_r = 90\%,\quad \gamma_{max} = 6.2$ for $FS \leq 0.7$ (3.19b)

if $D_r = 80\%,\quad \gamma_{max} = 3.22 \cdot (FS)^{-2.08}$ for $0.56 \leq FS \leq 2.0$ (3.19c)

if $D_r = 80\%,\quad \gamma_{max} = 10$ for $FS \leq 0.56$ (3.19d)

if $D_r = 70\%,\quad \gamma_{max} = 3.20 \cdot (FS)^{-2.89}$ for $0.59 \leq FS \leq 2.0$ (3.19e)

if $D_r = 70\%,\quad \gamma_{max} = 14.5$ for $FS \leq 0.59$ (3.19f)

if $D_r = 60\%,\quad \gamma_{max} = 3.58 \cdot (FS)^{-4.42}$ for $0.66 \leq FS \leq 2.0$ (3.19g)

if $D_r = 60\%,\quad \gamma_{max} = 22.7$ for $FS \leq 0.66$ (3.19h)

if $D_r = 50\%,\quad \gamma_{max} = 4.22 \cdot (FS)^{-6.39}$ for $0.72 \leq FS \leq 2.0$ (3.19i)

if $D_r = 50\%,\quad \gamma_{max} = 34.1$ for $FS \leq 0.72$ (3.19j)

if $D_r = 40\%,\quad \gamma_{max} = 3.31 \cdot (FS)^{-7.97}$ for $1.0 \leq FS \leq 2.0$ (3.19k)

if $D_r = 40\%,\quad \gamma_{max} = 250 \cdot (1.0 - FS) + 3.5$ for $0.81 \leq FS \leq 1.0$ (3.19l)

if $D_r = 40\%,\quad \gamma_{max} = 51.2$ for $FS \leq 0.81$ (3.19m)

Upon calculating the LDI, it is possible to estimate the Lateral Displacement (LD) as:

$$\mathrm{LD} = (\mathrm{S} + 0.2) \cdot \mathrm{LDI} \qquad \text{for } 0.2\% < S < 3.5\% \tag{3.20}$$

for gently sloping ground without a free face, were S is the ground slope in percent; or

$$\mathrm{LD} = 6 \cdot (L/H)^{-0.8} \cdot \mathrm{LDI} \qquad \text{for } 4 < L/H < 40 \tag{3.21}$$

for level ground with a free face.

Horizontal displacement (D_h) due to liquefaction-induced lateral spread can be determined by using the method proposed by Youd (2018) and reported in the following equations:

$$\log D_h = -16.713 + 1.532M - 1.406\log R^* - 0.012R + 0.592\log W + 0.540\log T_{15} + 3.413\log(100 - F_{15}) - 0.795\log(D50_{15} + 0.1mm) \tag{3.22}$$

for free face conditions, and

$$\log D_h = -16.213 + 1.532M - 1.406\log R^* - 0.012R + 0.338\log S + 0.540\log T_{15} + 3.413\log(100 - F_{15}) - 0.795\log(D50_{15} + 0.1mm) \tag{3.23}$$

for gently sloping ground conditions, where

$$R^* = R_0 + R \quad \text{and} \quad R_0 = 10^{(0.89M - 5.64)} \tag{3.24}$$

and D_h is the predicted lateral displacement in meters; M is the moment magnitude of the earthquake; R is the map distance from the site to the epicenter in kilometers; T_{15} is the cumulative thickness of saturated liquefiable layers with $(\mathrm{N}_1)_{60} < 15$, in meters; F_{15} is the average fine content (percent passing the No 200 sieve) for granular material within the T_{15} layer in percent; $D50_{15}$ is the average mean grain size for granular materials within the T_{15} layer in mm; S is the ground slope in percent; W is the free face ratio, in percent, defined as the ratio of the height of the free face to the horizontal distance (L) from the toe of the free face to a given point.

3.2.3. Slope Stability Analysis - Landslides

Simplified methods can be used to conduct slope-stability analyses to assess the probability of landslides or rockfalls induced by seismic activity. Regarding landslides, pseudo-static analysis (in which the effects of an earthquake are represented by constant horizontal and/or vertical accelerations) can be used first to derive the critical acceleration value (a_c), defined as the acceleration required to produce slope instability, that is the product of the critical seismic coefficient (k_c) and the acceleration of gravity (g). Newmark sliding block analysis (Newmark, 1965) can then be executed to predict the permanent displacements of slopes subjected to ground motion. In this analysis, a potential landslide is considered equivalent to a rigid block resting on an inclined plane. As an alternative to the Newmark analysis, there are many simplified prediction equations available in the literature (e.g., Crespellani et al., 1998) that link the displacement of the slope to the slope critical acceleration value and to several ground motion parameters representative of ground shaking. These equations were developed based on numerous parametric Newmark analyses (Fig. 3.18).

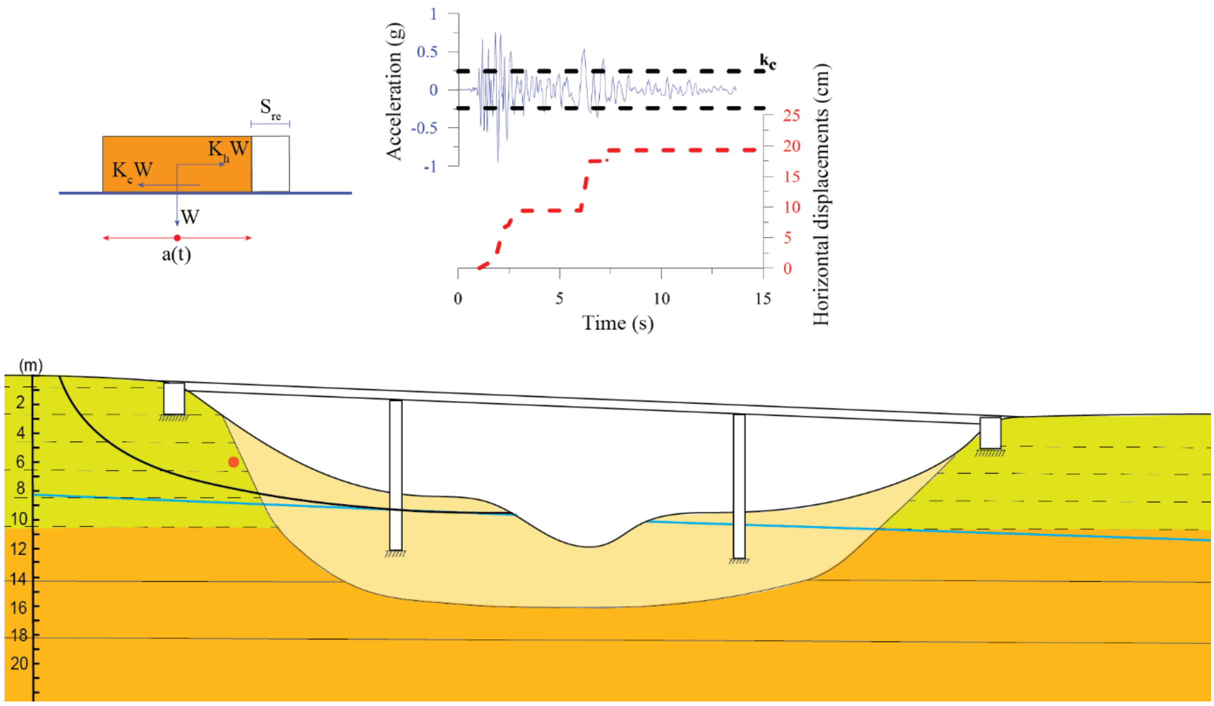

Fig. 3.18. Sketch of a bridge crossing a valley filled by alluvial soils showing typical results of Newmark slope analyses in terms of permanent displacements. The accelerogram a(t) is computed at the center of mass (orange point) of the potential landslide. k_c is the critical seismic coefficient (dashed blue line), W is the weight of the block corresponding to the instable mass, S_{re} is the horizontal permanent displacement of the instable mass at the end of the shaking. Yellow and orange polygons represent stratified consolidated deposits, while light-yellow depicts loose deposits, the black curve identify the detachment surface.

In addition, in recent literature are available physically-based probabilistic models and hybrid methods, by coupling data-driven methods, to assess landslide susceptibility (e.g., Ji et al., 2022; Pei and Qiu, 2024; Montrasio et al., 2023; Gatto et al., 2023).

3.2.4. Slope Stability Analysis - Rockfall

To assess rockfall hazard, it is crucial a geomechanical/morphological survey for the identification of the rockfall source zones (i.e., detachment niches). After that, simplified approaches or trajectographic numerical simulations are generally required to characterize the potential paths and movement characteristics of falling rocks. The key factors for the risk estimation include maximum travel distance, bounce height and translational velocity of the blocks at the impact instant. Numerical simulations of rockfall in three dimensions model the occurrence on a full 3D slope surface (e.g., Descoeudres and Zimmermann, 1987). Various software packages are available to implement these runout analyses (e.g., Chen et al., 2013). The strength of 3D models lies in their ability to integrate the shape of rock fragments and topography into the resulting dynamic behavior. Nevertheless, these models are limited by their need for numerous spatially explicit maps and substantial computational power. For this reason, two-dimensional models are the best solution to have an easy-to-use method to model the phenomenon with enough accuracy, using commercial software and a not so powerful computer.

The movements of a falling rock can be classified into freefall, bouncing, sliding, toppling, or rolling. Computer software has become increasingly popular for simulating the trajectory of a falling rock. Among these movements, the impact mode is the most critical yet intricate type of motion. When two objects come close to each other or when one approaches an infinite surface, they collide at a point known as the collision surface or impact area. During an infinitesimal time interval, the relative velocities of some nearby parts of the two objects become negative, indicating contact at that moment. The contact forces activated by the collision cause the objects to push apart, resulting in positive relative contact velocities. Any numerical model that aims to simulate the generation of impulses at the contact point and predict the velocities after rebounding is referred to as an impact model. Guzzetti et al. (2002) discussed various rockfall models developed over the past thirty years, classifying them into three main categories based on the impact model: lumped mass, hybrid, and rigid body.

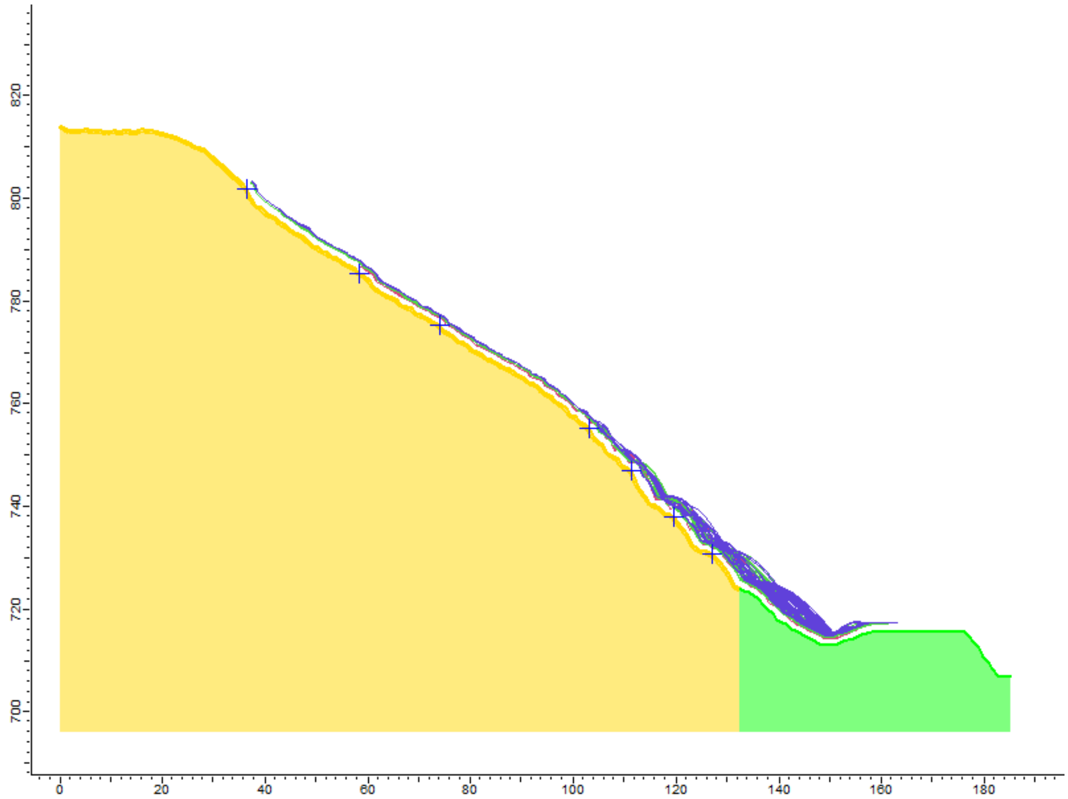

Fig. 3.19. Example of rockfall modeling using RocFall2D by Rocscience. The yellow polygon represents the rocky slope, while the green polygon indicates the alluvial deposits. The blue crosses denote the rock blocks feeds, and the blue, red, and green lines illustrate the trajectories of falling rock blocks with diameters of 1.2, 1.5, and 1.8 meters, respectively. The topographic profile is derived from a 1-meter resolution DTM obtained from LiDAR data, utilizing QGIS software.

In rockfall simulations, the most commonly used models are lumped-mass (or stereomechanical) models, which employ particle methods to concentrate the mass of a rock into a small particle. Other approaches include hybrid methods that utilize simplified impact models when a particle collides with a surface. The rockfall literature also features several rigid body models that consider simplified rock shapes and employ specific impact models. In this work, we use the code named RocFall2D by Rocscience based on the Rigid Body Model (Fig. 3.19), as in the theoretical framework introduced by Ashayer (2007).

3.2.5. Seismic Risk Evaluation Through Fragility Curves in Bridges/Viaducts

Upon obtaining the values of the peak ground acceleration, lateral displacements or rocks velocity, and vertical settlements, it is possible to assess the potential damage resulting from the interaction of these hazards with the linear structure using fragility curves (e.g., Brandenberg et al., 2011; Gardoni et al., 2002; Hawng et al., 2001). Furthermore, the probability of damage can be ascertained by considering four levels of intensity: slight, defined as the presence of minor fissures in the infrastructure without compromising its safety and stability; moderate, characterized by visible cracks in the infrastructure, although it may still be deemed accessible; extensive, indicating that the infrastructure is no longer accessible; and collapse, denoting the complete loss of functionality of the structure.

Fragility curves allow to assess the exceeding of pre-established damage status of a structure in probabilistic terms, by means of a relationship between an earthquake intensity measure, such as the PGA, and the probability that a specific level of damage is reached or exceeded (e.g., Brando et al., 2017; De Matteis et al., 2019). Several fragility curves for bridges are available in literature, developed considering the design of the structure, the way of failure, and the ground motion intensity parameters (or Intensity Measure, IM) which can cause damage. In this study, fragility curves available from literature are selected to assess the risk from rockfall (Xie et al., 2020) and ground shaking (Branderberg et al., 2011), using respectively the translational velocity of the falling blocks at the moment of the impact on the piles of the viaduct, and the PGA at foundation depth. Four scenarios of damage (slight, moderate, extensive, and collapse) are proposed for each secondary hazard identified in the selected area.

Brandenberg et al. (2011) investigated the fragility surfaces of demand for bridges located on liquefied and laterally spreading ground, which illustrate the probability P(EDP>edp|IM=im). This analysis involves a vector of Engineering Demand Parameters (EDP) and considers the intensity measure (IM) as the displacement of the ground due to lateral spreading in a free field. To simulate the responses of bridges affected by lateral spreading caused by liquefaction, they conducted an equivalent global nonlinear finite element analysis (Fig. 3.20). Additionally, nonlinear dynamic time-history analyses were employed to evaluate the response resulting from seismic shaking.

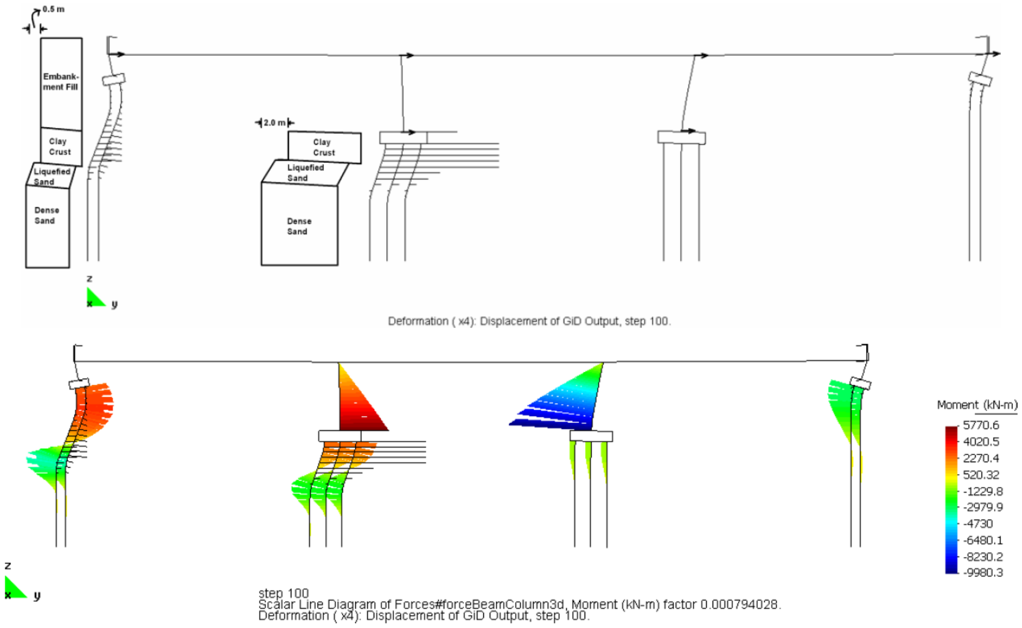

Fig. 3.20. Example of Global Equivalent Static Analysis on a bridge model, showing load patter and deformed mesh (top), and deformed mesh and moment distribution in nonlinear beam column elements (bottom), with deformations amplified by a factor of 4.0. From Brandenberg et al. (2011).

In Brandenberg et al. (2011), bridges are classified based on the type of superstructure, how the superstructure connects to abutments and piers, number of columns per pier, pile type and the age of the bridges (Fig. 3.21).

Six bridge models (Fig. 3.22) were selected to represent the most common types of highway bridges, each featuring different configurations of a multi-span straight bridge with single column construction. Model E1 illustrates a continuous bridge with monolithic abutments. In contrast, models E2 through E6 are equipped with seat-type abutments. Model E2 shows a continuous bridge with seat-type abutments, while Model E3 is similar to Model E2 but includes an expansion joint at the center of the mid-span. Model E4 is isolated at the pier tops with a continuous deck, whereas Model E5 incorporates both an expansion joint at the mid-span and isolation. In Model E6, simply supported connections are used at the pier top, and the adjacent decks are pin-connected to prevent collapse. The structural characteristics of these bridge components are derived from two actual bridges constructed before 1971, thus reflecting the features of older bridges designed prior to the implementation of modern seismic codes.

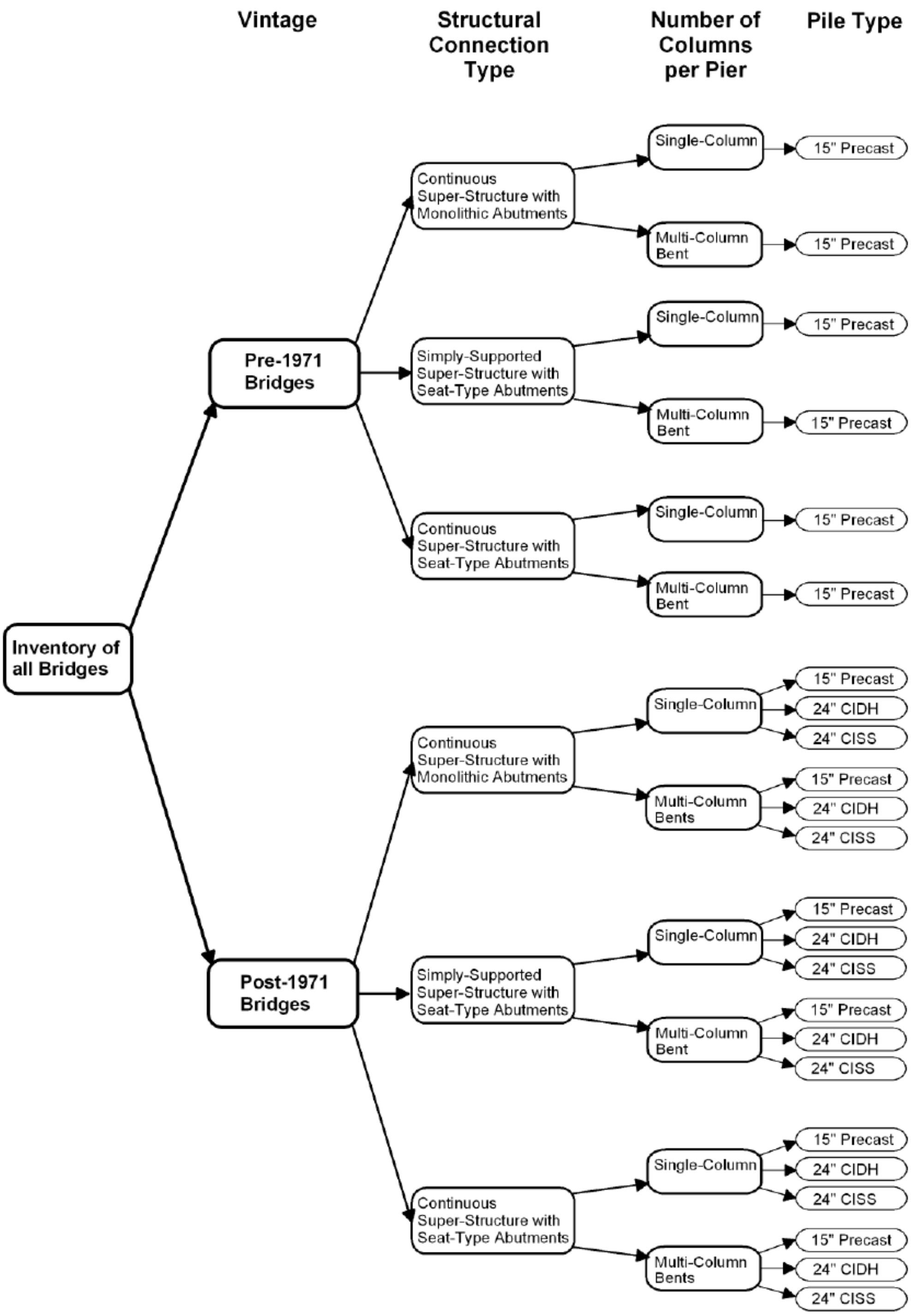

Fig. 3.21. Classification of bridges based on vintage, structure type, number of piers and type of piles, as used in development of fragility curves by Brandenberg et al. (2011). CISS stands for concrete cast-in-situ (non-displacing) piles; CIDH is concrete Cast-In-Drilled-Hole piles.

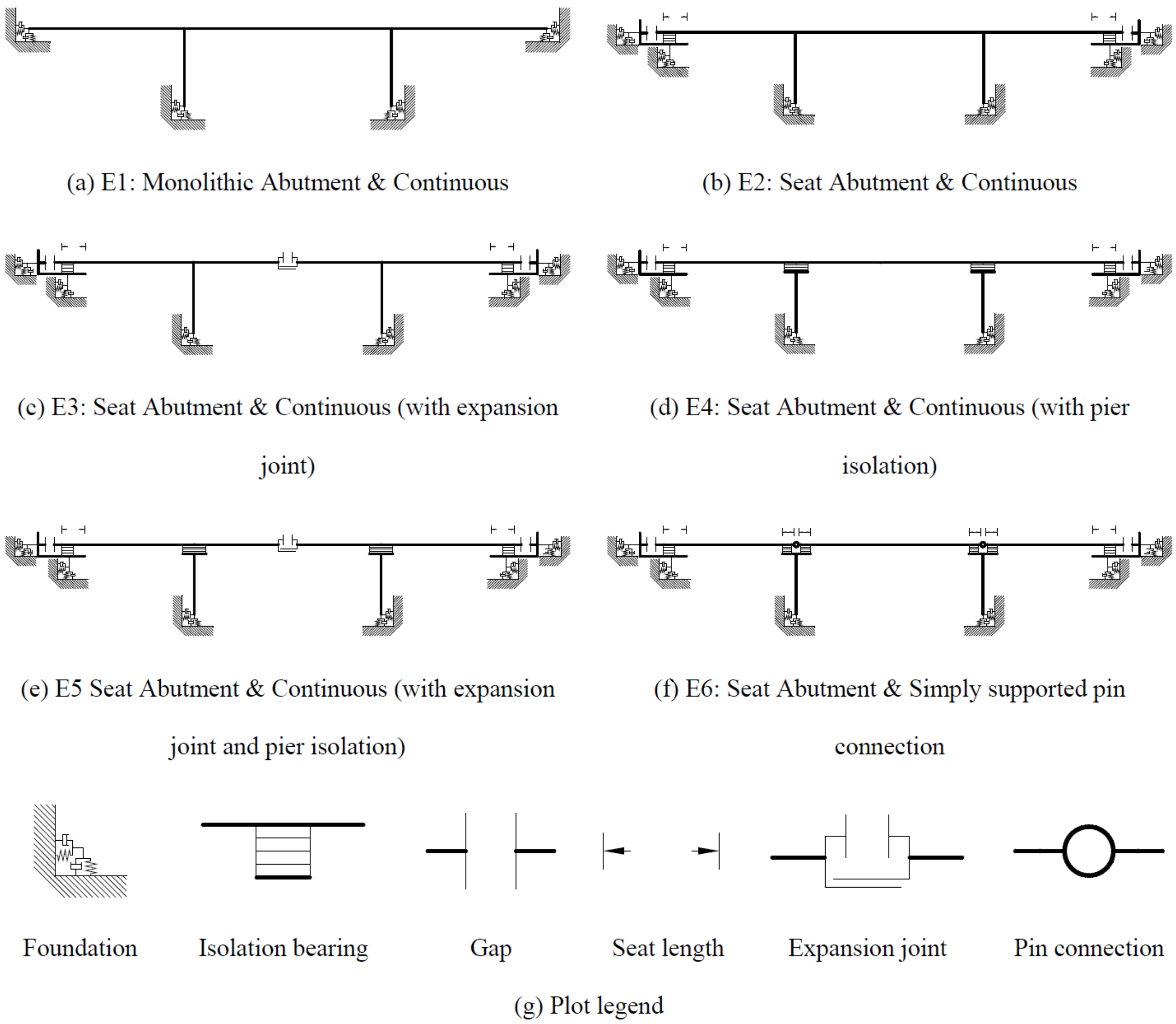

Fig. 3.22. Sketches of the six bridge models as reported in Brandenberg et al. (2011).

To account for the variability in structural and geotechnical conditions at specific bridge test locations, model input parameters were depicted as random variables. Nonlinear equivalent static analyses were performed using inputs that were randomly selected through the Monte-Carlo simulation technique. The fragility curves for ground shaking (Fig. 3.23) and lateral spreading (Fig. 3.24) were thus developed considering four different damage scenarios: slight, moderate, extensive, and collapse, and were therefore used in this study as the final step in level 2 analyses, for the determination of expected damage in the event of a seismic event, with consequent ground shaking and liquefaction-induced lateral spread. The intensity measure parameters adopted in the fragility curves are PGA and PGD, respectively. PGA is the Peak Ground Acceleration, i.e. the maximum value of the acceleration during the seismic shaking while PGD represents the Permanent Ground Displacement i.e. the horizontal displacement at the end of shaking due to lateral spreading.

These curves were chosen for this thesis because they were generated by considering a wide range of structural and geotechnical configurations. This means they allow for a good and reasonable approximation in assessing the probability of damage to a given structure.

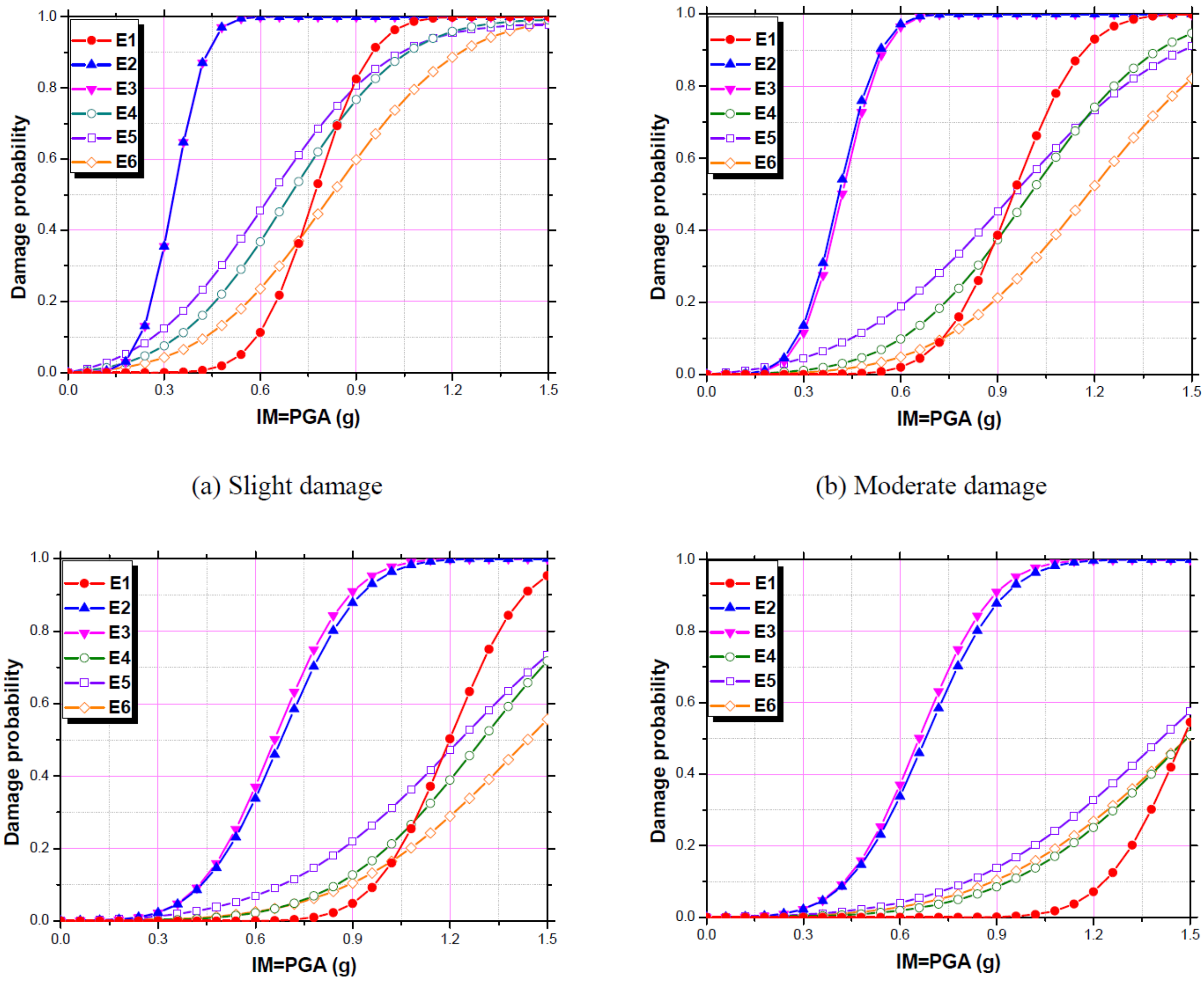

(a) Slight damage

(b) Moderate damage

(c) Extensive damage

(d) Collapse damage

Fig. 3.23. Fragility curves of the six bridge models in Figure 3.22, under seismic shaking. IM stands for Intensity Measure, PGA is the peak ground acceleration in g. From Brandenberg et al. (2011).

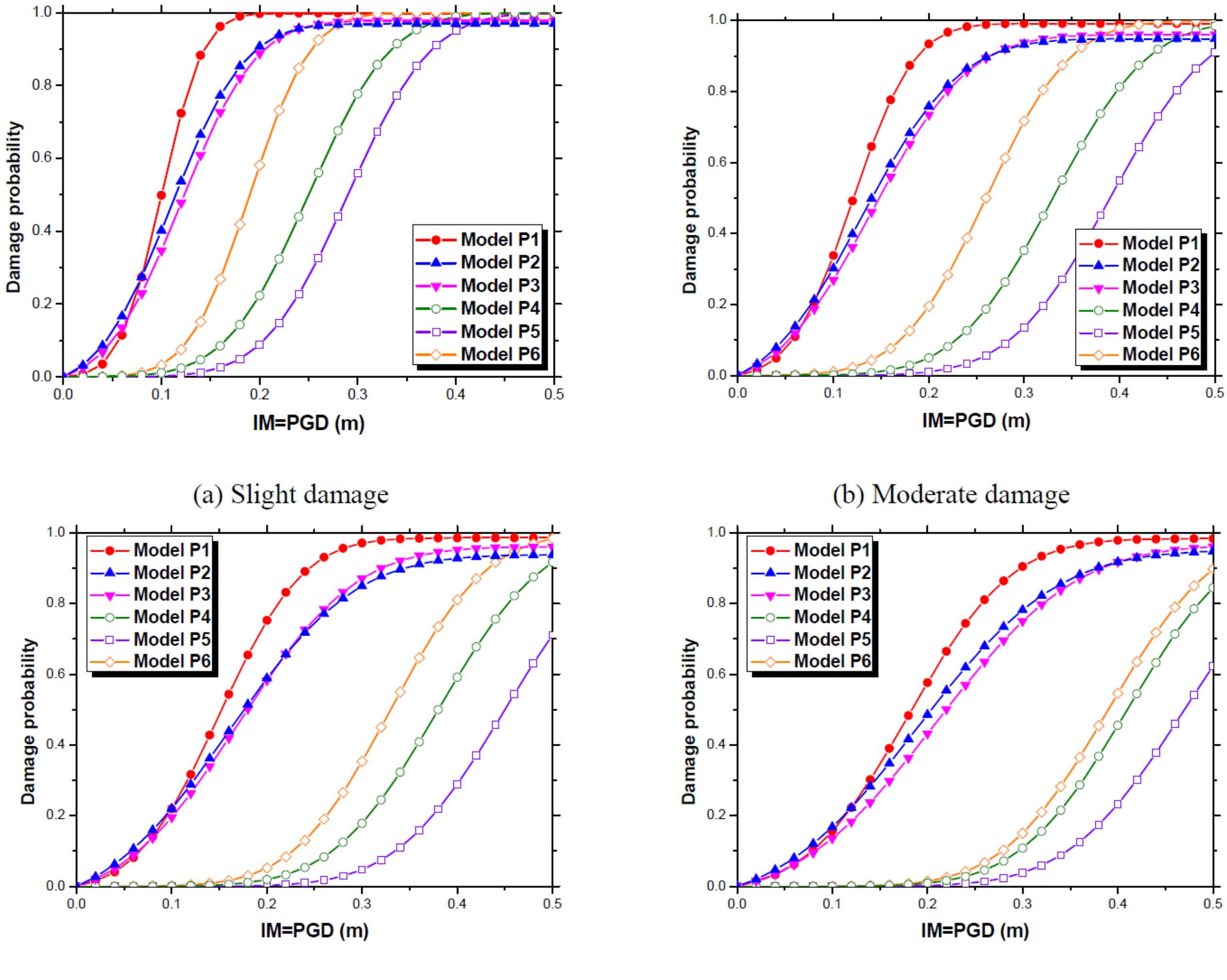

(a) Slight damage (b) Moderate damage

(c) Extensive damage (d) Collapse damage

Fig. 3.24. Fragility curves of the six bridge models in Figure 3.22, under lateral spreading. IM stands for Intensity Measure, PGD is the permanent ground displacement in meters. From Brandenberg et al. (2011).

Among the various works available in the literature for the assessment of rockfall impact damage on bridges (e.g., Cao et al., 2024, Sun et al., 2023), it was decided to use, for the case studies in this thesis, the curves proposed by Xie et al. (2020). In this research, the authors investigate the dynamic responses and vulnerability of bridge columns with different cross-sectional shapes when exposed to various rockfall impacts, considering the blocks' diameters, impact speeds, and heights of the rockfalls. The study concentrated on circular and square reinforced concrete (RC) columns, which are the most common in bridge construction, and developed detailed finite element (FE) models. The analysis meticulously examined how rockfall diameter, impact speed, and impact height affect the dynamic responses of the columns, such as impact force, lateral displacement, and remaining axial capacity. A vulnerability analysis method is devised using a response surface model and Monte Carlo simulations to evaluate bridge columns under rockfall impacts. The vulnerability analysis results for the two types of bridge columns are presented. To provide a practical reference for impact analysis, a real bridge structure was selected and slightly modified, considering an 11-span continuous girder bridge, with each span measuring 30 meters in length. This structure was therefore used for modeling, repeating the analyses and laboratory tests with only the shape of the piles modified. The circular column has a diameter of 1.2 m and a height of 10 m, while the square column is designed based on the area equivalence of circular and square sections (Fig.3.25). Additionally, both circular and square columns utilize the same longitudinal and transverse steel reinforcement ratios. For transverse reinforcement, spiral stirrups are used in the circular columns, whereas rectangular hoop reinforcements are employed in the square columns.

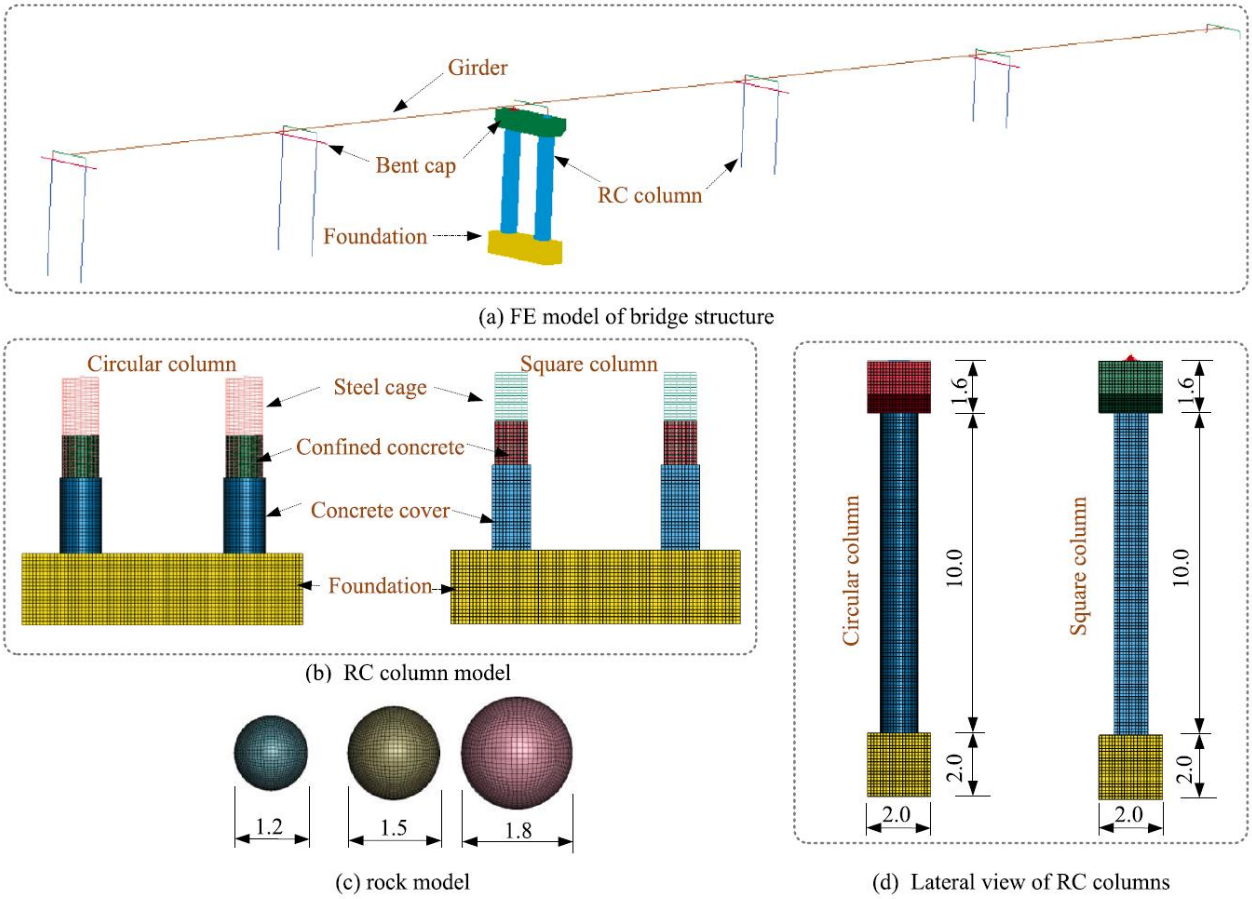

Fig. 3.25. Detailed FE model of the bridge structure under rockfall impact established using LS-DYNA based on the layout of the bridge. Measure unit meters. From Xie et al. (2020).

To enhance computational efficiency, a simplified beam model is utilized for the superstructure and the columns not affected by impact (Fig. 3.25 a). Solid elements are employed to represent the impacted column, foundation, and cap beam, while beam elements are used for the longitudinal and transverse reinforcements. Since bridges exposed to rockfall impacts are typically found in mountainous regions with generally favorable geological conditions, Xie et al. (2020) did not account for soil–pile interaction. In other words, geotechnical problems related to settlements or landslides were not addressed. The only source of geotechnical risk is due to the rockfall phenomena.

The main damage is usually concentrated in the bridge column, while the effects on other parts, such as the cap beam, foundation, superstructure, and additional columns, are relatively minor. To enhance computational efficiency, these unaffected sections are modeled using an elastic material approach. A spherical model is used to depict the rockfall, and rock blocks with diameters of 1.2 m, 1.5 m, and 1.8 m are analyzed to assess the impact of rockfall size, as illustrated in Figure 3.25c. Rock parameters such as Young's modulus, mass density, and volume, are derived from existing literature. The rock block is assumed to be made of granite, and a rigid body model is employed to conservatively simulate the bridge structure's response to a rockfall impact. For the bridge columns, normal concrete with a strength grade of C40, as specified in China's design code, is used.

Xie et al. (2020) conducted an in-depth investigation into the dynamic responses of columns with various cross-sections when subjected to rockfall impacts, utilizing detailed FE simulations. In these simulations, the primary parameters varied were the rockfall's diameter, the velocity of impact, and the height from which it fell. A total of 12 scenarios were analyzed to evaluate how these key factors influenced the dynamic behavior of bridge columns, considering an impact velocity range of 5–20 m/s. Studies of rockfall incidents in China's western mountainous regions have shown that impacts on bridge columns typically occur at or below the midpoint of the columns. Therefore, for a bridge column with an overall height of 10 m, the impact heights were set between 1 m and 5 m. Given the numerous potential impact angles in rockfall incidents involving bridge columns, where any angle is possible, the transverse direction was chosen as the initial impact angle to explore the dynamic behaviors and vulnerability of both circular and square columns. Ultimately, the authors concluded that the lateral displacements of both column types increase as the rockfall diameter, impact velocity, and impact height rise.

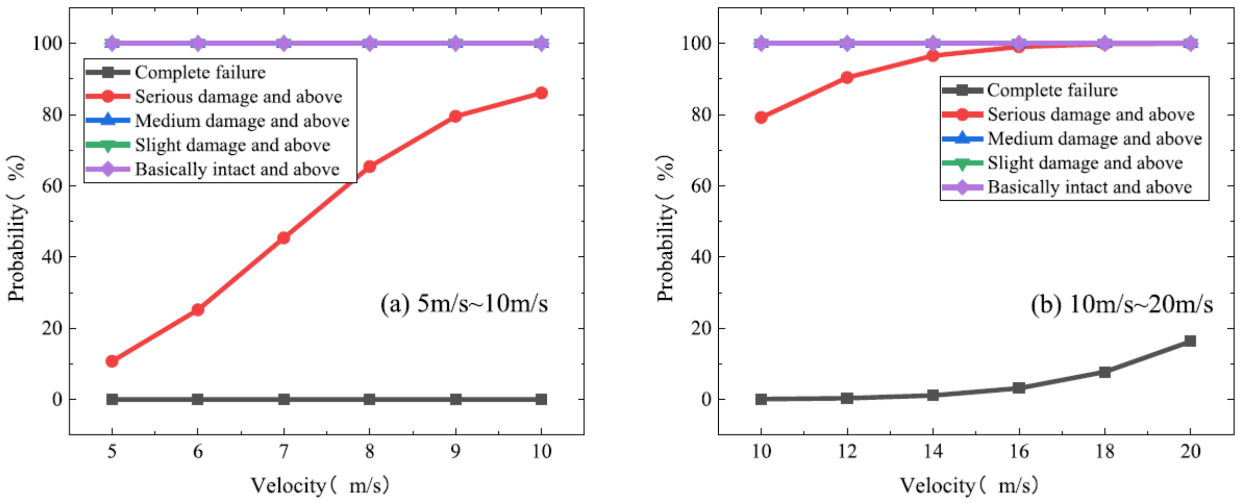

Fig. 15. Failure probability versus impact velocity of circular column.

Fig. 3.26. Fragility curves developed by Xie et al. (2020) for bridges with circular-section piers; (a) impact velocity range between 5 and 10 m/s; (b) impact velocity range between 10 and 20 m/s.

In summary, the authors, considering the data available in the literature, those obtained from direct laboratory tests on columns with the characteristics of the model under consideration, and numerical modeling of the impacts, developed fragility curves for piers with circular (Fig. 3.26) and square (Fig. 3.27) cross-sections, using the impact velocity of the rock blocks as the parameter for damage assessment.

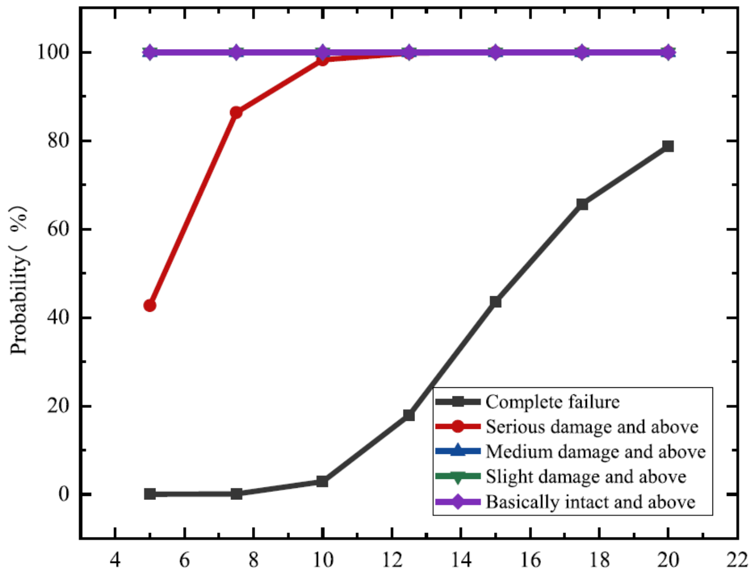

Fig. 3.27. Fragility curves developed by Xie et al. (2020) for bridges with squared-section piers; impact velocity range between 5 and 20 m/s.

3.3. Formulation of the GETI Index

Multi-hazard risk assessment in linear infrastructure, such as bridges and viaduct, are mostly based on a statistic approach (e.g., Kameshwar and Padgett, 2014), using the total probability theorem to calculate the overall risks, but conducted the assessment separately for each hazard considered.

In current methodology, the overall risk is computed, for each considered hazard, by convolution of hazard curve and the corresponding fragility (e.g., ASCE, 2017). As an example, the equation proposed by Kameshwar and Padgett (2014) in earthquake-hurricane combined risk assessment is reported. In this study, the authors considered the annual probability of failure of a bridge subjected to the two hazards. The general formulation of the annual risk of failure for each hazard is given by equation 3.25:

$$P_f = \int P_{(f|\lambda)} \left| \frac{dH(\lambda)}{d\lambda} \right| d\lambda \qquad (3.25)$$

in which λ is a hazard intensity parameter, $P_{(f|\lambda)}$ is the fragility curve, and $H(\lambda)$ represents the hazard curve. The hazard curve illustrates the likelihood of surpassing a certain threshold annually within the intensity measure domain used to define the external hazard. The fragility curve for fundamental events is derived from empirical, experimental, and/or numerical simulation data, showing the conditional probability of failure at each level of hazard intensity.

As seen before (§2.2), the limitation of this kind of approach is that it does not consider interaction between hazards and the possible effects on the structure of the simultaneous occurrence of more than one hazard. Furthermore, cascade effects are not evaluated. Another issue may be the asynchronous occurrence of hazards, that may affect the structure with enough delay time to let the damage on the structure not to be considered as independent.

Kwang et al. (2017, 2018) made a step over, considering a hybrid model of BN and FTA applied to multi-hazard risk assessment, in order to take into account the actual total probability of damage in case of the simultaneous occurrence of two natural hazards, even if they still do not considered the possibility of interaction between hazards, and how one of them can trigger or enhanced the other.

The BN is widely use in civil structural engineering to represent the effects of an event on a structure, considering the failure system. It is based on the Bayes Theorem, that can be defined (e.g., Blitzstein and Hwang, 2015) as follows:

$$P(A|B) = \frac{P(A \cap B)}{P(B)} \tag{3.26}$$

where A is the event whose uncertainty we want to update, and B is the evidence we want to treat as given. We call P(A) the prior probability of A, intended as before updating, and P(A|B) the posterior probability of A, considered after updating based on the evidence.

By moving the denominator in the definition to the other side of the equation, we can obtain that:

$$P(A \cap B) = P(B)P(A|B) \tag{3.27}$$

If P(A) > 0 and P(B) > 0, then this is equivalent to P(A|B) = P(A), and also equivalent to P(B|A) = P(B). If events A and B are independent, the above relation can be written as:

$$P(A \cap B) = P(A)P(B) \tag{3.28}$$

From this, we can say that two events are independent if we can obtain the probability of their intersection by multiplying their individual probabilities. If $P(A \cap B) \neq 0$, it's true that they are compatible, so they can take place simultaneously. However, the likelihood of A happening doesn't influence the likelihood of B happening, or vice versa.

By considering three events A, B, and C, they can be defined independent if all of the following equations are verified:

$$P(A \cap B) = P(A)P(B) \tag{3.29a}$$

$$P(A \cap C) = P(A)P(C) \tag{3.29b}$$

$$P(B \cap C) = P(B)P(C) \tag{3.29c}$$

$$P(A \cap B \cap C) = P(A)P(B)P(C) \tag{3.29d}$$

In Bayesian approach, as P(A|B)=P(A∩B)/P(B), the probability of B is given by the Total Probability Theorem, written as follow:

$$P(B) = P(B|\mathrm{A})P(B) + P(\mathrm{B}|\bar{A})P(\bar{A}) \tag{3.9}$$

where $\bar{A}$ is the complementary of A, so the likelihood that A does not happened.

Given this, BN are probabilistic graphical models consisting on nodes (circles) representing random variables and links (arrows) representing conditional probability relationships (dependence). In that way, it is possible to schematize the probability of damage on a structure in terms of the conditional probability that a parameter of the fragility is generated by a given event (Bensi et al., 2011).

A generic BN can be represented as in Figure 3.28:

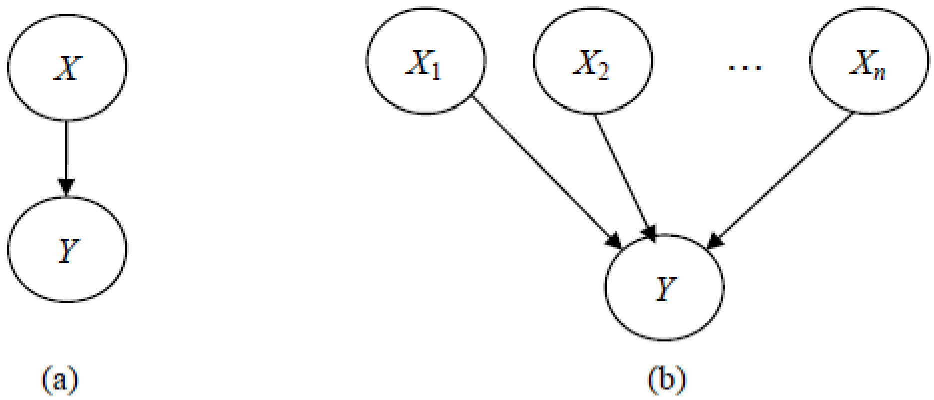

Fig. 3.28. (a) Two-node BN with Y dependent on X, and (b) BN with Y dependent on a vector of randon variables $X = \{X_1, \ldots, X_n\}$. From Bensi et al. (2011)

it is possible to calculate the Joint Probability as:

$$P(X_1,\ X_2,\ \ldots, X_n) = \prod_{i=1}^{n} P(X_i\,|Parents(X_i)) \tag{3.30}$$

$Parents(X_i)$ is parent nodes for X_i; $P(X_i|Parents(X_i))$ is the CPT of X_i, and *n* is the number of nodes in the network (e.g., Kwang et al., 2018). Typically, the new information comprises operational data, which includes whether an accident or primary event has occurred. Eq. 3.30 can be applied for either predicting probabilities or updating them. In predictive analysis, conditional probabilities such as *P(accident|event)* are calculated, representing the likelihood of a specific accident occurring given the occurrence or non-occurrence of a particular primary event. Conversely, in updating analysis, probabilities of the form *P(event|accident)* are assessed, indicating the likelihood of a specific event occurring given the occurrence of a certain accident. (Khakzad et al., 2011).

As seen before, Kwang et al. (2016, 2018) determined the system-level fragility using the FTA. A FTA diagram is a graphical decomposition of an undesirable event representing system failure (denoted as top event TE) into intermediate events and basic events through the use of logical gates (AND and OR gates). An example of simple FTA model is given in Figure 3.29.

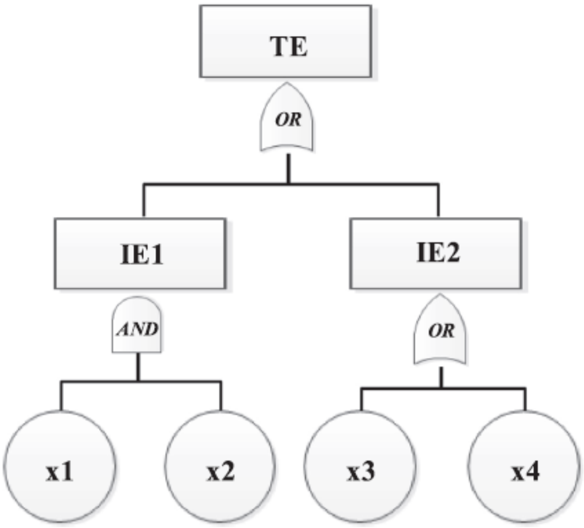

Fig. 3.29. Example of FTA: x1, x2, x3 and x4 represent four basic events; IE1 and IE2 are the intermediate events produced through combination of basic events by logic gates; AND and OR are the logic gates. From Kwang et al. (2016)

The basic events are characterized by Boolean states that represent “failure ”or “safe ”states, and are considered to be statistically independent as well. They are connected through the logic gates to characterize intermediate events which are also connected through the logic gates. To begin with, a qualitative evaluation is used to develop the logical expression for the TE. Boolean algebra is used to obtain the minimal cut- sets.

The order of a minimal cut-set is the number of basic events that contribute to the particular minimal cut-set. For illustration purposes, let us consider the example of a simple fault tree shown in Figure 3.29. In this figure, x1, x2, x3 and x4 represent four basic events. The IE1 and IE2 are the intermediate events produced through combination of basic events by logic gates. Therefore, we can write a logical expression for the top event as: $TE = (x1 \cap x2) \cup (x3 \cup x4)$. The corresponding Boolean algebra is $TE = (x1 \cdot x2) + (x3 + x4)$ and a total of 3 minimal cut-sets exist namely, $x1 \cdot x2$, x3, and x4. The minimal cut-sets x3 and x4 are of first order and the minimal cut-set $x1 \cdot x2$ is of second order. Finally, a quantitative analysis is conducted to compute the probability of occurrence of the TE and determine the importance measure for each minimal cut-set.

The probability of occurrence of the TE is calculated by using following equation (Eq. 3.31):

$$P(TE) = P\left(\bigcup_{j=1}^{n} M_j\right)$$

$$= \sum_{i=1}^{n} P(M_i) - \sum_{i<j=2}^{n} P(M_i M_j) + \sum_{i<j<k=3}^{n} P(M_i M_j M_k) + \cdots + (-1)^{n-1} P(M_i M_j \ldots M_n) P(M_j) \tag{3.31}$$

where M_1, M_2, …, M_n represents the minimal cut-sets and n is the total number of minimal cut-sets. The importance measure analysis calculates the contribution of the minimal cut-sets to the occurrence of TE and accordingly identifies the critical events.

The mapping algorithm integrates both graphical and numerical components. In the graphical mapping process, primary events, intermediate events, and the top event of the FTA are represented as root nodes, intermediate nodes, and the leaf node in the corresponding Bayesian Network (BN), respectively. The nodes within a BN are interconnected in a manner analogous to the corresponding components in the FTA. In the numerical mapping process, the occurrence probabilities of the primary events are assigned to the corresponding root nodes as prior probabilities. For each intermediate and leaf node, a conditional probability table is constructed, with these conditional probability tables being developed based on the type of gate. Figure 3.30 illustrates the simplified procedure for mapping FTAs into BNs (Khakzad et al., 2011).

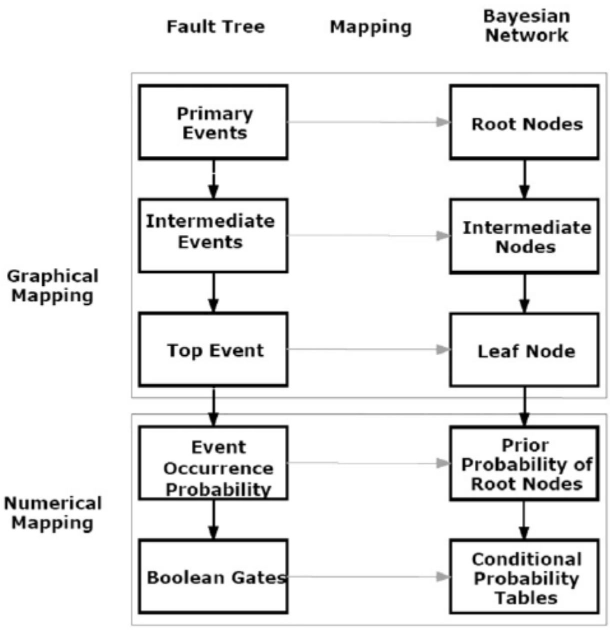

Fig. 3.30. simplified procedure for mapping FTAs into BNs. From Khakzad et al. (2011).

From this, Kwang and Gupta (2017) proposed a structural system failure under multi-hazard conditions model, using a hybrid approach between BN and FTA and considering earthquake, wind, and flood induced failures, connected by the logic gate “OR”, obtained the total probability of failure as in equation 3.31. In this approach, the effects of the three phenomena are considered independent, and the risk is calculated as the annual probability of occurrence of the events.

In the above proposed statistic methods for multi-hazard risk assessment on structure it is possible to notice that, as the random variables are considered Booleans, only the system failure is considered and only for the action of the hazard acting separately. In this view, in example, the effect of the occurrence of an earthquake is evaluated only in terms of ground shaking, while its secondary effects, such as soil liquefaction and landslides, are not considered. Thus, to express the concept of the “cascade effect” in mathematical terms, the damage derived, in this case, from ground shaking, liquefaction, and landslide/rockfall, considered as secondary effects of the occurrence of an earthquake, can be described by the conditional probability (§2.3.2). The ground shaking (S) is a secondary effect of the occurrence of an earthquake, considered as the rupture of a rock block at depth, with the propagation of seismic waves to the surface. The ground shaking can trigger soil liquefaction/lateral spreading (LQ), landslides (L), and/or rockfall (R) (e.g., Yeats at al., 1997; Kramer and Stewart, 2025), potentially lead to permanent ground deformations that can have effects on the infrastructure.

In this view, the model was developed by first considering the dependence of soil liquefaction, landslide, and rockfall on ground shaking (§3.1.2), which is a necessary but not sufficient condition for the development of other secondary effects. In fact, the occurrence of liquefaction phenomena (also understood as lateral spreading), landslides, and rockfall is also linked to a series of predisposing conditions, such as the presence of a shallow water table, stratigraphic conditions (e.g., loose granular deposits, contrast between cohesive cover and rocky slope, intensely fractured rocky slope, ...), or morphological conditions (e.g., saturated loose granular deposits with slight slope) that are suitable. These conditions are taken into account during the initial phases of Level 1 (§3.1), in order to determine the hazards that can reasonably be expected to occur and to potentially impact the structure. For this reason, the model has been simplified by not highlighting the predisposing conditions other than the occurrence of ground shaking.

Furthermore, landslides and rockfall have been considered as two separate hazards, taking into account the fact that they are two completely different physical phenomena, with predisposing factors and occurrence dynamics that do not overlap (§3.1.2.4). Moreover, while for rockfall the geotechnical parameter used to determine the expected damage to the structure is the impact velocity of the blocks against it, for landslides it is the horizontal displacement of the foundation soil or the piers. The fragility curves used for the two phenomena are therefore distinct and based on different physical phenomena, considering that the effects on the structure resulting from horizontal displacement (landslide) and direct impact of rock blocks (rockfall) are different and distinguishable (3.2.4). Instead, with regard to the occurrence of liquefaction-induced lateral spread and certain types of earthquake-induced landslides, it is possible for there to be an overlap due to their simultaneous and overlapping effects on bridge foundations. In the model, this overlap is addressed through the use of a fragility surface that assesses the concurrent occurrence of the two phenomena, using the same parameter defined as the permanent horizontal displacement.

The theoretical formulation of the GETI Index is based on PGM model (§2.3.2), as it is shown in Figure 3.31: Given the occurrence of an earthquake (E), with a defined scenario of a return period, the induced ground shaking (S) may trigger liquefaction (LQ) and/or landslides (L)/rockfall (R). S, LQ, L and R circles represents the susceptibility of a given area to the hazards. δ_{LQ}, δ_{LS}, δ_L, δ_R, and δ_S represents the expected values of the effects, respectively, of soil liquefaction, lateral spreading due to soil liquefaction, landslide, rockfall, and ground shaking; D_{LQ}, D_H, D_R, and D_S are the probability of damage on a bridge/viaduct for LQ, L, R and S respectively, and represent the minimal cut-sets of the FTA. The logic door "OR" explain the connection between the four damages and lead to the total damage D; Blue circles represent the observed nodes, the yellow circles depict the query nodes; Red circles represent the primary cause (earthquake) and the final effect (the total damage).

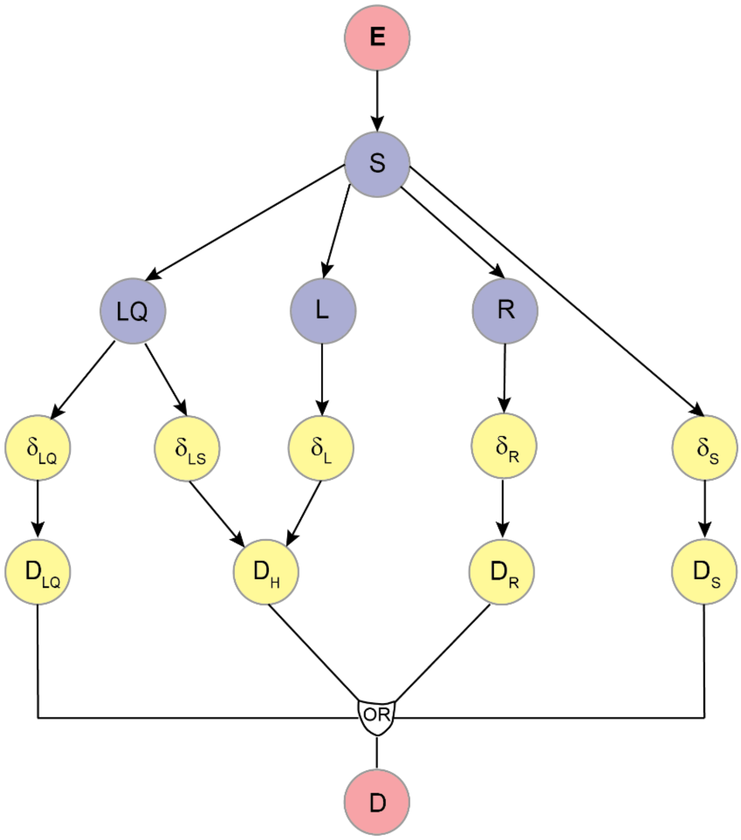

Fig. 3.31. PGM of the GETI.

Thus, using the theorem of total probability, the probability of damage derived from exceeding a value of PGA (ground shaking), vertical settlements (liquefaction), horizontal displacement (lateral spred/landslide), falling rocks impact velocity (rockfall) can be obtained as in Eqs. 3.32 a, b, c, and d respectively:

$$P(D_S > d_S) = \int_S \int_{\Delta_S} P(D_S > d_S|\Delta_S = \delta_S)p(\delta_S|S = s)p(S)d\delta_S dS \tag{3.32a}$$

$$P(D_{LQ} > d_{LQ}) = \int_S \int_{LQ} \int_{\Delta_{LQ}} P(D_{LQ} > d_{LQ}|\Delta_{LQ} = \delta_{LQ})p(\delta_{LQ}|LQ = lq)p(S = s)\, p(lq|s)p(s)d\delta_{LQ} dlq ds \tag{3.32b}$$

$$P(D_H > d_H) = \int_S \int_{LQ,L} \int_{\Delta_{LS},\Delta_L} P(D_H > d_H|\Delta_{LS} = \delta_{LS}, \Delta_L = \delta_L)p(\delta_{LS}|LQ = ls)p(\delta_L|L = l)p(S = s)p(ls, l|s)p(s)d(\delta_{LQ}, \delta_L)d(ls, l)ds \tag{3.32c}$$

$$P(D_R > d_R) = \int_S \int_R \int_{\Delta_R} P(D_R > d_R|\Delta_R = \delta_R)p(\delta_R|R = r)p(S = s)p(r|s)p(s)d\delta_R drds \tag{3.32d}$$

Where $p(s)$ is the probability density function (PDF) of shaking (from a hazard model, e.g., seismic hazard curve); $p(\delta_S|S = s)$, $p(\delta_{LQ}|LQ = lq, S = s)$, $p(\delta_{LS}|LQ = ls, \delta_L|L = l, S = s)$, $p(\delta_R|R = r, S = s)$ are the conditional PDF of effects given, respectively, by ground shaking, soil liquefaction, landslide and liquefaction-induced lateral spread, rockfall (soil response model); $P(D_S > d_S|\Delta_S = \delta_S)$, $P(D_{LQ} > d_{LQ}|\Delta_{LQ} = \delta_{LQ})$, $P(D_H > d_H|\Delta_{LQ} = \delta_{LS}, \Delta_L = \delta_L)$, $P(D_R > d_R|\Delta_R = \delta_R)$ are the conditional probability that damage exceeds a threshold given a PGA value, vertical settlements, horizontal displacements. or block velocity respectively (fragility function). LQ, L and R are considered as variables that describe soil properties, thus values of ground deformation and/or, e.g., rock blocks velocity, depend on LQ/L/R as well as on S.

The application of a hybrid BN-FTA model, proposed and validated by Kwang et al. (2017, 2018), allows us, through the use of the minimal cut-set (Eq. 3.31), to maintain the condition of independence of the effects and, therefore, to apply conditional probability to calculate the expected damage to a structure in the event of an earthquake. Indeed, the four secondary hazards can be considered as acting simultaneously on the infrastructure. However, when liquefaction-induced lateral spreading and landslides occur in the same location at the same time, their combined effects on the structure can overlap, leading to indistinguishable damage. For this reason, the overall damage (D_H) caused by the two phenomena, and due to horizontal displacements of the foundation soil and piles, is considered as the total damage resulting from lateral spreading and that from landslides. In this way, the resulting damages will be simultaneous and non-overlapping, so the occurrence of one of them does not influence the damage resulting from another From this perspective it is possible to consider D_S, D_{LQ}, D_H and D_R as they are independent (Fig. 3.30), and the total probability of damage can be calculated using the equation 3.31.

The probability of occurrence of shaking can be considered as the probability of occurrence of the earthquake, since we always have ground shaking in case of earthquake, or as the probability to have ground motion (GM) parameter significantly high to have effects on structure. Considering the first approach, the probability of occurrence of an earthquake can be determined with fault-based PSHA for the nearest fault system to a given area. Considering this, the probability of occurrence of an earthquake which generated a significant value of PGA in a certain moment corresponds to a very small value, and can lead to misunderstand the significance of the index. In the second case, a generic PGA threshold cannot be determinate, since it depends on vulnerability of the structures located in a given area. Due to the fact that the surficial effects of an earthquake are strictly related to the PGA value, we first determine that value considering a fixed return period, with the exceedance of a given value of PGA in a time range. After this, we performed a LSR to obtain the value of PGA considering the stratigraphical and geotechnical characteristics in the area under or close to the bridge (§3.2.1). In this way, we not considered the whole distribution of possible PGA values, but only those derived from the given scenario, and from those we extracted the most reliable value at the foundation level, δ_S.

In this way, $p(s)$ became an observed variable with a fixed value, derived from the selection of a gaussian distribution inside the PDF, and then of most reliable value in the distribution. After this assumption, Eqs 3.32a, 3.32b, 3.32c and 3.32d can be simplified as:

$$P(D_S > d_S) = P(D_S > d_S|\delta_S) \tag{3.33a}$$

$$P\big(D_{LQ} > d_{LQ}\big) = \int_{LQ} \int_{\Delta_{LQ}} P\big(D_{LQ} > d_{LQ}|\Delta_{LQ} = \delta_{LQ}\big) p\big(\delta_{LQ}|LQ = lq\big)\, p(lq|s)\, d\delta_{LQ}\, dlq \tag{3.33b}$$

$$P(D_H > d_H) = \int_{LQ,L} \int_{\Delta_{LQ},\Delta_L} P\big(D_H > d_H|\Delta_{LQ} = \delta_{LS}, \Delta_L = \delta_L\big) p(\delta_{LS}|LQ = ls) p(\delta_L|L = l) p(ls, l|s)\, d(\delta_{LQ}, \delta_L)\, d(ls, l) \tag{3.33c}$$

$$P(D_R > d_R) = \int_R \int_{\Delta_R} P(D_R > d_R|\Delta_R = \delta_R) p(\delta_R|R = r) p(r|s)\, d\delta_R\, dr \tag{3.33d}$$

Even if methods to determine the probability of occurrence of soil liquefaction, landslides and/or rockfall as the probability of exceeding a given threshold value of a GM parameter (e.g., PGA) in a certain time are available in literature (e.g., Zhu et al., 2017, HAZUS, 2024), they are designed for regional studies, considering assumption and simplifications too great to be used at the scale of the infrastructure, as reported in the studies themselves. Furthermore, these studies are calibrated and validated in specific areas, with a peculiar geological framework and geotechnical characteristics, which add a unknown amount of uncertainty to the output values if these method are applied in a different area around the world.

Thus, we considered the occurrence of liquefaction only as the susceptibility of a soil to liquefy in case of the given earthquake, calculating the potential effect at the ground surface using the simplified methods (§3.2.2), and not taking into account the probability of occurrence of liquefaction.

With this simplification, we can obtain the expected value of vertical settlements or horizontal displacements for a defined soil behavior under a given seismic solicitation. Similarly, the occurrence of landslide phenomena in soil or rock is considered only in terms of the area's susceptibility and the expected displacement or impact velocity, without taking into account the probability that the landslide will occur in a given area. Furthermore, considering that the effects of horizontal displacement caused by a translational sliding landslide in soil are entirely comparable to those caused by lateral spreading due to liquefaction, in the event that both phenomena may potentially occur simultaneously, their simultaneous effects on the foundation soil must be considered as the minimal cut-set in Eq. 3.31.

Eqs 3.33a, 3.33b, 3.33c, and 3.33d can be simplified again, obtaining:

$$P(D_S > d_S) = P(D_S > d_S|\delta_S) \quad (3.34a)$$

$$P\left(D_{LQ} > d_{LQ}\right) = P\left(D_{LQ} > d_{LQ}|\delta_{LQ}\right) \quad (3.34b)$$

$$P(D_H > d_H) = P(D_H > d_H|\delta_{LS}, \delta_L) \quad (3.34c)$$

$$P(D_R > d_R) = P(D_R > d_R|\delta_R) \quad (3.34d)$$

From this, the GETI was structured not as a probability of risk, intended as the product of the probability of occurrence of the hazard multiplied by the susceptibility of the area to the hazard and the probability of damage of a given structure, but as an index of the total probability of damage on a certain infrastructure given an earthquake and its correlated secondary hazards. Upon obtaining the values of the peak ground acceleration (δ_S), vertical settlements (δ_{LQ}), horizontal displacements (δ_{LS} and δ_L), rock blocks impact velocity (δ_R), it is possible to assess the potential damage resulting from the interaction of these hazards with the linear structure using fragility curves, achieving the probability of damage derived from ground shaking, liquefaction, landslide, and rockfall.

Thus, GETI is defined by the Eq. 3.31, as the union of the probabilities of damage derived from ground shaking, soil liquefaction, lateral spreading/landslides (considered as a minimal cutset), and rockfall (Eq. 3.35).

$$
\begin{aligned}
GETI = P\left(\bigcup_{i=1}^{n} D_i\right) \\
&= P(D_S > d_S|\delta_S) + P\big(D_{LQ} > d_{LQ}|\delta_{LQ}\big) + P(D_H > d_H|\delta_{LS}, \delta_L) \\
&+ P(D_R > d_R|\delta_R) - P(D_S > d_S|\delta_S)P\big(D_{LQ} > d_{LQ}|\delta_{LQ}\big) \\
&- P(D_S > d_S|\delta_S)P(D_H > d_H|\delta_{LS}, \delta_L) - P(D_S > d_S|\delta_S)P(D_R > d_R|\delta_R) \\
&- \mathrm{P}\big(D_{LQ} > d_{LQ}|\delta_{LQ}\big)P(D_H > d_H|\delta_{LS}, \delta_L) - P\big(D_{LQ} > d_{LQ}|\delta_{LQ}\big)P(D_R > d_R|\delta_R) \\
&- \mathrm{P}(D_H > d_H|\delta_{LS}, \delta_L)P(D_R > d_R|\delta_R) \\
&+ P(D_S > d_S|\delta_S)P\big(D_{LQ} > d_{LQ}|\delta_{LQ}\big)\mathrm{P}(D_H > d_H|\delta_{LS}, \delta_L) \\
&+ P(D_S > d_S|\delta_S)\mathrm{P}(D_H > d_H|\delta_{LS}, \delta_L)P(D_R > d_R|\delta_R) \\
&+ P\big(D_{LQ} > d_{LQ}|\delta_{LQ}\big)\mathrm{P}(D_H > d_H|\delta_{LS}, \delta_L)P(D_R > d_R|\delta_R) \\
&- P(D_S > d_S|\delta_S)P\big(D_{LQ} > d_{LQ}|\delta_{LQ}\big)\mathrm{P}(D_H > d_H|\delta_{LS}, \delta_L)P(D_R > d_R|\delta_R)
\end{aligned}
\tag{3.35}
$$

When liquefaction-induced lateral spread and earthquake-induced landslides occur simultaneously, exerting comparable or overlapping effects on a structure, it is essential to employ a fragility surface, currently unavailable in the literature, to accurately assess the probability of damage from these two hazards. In cases where the phenomena do not have overlapping effects or do not both act on the structure, fragility curves available in the literature for lateral spreading and landslides, respectively, can be used.

From here, it is possible to calculate the GETI for four different damage scenarios: slight, moderate, extensive, and collapse, using the corresponding fragility curves. In this regard, four distinct scenarios are considered, one for each damage level, and the probability of damage is calculated for each individual scenario, always assuming that the events leading to damage act simultaneously on the structure. Although these are evaluations of distinct scenarios, it is clear that the results must be consistent and interconnected, so that, for example, in the case of a high probability of collapse, there is consequently high probability of lesser degrees of damage.

Consequently, the GETI index can be expressed as the total probability of damage potentially derived from the occurrence of ground shaking, soil liquefaction, landslides, and rockfall, calculated for each considered class of damage, as in Equation 3.36a, 3.36b, 3.36c, and 3.36d.

$$GETI_{Slight} = P\big(D_{Slight}|S, LQ, L, R\big) \tag{3.36a}$$

$$GETI_{Moderate} = P(D_{Moderate}|S, LQ, L, R) \tag{3.36b}$$

$$GETI_{Extensive} = P(D_{Extensive}|S, LQ, L, R) \tag{3.36c}$$

$$GETI_{Collapse} = P\left(D_{Collapse}|S, LQ, L, R\right) \tag{3.36d}$$

4. CASE STUDIES

After the theoretical formulation of the GETI index, two case studies were selected to verify its real-world functionality and effectiveness in infrastructure management. The first case study was conducted in the town of Avezzano, municipality of L'Aquila, Italy, and consisted of the seismic risk assessment of the viaduct through the GETI index. The second case study was conducted in the Cherry Hill area, Farmington, Utah (US), where the subsoil of an interchange viaduct upon the Route 89 was reinforced to avoid soil liquefaction in case of the activation of the Wasatch fault, 3 km far from the investigated site. The case study was selected to test the GETI before and after the ground improvement.

4.1. Avezzano (Italy)

To assess the applicability and practical efficacy of the index, GETI was applied to a case study in Italy. The objective of this empirical application is to evaluate whether the proposed procedure can yield the anticipated results, determine its degree of accuracy and precision, and ascertain its potential as a tool for managers to assess the safety of linear infrastructure, such as bridges and road viaducts. The selected viaduct is situated in Abruzzo Region (Central Italy), a region characterized by an active extensional tectonic phase, as evidenced by several significant earthquakes over the past two centuries (Locati et al., 2022). Furthermore, the viaduct is located in proximity to a fault system considered active and capable (Galadini and Galli, 1999; Di Naccio et al., 2020), as well as to the eastern slope of a carbonate relief, which is susceptible to rockfall (Di Naccio et al., 2020), as documented in the Level 1 Seismic Microzonation studies. In addition, the viaduct is constructed upon lacustrine sediments interspersed with material derived from the slope, rendering it potentially susceptible to ground motion amplification and liquefaction.

Given these considerations, the viaduct was selected as a case study for the application of the GETI index. In accordance with the logical framework presented in Fig. 3.2 (§3), the initial step involved the acquisition of the viaduct design and construction documents, geological maps, seismic microzonation studies, and all available geological and geotechnical literature data pertaining to the selected area.

4.1.1. Application of GETI: Level 1

4.1.1.1. Literature Review and Analysis

To assess the probability of damage on the Avezzano viaduct due to the occurrence of an earthquake, an extensive literature review was performed. The aim of this first step was to define the geological and geotechnical asset of the area, the presence of known phenomena linked to the investigated hazard, such as historical landslides or soil liquefaction. From this point of view, we collected data from seismic microzonation studies, from the surveys conducted by the Italian *Azienda* *nazionale autonoma delle strade*, ANAS, and from the academic studies conducted before and during the construction of the Avezzano-Sora highway. The reconstruction of the bridge layout and its associated hazards was also made possible thanks to the level 0, 1, 2 assessment carried out by the Fabre consortium and made available for this thesis work.

The viaduct was constructed from 1991 to 2001, with a length of 343 m and comprising 10 spans of 35 m each. It features a Gerber truss configuration and 9 piles for each track, in addition to abutments. The track partially overlooks a developed area and follows a straight alignment compliant with the main extra-urban road of type B. The road platform consists of two independent tracks, each approximately 7 m wide, accommodating two unidirectional lanes and the right-hand paved quay, without grade intersections, and equipped with a restraint curb on both sides (Fig. 4.1).

Fig. 4.1. Picture of the Avezzano viaduct

The viaduct's structural design incorporates prefabricated prestressed concrete Gerber beams with post-tensioned cables and a continuous slab, decoupled stem batteries cast in situ, and monolithic reinforced concrete abutments. The observed access points to the viaduct are constructed of soil. The piles and abutments of the viaduct are supported by shallow foundations, positioned 3 m below ground level. The foundation soil was reinforced using micropiles extending to a depth of 15 m, considering the stratigraphy deducted from seven boreholes drilled during the initial phase of viaduct construction (Fig. 4.2).

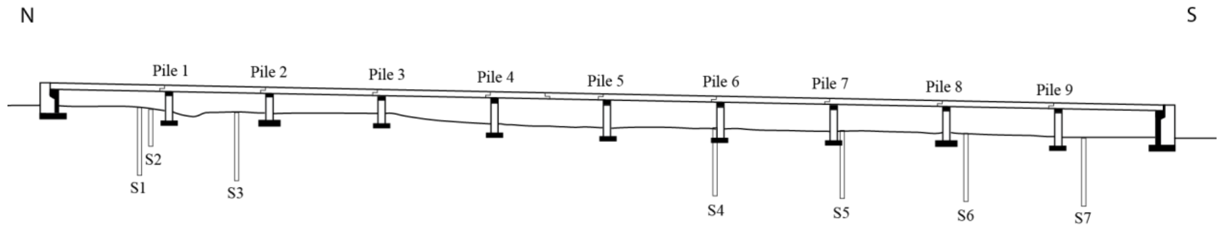

Fig. 4.2: schematic longitudinal section view of the boreholes drilled under the viaduct. The stratigraphic logs show coarse material mixed with lacustrine fine sediments in the first 12-13 m, overlaying lacustrine deposits.

The viaduct is situated close to the town of Avezzano in Central Italy, within a Quaternary intermontane extensional basin known as the Fucino Basin. The basin area was probably covered by a lake since its formation, and it is filled by over 1000 meters of lacustrine and fluvial Plio–Quaternary deposits (Galadini et al., 1999). Following the lake level fluctuation during the last 30,000 years, it is possible to recognize four different lake bed sediments, dated from 1860 a.C. to 32,520 a BP. Close to the mountain range, the stratigraphy shows an alternance of lacustrine and slope/colluvial sediments, given by the oscillations in lake level and the changing of the shoreline. The most surficial lacustrine deposit is dated from 1450 to 930 a B.P., and it is composed of whitish sandy silt, overlain by grey-brown silt layer. This recent deposits overlying the whitish or yellowish fine sands dated from 6170 to 4070 a B.P.. The thicker and oldest deposits sampled in the area occupied by the Fucino lake are mostly formed by greyish-blue clayey silt, intercalated with levels of tephra. They were dated up to 30,000 a B.P..

According to Galadini et al. (1999), the tectonic development of the Fucino Basin (Fig. 4.3) started in the Pliocene, when NE–SW faults along the northern edge created a half-graben basin. However, since the Late Pliocene, activity began on NW–SE trending fault branches along the basin's eastern edge, forming a new half-graben that overlapped and was perpendicular to the existing one. The basin is also affected by secondary faults, with the most notable being the Trasacco and Luco dei Marsi faults.

On January 13, 1915, a powerful earthquake (Ms 7.0) struck the villages in the Fucino Basin and surrounding regions, causing over 30,000 fatalities and widespread damage across an area of 500 km². According to the Italian seismic catalogues (CPTI, 2022), the main shock's epicenter was located in the center of the plain (Fig. 4.3), with the hypocenter at a depth of 8 km. Surface ruptures and other geological effects caused by the earthquake were reported, including landslides in the southeastern part of the basin, differential settlements in the inner portion, and liquefactions along the eastern border of the basin (Galli and Ferreli, 1995). Paleoseismological investigations of the active fault system in the Fucino basin have revealed the occurrence of at least 10 paleoearthquakes in the past 33 ky, with a recurrence interval ranging from 1400 to 2600 years (Di Naccio et al., 2020; Galadini and Galli, 1999). The viaduct is located about 2.5 km far from the Luco dei Marsi active fault, in an area subjected to a macroseismic intensity of 11 (on a scale of 12) during the 1915 earthquake

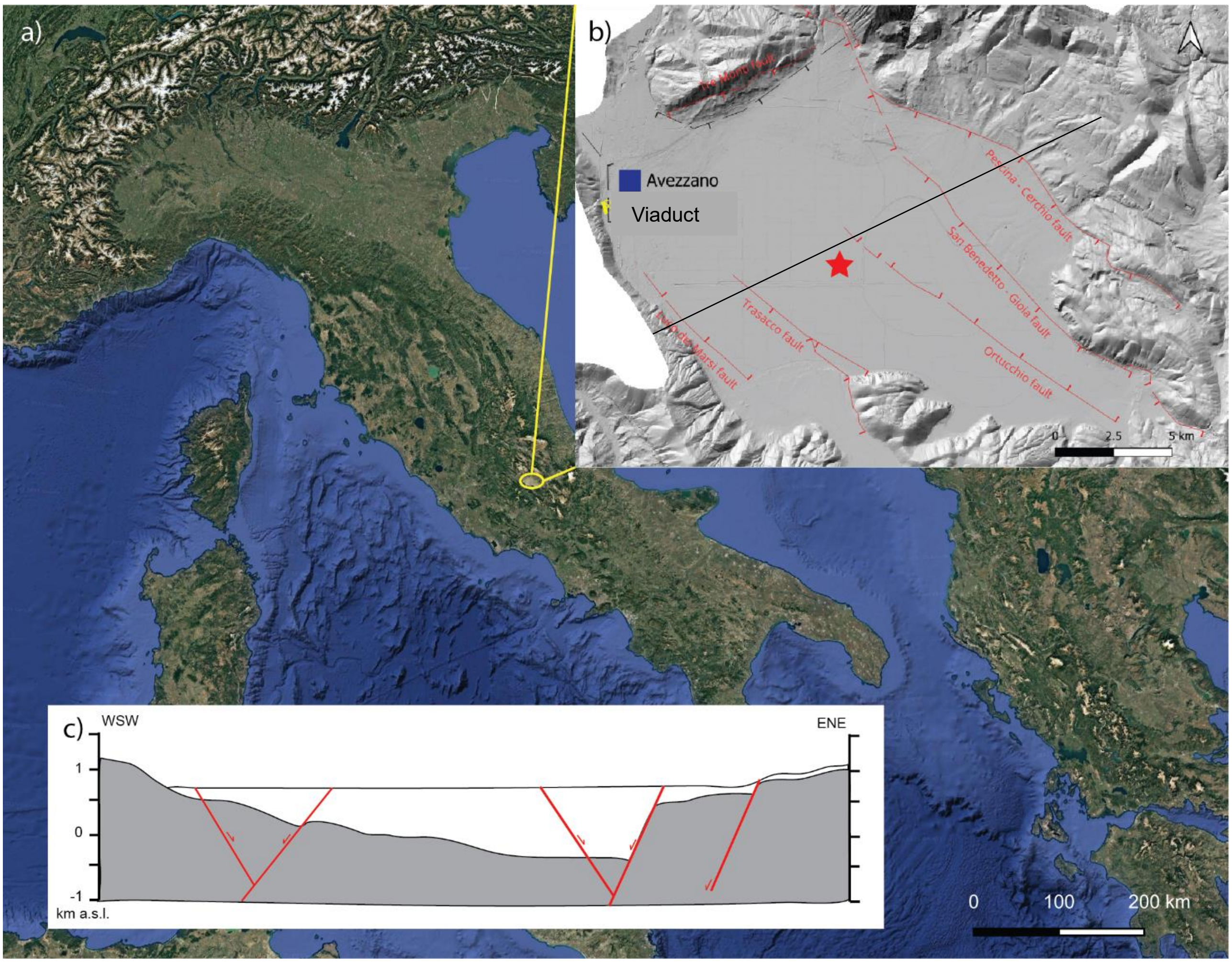

Fig. 4.3. a) Location of the viaduct in satellite view (Google satellite); the yellow square depicts the position of the viaduct; b) schematic tectonic map of the Fucino Basin (DTM 1 m from http://wms.pcn.minambiente.it/ogc?map=/ms_ogc/WMS_v1.3/servizi-LiDAR/LIDAR_ABRUZZO.map); the yellow line depicts the location of the viaduct; the red lines represents the surficial trace of the active normal faults, with the direction of immersion of the fault planes; the black dashed lines represents the supposed trace of buried normal faults (Pliocene); the red star is the supposed epicenter of the 1915 Fucino earthquake; the blue square represent the macroseismic intensity of 11 caused by the Ms 7.0 earthquake of 1915; c) schematic cross section of the central part of the Fucino basin; grey represents the bedrock; white depicts the lacustrine/alluvial deposits; red lines are the active normal faults, as reported in b). Modified from Di Naccio et al. (2020).

The basin is bordered by mountains consisting of deeply fractured Meso-Cenozoic carbonates. The viaduct is located in proximity to the eastern slope of Mt. Salviano (Fig. 4.4).

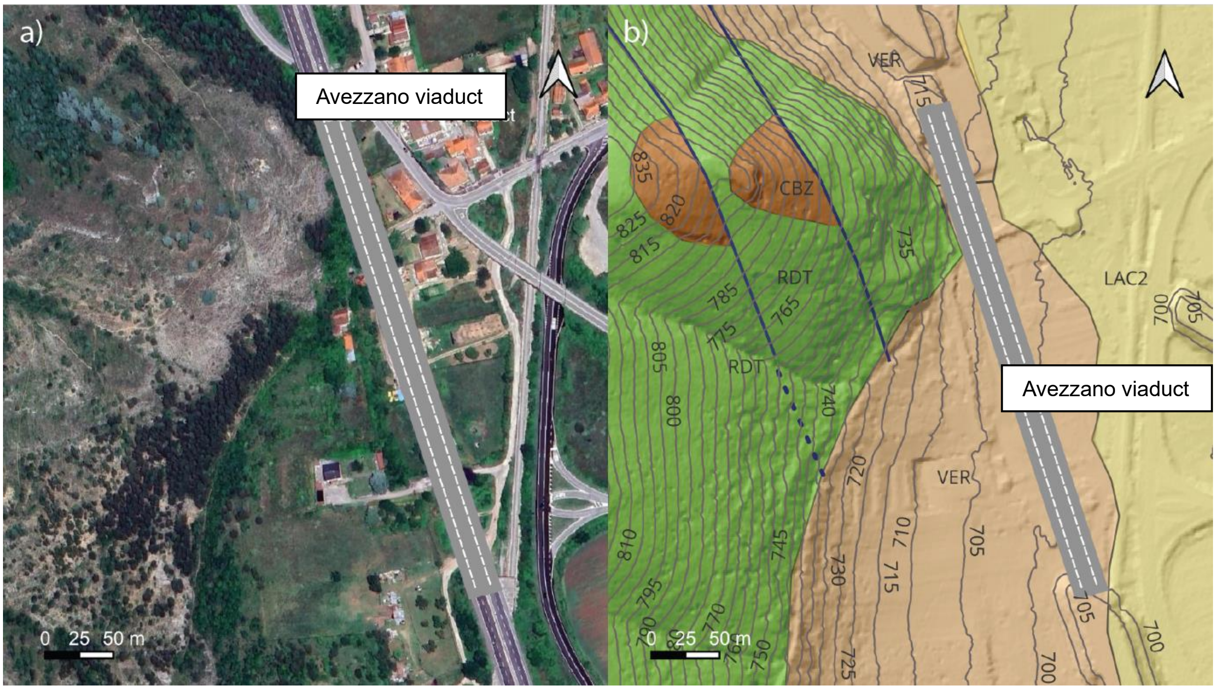

Fig. 4.4. a) Satellite view of the viaduct and the eastern slope of Mt. Salviano; b) schematic geological map of the area investigated; RTD stands for Calcari a radiolitidi (Cretaceous carbonates); CBZ stands for Calcari a briozoi e litotamni (Miocene carbonates); VER stands for slope deposits; LAC2 stands for late Pleistocene lacustrine deposits. Modified from https://www.isprambiente.gov.it/Media/carg/368_AVEZZANO/Foglio.html with the information collected from microzonation studies.

The southernmost region of the eastern slope of Mt. Salviano has experienced rockfall events in the past, as documented in seismic microzonation studies and reported by Di Naccio et al. (2020). Based on this evidence, we examined the slope's morphology near the viaduct using a 1 m resolution DTM derived from LiDAR data (http://wms.pcn.minambiente.it/ogc?map=/ms_ogc/WMS_v1.3/servizi-LiDAR/LIDAR_ABRUZZO.map), suggesting the presence of at least one distinct detach niche along the slope (Fig. 4.5). Furthermore, the stratigraphic logs derived from seven boreholes drilled by ANAS during the construction of the viaduct show the presence of very course material among the alternance of slope and lacustrine deposits along the trace of topographic section 01 (Fig. 4.6), which can be interpreted as derived from the detachment of rock blocks from the slope (rockfall).

To verify and better constrain the evidence collected from literature, a geological survey was conducted in the area of the viaduct.

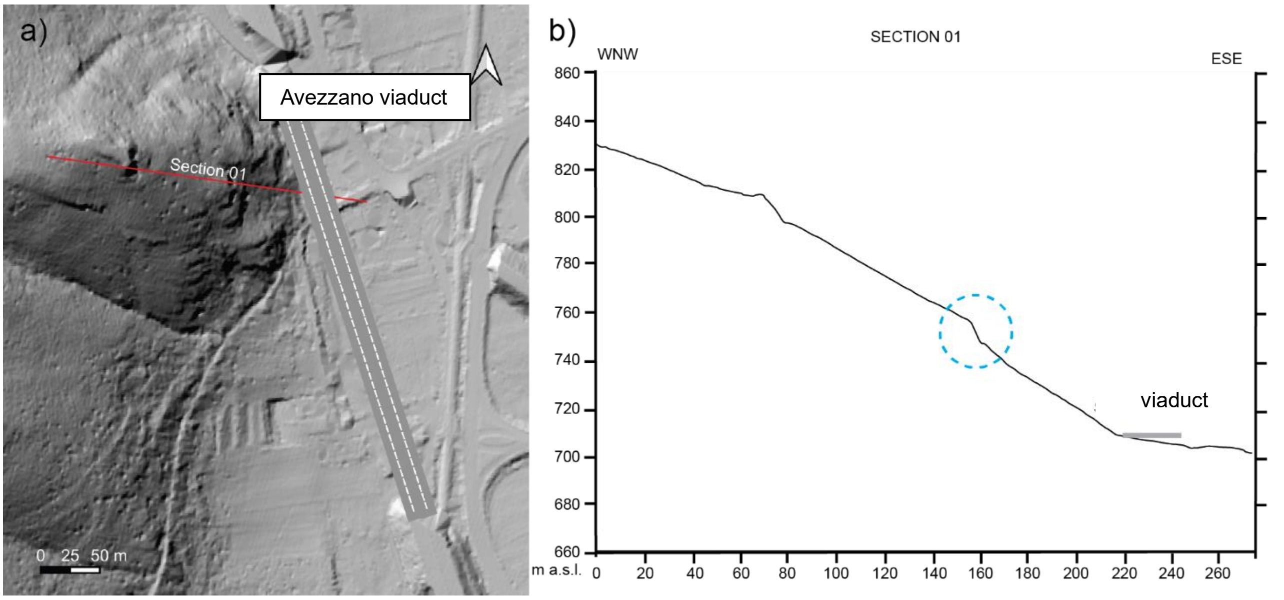

Fig. 4.5. a) Trace of the topographic section of the closest part of the eastern slope of Mt. Salviano to the viaduct; b) Topographic section 01; the dashed blue circle highlights the supposed detach niche; the grey line depicts the viaduct.

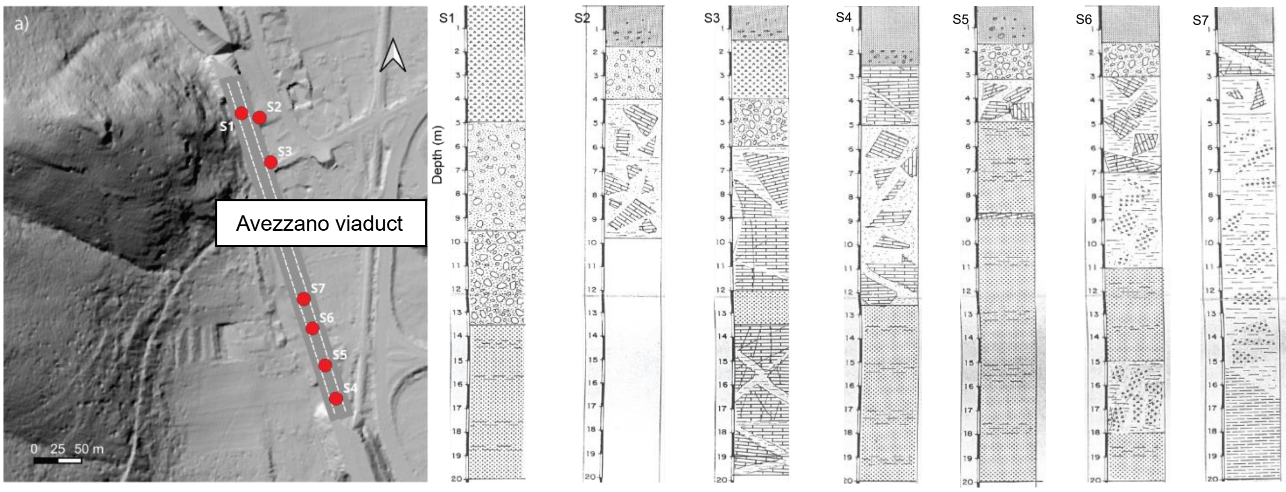

Fig. 4.6. a) position of the seven boreholes (red dots) drilled by ANAS during the construction of the viaduct; b) stratigraphic log of soundings S1, S2, and S3; points represent fine deposits, mostly silty sand; white circles represent the presence of gravel in fine deposits; the bricks represent rock fragments.

4.1.1.2. Geological and Geophysical Surveys

To gain a deeper understanding of the literature review findings and evaluate the extent of slope fracturing, a rapid on-site analysis was conducted (Fig. 4.7). This analysis aimed to assess the degree of fracturing and the current condition of both the slope and the land supporting the viaduct. The analysis confirmed the existence and characteristics of the fracture families identified during level 3 seismic microzonation studies in the municipality of Avezzano, as reported by Di Naccio et al. (2020).

Fig. 4.7. Photograph of the surveyed area on the slope near the viaduct; as can be seen, the rock is heavily fractured and sparsely vegetated.

As reported by Di Naccio et al. (2020), the eastern slope of Mt Salviano is affected by three major sets of fractures, as shown in Figure 4.8 b and c:

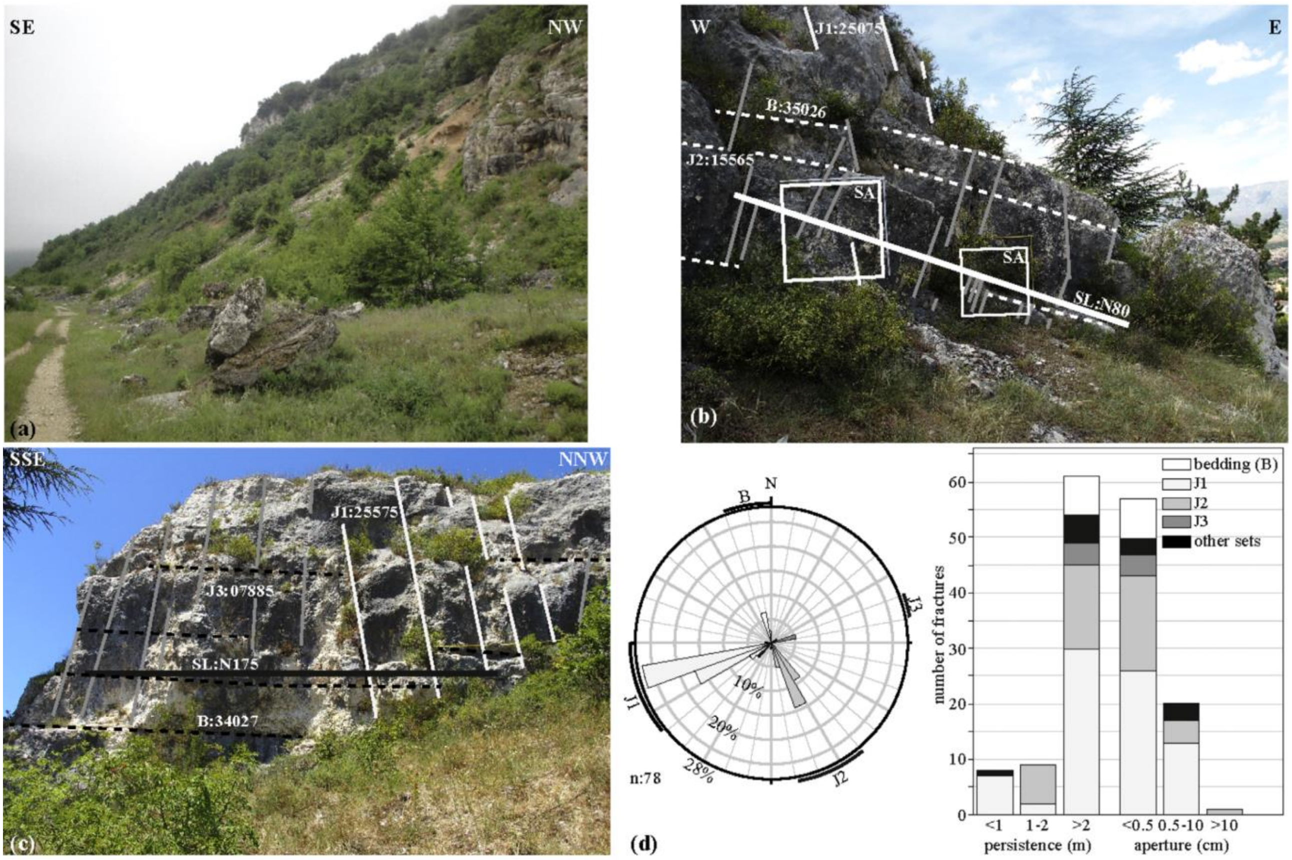

Fig. 4.8: a) rock fall block found at the piedmont of Mt. Salviano eastern slope, ~1.2 km far from the studied area; b) and c) geomechanical analyses. J1, J2 and J3 represent the sets of fractures with their orientation, B

stands for bedding; d) synoptic rose diagram and persistence and aperture frequency diagrams of the main joint sets and bedding (from Di Naccio et al., 2020).

Di Naccio et al. (2020) suggest that, given the slope near the viaduct is approximately 35° steep and shares similar geomechanical characteristics with the southern area examined during the third level of microzonation studies, it can be inferred that the slope is prone to earthquake-induced instability. The primary failure mode is likely to be topple/rockfall..

4.1.1.3. Applicability of the Index

Considering the first part of the logic flow of GETI index (§3), the question to address is "Is the area affected by the hazard investigated?". Based on data acquired from literature and geological surveys, it is possible to conclude that the viaduct is exposed to seismic hazard, due to the presence of an active fault system in the near field. The proximity of the structure to the mountain slope and the structural features of the rock mass make the viaduct potentially susceptible to rockfall hazard, while the presence of an approximately 40 m thick lacustrine deposit beneath the foundation may induce ground motion amplification phenomena (§3.1.2.2).

It appears feasible to exclude the occurrence of soil liquefaction due to the absence of a water table in the first 20 m below the ground surface, remembering that soil saturation is a necessary, but not sufficient, condition for the occurrence of earthquake-induced liquefaction (§3.1.2.3). Furthermore, the stratigraphic logs indicate the presence of approximately 10 m of very coarse slope material, which is typically not susceptible to liquefaction. Consequently, comprehensive studies are necessary for risk assessment and to accurately apply the GETI index.

4.1.2. Application of GETI: Level 2

4.1.2.1. Site Response Analysis

To analyze the potential for ground motion amplification and quantify the Peak Ground Acceleration (PGA) value in correspondence of the foundation soil deposit of the viaduct, a site response analysis was conducted using the 1D nonlinear time domain DEEPSOIL code version 7.1 (DEEPSOIL V7.1, 2024). Given the relevance of the viaduct, a design reference period of 75 years was assumed, and consequently, a 712-year return period scenario was selected, based on the Italian seismic code (NTC, 2018) for Ultimate Limit State (SLV). Utilizing the probabilistic assessment of seismic hazard (PSHA) of Italy from INGV studies (Stucchi et al., 2011) and implemented in NTC2018, an a_g value of 0.28 g can be assumed as the acceleration input at the seismic bedrock.

Seven natural accelerograms were selected in accordance with the seismological characteristics (expected magnitude and source-to-site distance of the regional fault systems), and scaled to the considered a_g value. Subsequently, the seismic input was applied at the seismic bedrock (characterized by $V_S = 1200$ m/s) located at 40 m depth as deduced from data from previous studies.

Above the bedrock, the stratigraphy of the area beneath the viaduct is variable and affected by coarse and chaotic material, likely derived from rockfall and/or erosion in the first 12 m below ground level. The ground motion amplification effects were modeled through site response analyses based on seven stratigraphic logs available from previous studies, and considered representative of geological and geotechnical conditions along the viaduct.

In this regard, and considering the position of the piles in relation to the slope, the stratigraphy of boreholes S4-S5-S6-S7, corresponding to piles from 6 to 9, and to the southern abutment, was extended to piles from 3 to 5. The stratigraphy of boreholes S1-S2-S3 were considered for the abutment in the northern part of the structure, as well as for the first two piles (Fig. 4.2). The Vs profiles of the models adopted in the analyses are shown in Figure 4.9 a. The effect of micropile improvement in the upper 15 m of subsoil was not considered in the analysis. As a result, seven PGA profiles were obtained (Fig. 4.9 c).

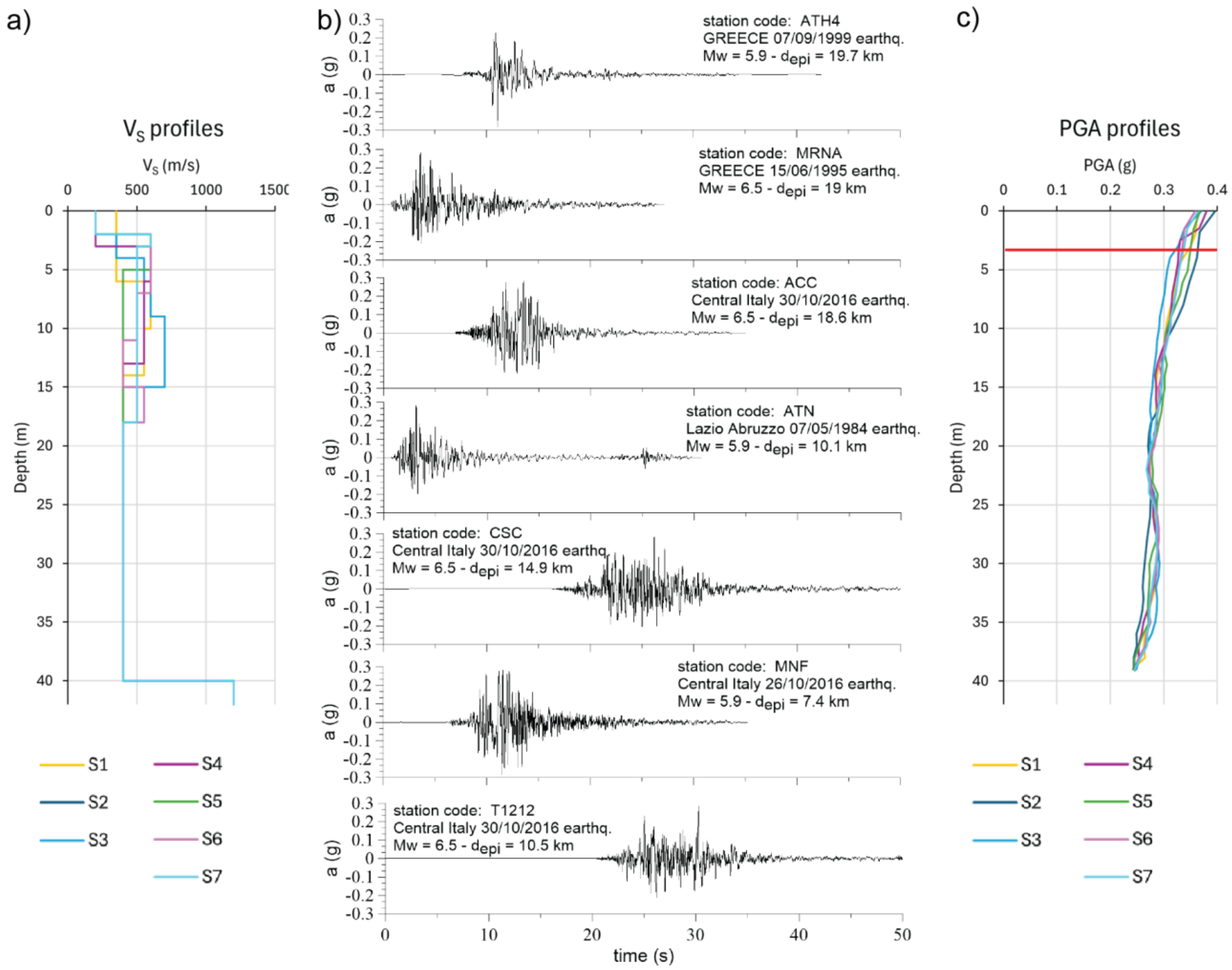

Fig. 4.9. a) V_S profiles deducted from microzonation studies and adopted for site response analyses; b) Natural accelerograms employed for site response analyses with main characteristics; d_{epi} is the epicentral distance;

SF is the scaling factor; M_W is the moment magnitude; c) PGA profiles, considering boreholes S1, S2, S3, S4, S5, S6, and S7, obtained through the site response analysis using Deepsoil code version 7.1 (DEEPSOIL V7.1, 2024). The red line represents the foundations level.

To determine the behavior of the structure under the action of the earthquake, an average value of PGA was calculated using the seven profiles, obtaining a PGA value at the foundations level (3 m below the ground surface) of 0.34 g. Although the studied area is situated in an intramountain basin, which could potentially lead to 2D basin edge effects, we opted for a 1D analysis. This decision was made to maintain the index as a straightforward tool for risk assessment, avoiding overly advanced techniques.

4.1.2.2. Slope Stability Analysis

Previous studies (Di Naccio et al., 2020) conducted on the slope in question revealed strata dipping in the slope direction and that the rock mass is also affected by several families of persistent fractures perpendicular to the stratum boundaries. Analyses based on the limit equilibrium method (pseudo-static approach) conducted on the same slope indicate a minimum threshold of 0.09 g for block slip (D'Elia, 1989). Considering that peak accelerations reach values about 3 times higher than the threshold, the detachment of blocks from the slope in the event of an earthquake is considered highly probable.

To quantify the probability of the interaction of the rockfall with the structure and to determine the impact velocity, a numerical model was created using Rockfall2D code by Rocscience Inc.. As input data, nine profiles derived from a Digital Terrain Model (DTM) with 1 m resolution (http://wms.pcn.minambiente.it) were traced in correspondence of six piles and the two abutments of the viaduct, considering the maximum slope value for each. The 9 two-dimensional models of the slope were utilized to model the occurrence of rockfall, considering as seeders the scarps or the discontinuities of the slope shape. The model used is that of the rigid body (§3.2.4), with spherical blocks of three different sizes: 1.2, 1.5, and 1.8 m. The choice of dimensions was made by taking into account both the data collected during level 1, from the literature and from field surveys, and in order to make the model comparable with that used for the development of impact fragility curves by Xie et al. (2020). A horizontal detachment velocity of 22 cm/s was imposed on the blocks, calculated by considering the PGA at the bedrock from the seven natural accelerograms used for the site response analyses. The slope was modeled considering both the absence of vegetation (Fig. 4.7) and the absence of barriers. For each source area, trajectories and velocities were modeled for 100 blocks for each size considered, ultimately obtaining a statistically representative velocity value and a percentage of blocks impacting the structure. In this sense, the position of the individual pile in each profile was estimated from DTM, satellite, and survey data, and the velocity of the impact of the rocks on the pile was calculated considering the estimated velocity of the blocks when they reach this position on the profile (Fig. 4.10).

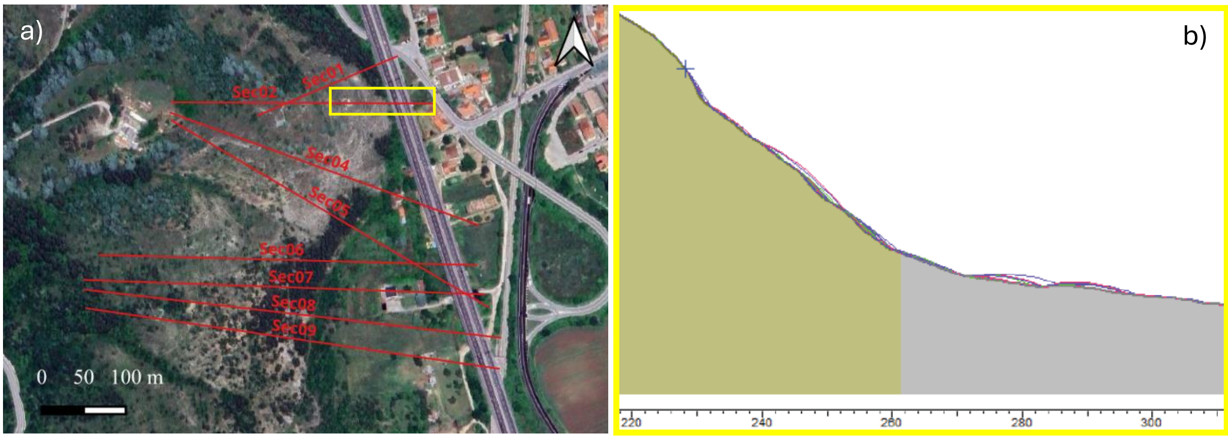

Fig. 4.10. a) Satellite (Google Earth) view of the slope near the viaduct; red lines depict the section traces, the yellow box indicates the slope profile reported in b). b) Slope profile with detachment points (crosses) and trajectories (red and blue lines) of falling blocks, as simulated using the Rockfall2D code.

As a result, the 100% of the rocks impacted on pile 1 west and 25% is able to impact pile 1 east , with an average velocity of approximately 17 m/s. Pile 2 west was impacted by 10% of the blocks with an average velocity of 15 m/s, while piles from 3 to 9 were not impacted by rocks in this simulation.

4.1.2.3. Damage Assessment

The results from site response and rockfall analyses are used as input parameters in the fragility curves developed by Brandenberg et al. (2011) and Xie et al. (2020) for consequence of seismic ground shaking and rock impact velocity, respectively (Fig. 4.11).

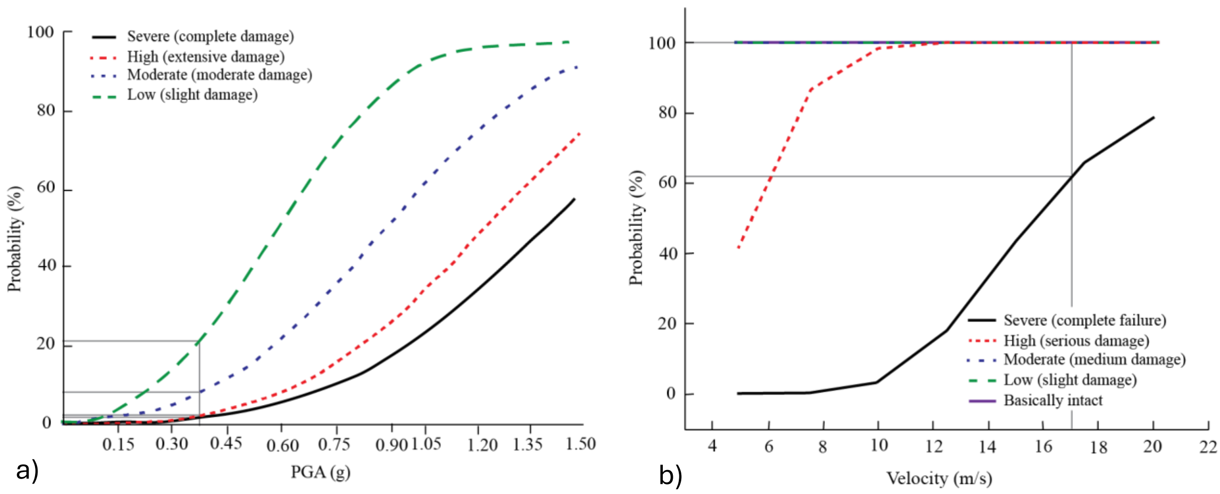

Fig. 4.11. Fragility curves for damage on bridges derived from a) ground shaking (modified from Branderberg et al., 2011) and b) rockfall (modified from Xie et al., 2020). Grey lines represent PGA and block impact velocity resulting from the analyses conducted in this study.

Regarding the fragility curves proposed by Branderberg et al. (2011), those for bridges type E5 (Seat Abutment & Continuous with expansion joint and pier isolation), corresponding to the bridge under study, were used to determine the probability of damage for the selected viaduct. As for rockfall, the curves developed by Xie et al. (2020) refer exclusively to two pile models: one with a circular section and one with a square section. It is clear that neither model corresponds to the construction design of the viaduct addressed in this study, which features rectangular piles (Fig. 4.1) with dimensions of 2.4 x 7.60 m. Since the expected impact will mainly occur on the shorter side, which faces the slope, it is considered entirely implausible that the effect would be comparable to that on a pile with a side length of 1.06 m, like those used in the tests conducted by Xie et al. (2020). Nevertheless, since the aim of this case study is to test the functionality of the GETI and no more suitable curves are available, it was decided to proceed with the evaluation all the same, bearing in mind that the result does not reflect the actual potential damage to the bridge, which is presumably largely overestimated.

4.1.3. Results

The results in terms of damage probability for the three seismic phenomena (shaking, liquefaction and rockfall) are shown in table 1. If liquefaction is obviously zero as stated in level 1 assessment, the most important contribution to damage is related to rockfall for all damage classes while the ground shaking (even considering the amplification effects) plays a less relevant role. Interventions strategies for seismic risk mitigation of the viaduct should therefore focus on rockfall, i.e. the protection of the viaduct from block impact (rockfall barriers) or consolidation of the slope to prevent the detachment of rock blocks.

Table 1: Probability of damage derived from fragility curves for slight, moderate, extensive, and collapse damage referred to, respectively, ground shaking, soil liquefaction, landslides/lateral spreading, and rockfall. The values of the expected damage due to rockfall are largely overestimated and do not represent the actual damage on the structure in case of an earthquake.

	$P(D_S)$	$P(D_{LQ})$	$P(D_H)$	$P(D_R)$
Slight	0.22	0	0	0.25
Moderate	0.08	0	0	0.25
Extensive	0.04	0	0	0.25
Collapse	0.03	0	0	0.16

In addition, it is essential to emphasize that the viaduct comprises two semi-independent tracks with common abutments; each track has nine piles. In this context, the state of collapse is defined as the loss of functionality of both tracks due to the rupture of the two piles during the rockfall. As the viaduct presents an isostatic scheme, the impact of rocks on one pile is considered sufficient to cause damage to the structure; consequently, the higher velocity together with the higher percentage of impacting blocks were used as parameters in damage determination. Thus, considering that the

100% of rocks impact on pile 1 west, but only the 25% of the blocks impact pile 1 east, potentially causing the collapse of the entire structure, the resulting probability of damage is defined as the product of the probability of damage due to the rocks' impact and the probability of impact as the percentage of rock blocks that reach the eastern pile.

Following the determination of probabilities for slight, moderate, extensive, and collapse damage, the GETI was calculated using Eqs 3.36a, 3.36b, 3.36c, and 3.36d (§3.3). Subsequently, the GETI was derived as follows:

$$\boldsymbol{GETI_S} = 0.22 + 0 + 0 + 0.25 - 0.22 * 0 - 0.22 * 0 - 0.22 * 0.25 - 0 * 0 - 0 * 0.25 - 0 * 0.25 + 0.22 * 0 * 0 + 0.22 * 0 * 0.25 + 0 * 0 * 0.25 - 0.22 * 0 * 0 * 0.25 = 0.415 = \mathbf{41}\%$$

$$\boldsymbol{GETI_M} = 0.08 + 0 + 0 + 0.25 - 0.08 * 0 - 0.08 * 0 - 0.08 * 0.25 - 0 * 0 - 0 * 0.25 - 0 * 0.25 + 0.08 * 0 * 0 + 0.08 * 0 * 0.25 + 0 * 0 * 0.25 - 0.08 * 0 * 0 * 0.25 = 0.31 = \mathbf{31}\%$$

$$\boldsymbol{GETI_E} = 0.04 + 0 + 0 + 0.25 - 0.04 * 0 - 0.04 * 0 - 0.04 * 0.25 - 0 * 0 - 0 * 0.25 - 0 * 0.25 + 0.04 * 0 * 0 + 0.04 * 0 * 0.25 + 0 * 0 * 0.25 - 0.04 * 0 * 0 * 0.25 = 0.28 = \mathbf{28}\%$$

$$\boldsymbol{GETI_C} = 0.03 + 0 + 0 + 0.15 - 0.03 * 0 - 0.03 * 0 - 0.03 * 0.15 - 0 * 0 - 0 * 0.15 - 0 * 0.15 + 0.03 * 0 * 0 + 0.03 * 0 * 0.16 + 0 * 0 * 0.16 - 0.03 * 0 * 0 * 0.16 = 0.185 = \mathbf{18}\%$$

The results are synthetized in Table 2. The values of the expected damage due to rockfall are largely overestimated and do not represent the actual damage on the structure in case of an earthquake.

Table 2. Results after computing GETI for each class of damage

	$P(\mathrm{D})$ %
$GETI_S$	41
$GETI_M$	31
$GETI_E$	28
$GETI_C$	18

4.2. Cherry Hill Interchange (Farmington, Utah, US)

To assess the applicability and practical efficacy of the index, GETI was applied to a case study in Utah (US). The objective of this application is to evaluate whether the proposed procedure can yield the anticipated results, determine its degree of accuracy and precision, and ascertain its potential as a tool for managers to assess the safety of linear infrastructure, such as bridges and road viaducts, in case the soil under the bridge was improved after liquefaction and lateral spreading assessment conducted considering the design earthquake.

Situated at the junction of U.S. Highway 89 and State Road 273, the Cherry Hill Interchange is approximately 29 kilometers north of Salt Lake City, within the Farmington area, and less than 2 kilometers from the surface trace of the active Wasatch Fault. The viaduct is constructed on deposits from Lake Bonneville and alluvial materials. Additionally, the Cherry Hill Interchange is located in a region known for liquefaction-induced lateral spreading. In response to these conditions, the soil beneath the viaduct was enhanced in 2000 with the installation of 850 stone columns, targeting a treatment depth of 8 to 15 meters, to mitigate the risks of liquefaction and lateral spreading.

4.2.1. Application of GETI: Level 1

4.2.1.1. Literature Review and Analysis

To assess the probability of damage on the Cherry Hill Interchange due to the occurrence of an earthquake, an extensive literature review was performed. The aim of this first step was to define the geological and geotechnical asset of the area, the presence of known phenomena linked to the investigated hazard, such as historical landslides or soil liquefaction. From this point of view, we collected data from seismic microzonation studies, from the surveys conducted by the United States Department of Transportation (UDOT), and from the academic studies conducted before and during the construction of the U.S. Highway 89 and the Legacy Parkway (State Road 67).

Cherry Hill Interchange is a viaduct that overpass the U.S. Highway 89. It is composed by two abutments and one central pile, which divided the eight lanes of the highway in four per direction. The viaduct has a length of 100 m and comprising 2 spans of 50 m each (Fig. 4.12). The deck is designed as a continuous structure and is made up of 12 prefabricated steel IPE beams, joined together by lattice-type steel crossbeams. The pier is made of reinforced concrete, with a frame of four shafts connected at the height of the cap by arches. The abutments are of the through-type, consisting of a visible bearing platform. Both the pier and abutments are founded on piles. Specifically, the foundation of the west abutment consists of a footing buried 2 m into natural ground, connecting piles 40 m long; the foundation of the east abutment consists of a footing buried 1 m into fill soil, connecting piles 34 m long; the foundation of the pier consists of a footing buried 4 m into natural ground, connecting piles 32 m long.

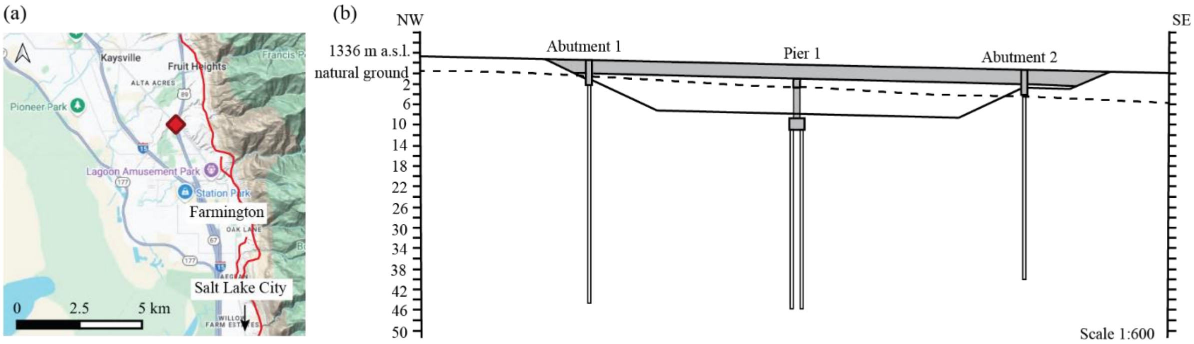

Fig. 4.12. a) Map of the area of Cherry Hill from Google Terrain; the red diamond depicts the position of the viaduct; the red line represents the surficial trace of the Wasatch fault (modified from USGS https://usgs.maps.arcgis.com/apps/webappviewer/index.html?id=5a6038b3a1684561a9b0aadf88412fcf). b) Schematic representation of Cherry Hill Interchange (modified from Price et al., 2000).

The Wasatch fault zone (WFZ), which bordered the Great Salt Lake (GLS) basin on the east, is the master, range-bounding normal fault system in northern Utah. It divides the stable Colorado Plateau and southern Rocky Mountain provinces to the east from the actively extending Basin and Range province to the west (Parsons, 2006). The WFZ accommodates 2–3 mm/yr of nearly east–west extension (Chang et al., 2006) along 10 major structural segments that together span ~350 km. Paleoseismological observations indicate that 24 surface-rupturing earthquakes, thought to be magnitude 6.5 or larger, have occurred in the last 7,000 years on the five central segments of the WFZ (Machette et al., 1991), making the WFZ the largest contributor to seismic hazard in the region (Kleber et al., 2021). Recent studies (e.g., Pang et al., 2020) highlighted the listric behavior of WFZ, with a steep dip plane (~70°) near the surface, and a low angle dipping at depth (~20° at >12 km). This means that the geometry of the basin reach the maximum depth close to the mountain front, with the top of the hanging-wall, composed by pre-tertiary bedrock, at depth estimated to be up to 3 km. Because most of Utah's 3.2 million residents are concentrated in an urban corridor that spans the WFZ and related faults, the regional seismic risk is severe. The highest risk occurs for the Salt Lake City metropolitan area, an urban core of 1.2 million people that lies in a sedimentary basin directly above the west-dipping Wasatch fault (Pang et al., 2020).

The actual Davis and Weber basins were occupied in the late Pleistocene by the Lake Bonneville, fed by Bear, Weber and Provo Rivers until the regression due to the catastrophic failure of the alluvial Old River Bed threshold, which dropped the lake level during the Bonneville flood at ~14.5 ka BP. From this event, the Lake Bonneville faced a continuous regression until dropping under the 1287 m above the sea level during the Holocene. The lake faced abrupt variations in level during the period between ~160 and ~10 ka BP, reaching the maximum of 1550 m above sea level ~20 ka BP. Every variation in the lake level during the last 40 ka is marked by a recognizable shoreline (Hart et al., 2004; Oviatt, 2014). Considering these cycles and the longtime of existence of the Lake Bonneville, the stratigraphy of the deposits that filled the basins is a complex superimposition of alluvial and lacustrine sediments, with an estimated thickness of >200 m, upon the pre-Bonneville sediments (Lemons and Chan, 1999). The latter are mainly composed by glacial and alluvial lower Pleistocene deposits, >200 m thick, overlying Pliocene volcanic tuffs, muds and agglomerates (Hunt et al., 1953).

The area of Cherry Hill is located in the northern part of the Davis basin (Fig. 4.13), mostly covered by the Great Salt Lake and bounded on the east to the Wasatch Mountain Range. According to Lemons and Chan (1999), the area is lapped by the distal part of the Weber river paleo-delta, which is characterized by fine grained deposits.

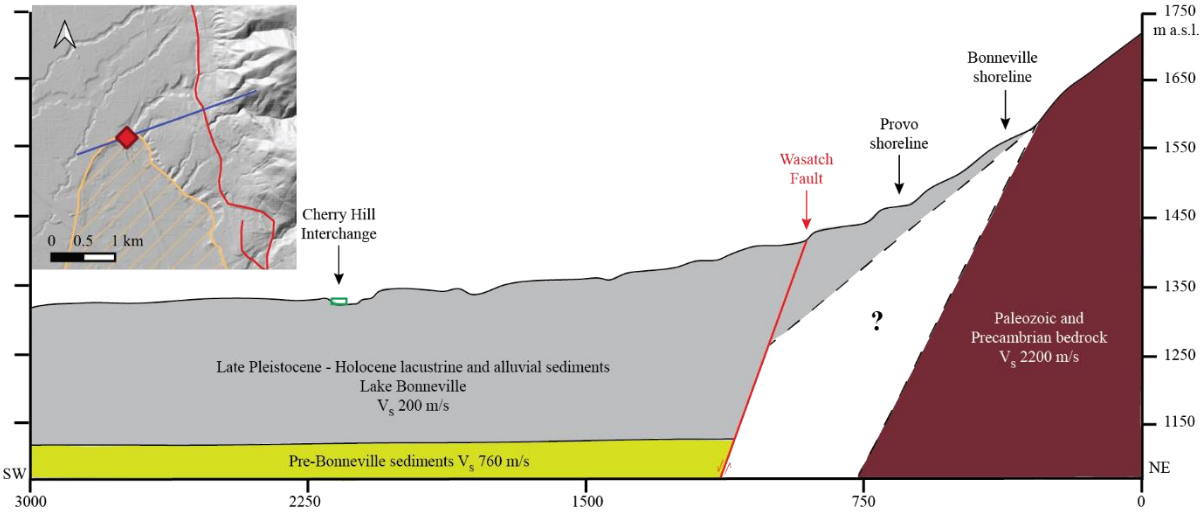

Fig. 4.13. Schematic geological cross section of the area of Cherry Hill. The topographic profile is extracted from the 5 m DTM of Davis County; the map on the left shows the position of the cross section; the yellow lines depict the extension of the lateral spreading deposits (modified from McDonald and Ashland, 2008); the red diamond represent the Cherry Hill Interchange; the blue line represent the trace of the cross section; the red line approximated the surficial trace of the Weber segment of the Wasatch fault (modified from USGS https://usgs.maps.arcgis.com/apps/webappviewer/index.html?id=5a6038b3a1684561a9b0aadf88412fcf). The wedge between the triangular facets and the Bonneville and pre-Bonneville sediments at the footwall of the Wasatch fault was intentionally left blank due to the uncertainties on the amount of the fault displacement.

In turn, the surficial stratigraphy of the northern part of the Davis basin is affected by the lack of major rivers and the presence of a large liquefaction-induced lateral spreading, so that the stratigraphy of this area consists of lacustrine and alluvial silt, clay, and fine sand, with alluvial and lateral-spread deposits, typically overlie lacustrine deposits, with a V_{S30} of about 200 m/s, as reported by McDonald and Ashland (2008). Previous studies in the northern part of Farmington showed that the ground water table (GWT) level always range between 1.5 to 4 m depth, and surficial deposits presents a median fine content of about 53%, even if they showed a non-plastic behavior (Rollins et al., 2012).

4.2.1.2. Applicability of the Index

Considering the first part of the logic flow of GETI index (§3), the question to address is "Is the area affected by the hazard investigated?”. Based on data from the literature and Level 1 analyses, it can be stated that the structure is located in an area susceptible to earthquakes, due to the presence of an active fault system, which is also very close to the viaduct itself when considering the surface trace of the Wasatch fault. The stratigraphy, represented by approximately 200 m of recent lacustrine-alluvial sediments overlying older lacustrine-alluvial deposits, makes the area potentially susceptible to phenomena of seismic motion amplification. Furthermore, the morphological characteristics of the site, which presents a slight slope toward the west, make it potentially susceptible to phenomena of liquefaction-induced lateral spread. The fact that the liquefiable layers were reinforced with gravel columns after the construction of the viaduct makes the case study particularly interesting, as it allows for comparison of the GETI values obtained through Level 2 analysis before and after the treatment, and for assessment of their sensitivity and functionality. The occurrence of liquefaction phenomena that could interfere with the structure through vertical settlements was not considered due to the presence of deep foundations that rest on non-liquefiable soils at depths greater than 30 m below the surface. The distance from the rock slope, which is over one kilometer, reasonably excludes the possibility that the structure could be affected by seismically induced rockfall events. The absence of covers other than those already considered in previous evaluations excludes the possible occurrence of landslide phenomena concurrent with those due to liquefaction. Therefore, Level 2 analyses will proceed with respect to site response analysis and liquefaction-induced lateral spread.

4.2.2. Application of GETI: Level 2 Before and After Ground Improvement

4.2.2.1. Site Response Analysis

Given the potential earthquake-related hazards in the area, we conducted a numerical site seismic response analysis and a liquefaction/lateral spreading assessment using simplified methods, as outlined in level 2 of the GETI (Salvatore et al., 2025). It is noteworthy that the subsoil at the Cherry Hill Interchange was reinforced by installing 850 stone columns at depths ranging from 8 to 15 meters (Rollins et al., 2012). Consequently, the liquefaction and lateral spreading assessments were performed considering the soil resistance both before and after this treatment. However, due to the lack of available VS profile data following the subsoil reinforcement, updating the PGA from the site response analysis was not feasible. As a result, the liquefaction assessment post-treatment was conducted using the same seismic input PGA as before.

To analyze the potential for ground motion amplification and quantify the PGA value corresponding to the foundation depth of the viaduct, a site response analysis was conducted using the 1D nonlinear time domain DEEPSOIL code version 7.1 (DEEPSOIL V7.1, 2024). According to the 2018 National Seismic Hazard Model for the conterminous United States, a PGA value of 0.6 g at seismic bedrock was estimated considering a 2% probability of exceedance in 50 years and a National Earthquake

Hazards Reduction Program (NEHRP) site class B/C ($V_{S30} = 760$ m/s). Four natural accelerograms (Fig.4.13b) were selected in accordance with the seismological characteristics (expected magnitude and source-to-site distance of the extensional regional fault systems), and scaled to the input PGA value of 0.6 g by ensuring a scaling factor lower than 4 (Pagliaroli and Lanzo, 2008). Subsequently, the seismic input was applied at the seismic bedrock (characterized by $V_S = 760$ m/s) located at a depth of 200 m as deduced from data from previous studies acquired in Level 1.

Above the bedrock, the stratigraphy beneath the viaduct primarily consists of silty sand and sandy silt, with clay being predominant in the first 2 meters from the surface (Price et al., 2000). There are also intercalations of coarse material resulting from the alternating transgression and regression of Lake Bonneville, leading to the deposition of fluvial deposits, such as the Weber delta.

Ground motion amplification effects were modeled through a total stress site response analyses based on three stratigraphic logs, which are considered representative of the geological and geotechnical conditions along the viaduct. The V_S profiles used in the analyses, shown in Figure 4.14 a, correspond to the power function that best approximates the measured values, extending the V_S profile up to a depth of 200 meters. The analysis did not consider the improvement in the upper 15 meters of subsoil. The hyperbolic MKZ model with non-Masing rules was employed in the modeling, while the nonlinear soil behavior was characterized using Darendeli (2001) normalized shear modulus and damping curves for a plasticity index PI=0. The results, in terms of PGA profiles, are presented in Figure 4.14 c, indicating a deamplification due to the high level of nonlinearity experienced by the soft soils under severe seismic input. An estimated PGA value of 0.2 g at the top can be derived from the average PGA profile (dashed red curve in Fig. 4.14 c).

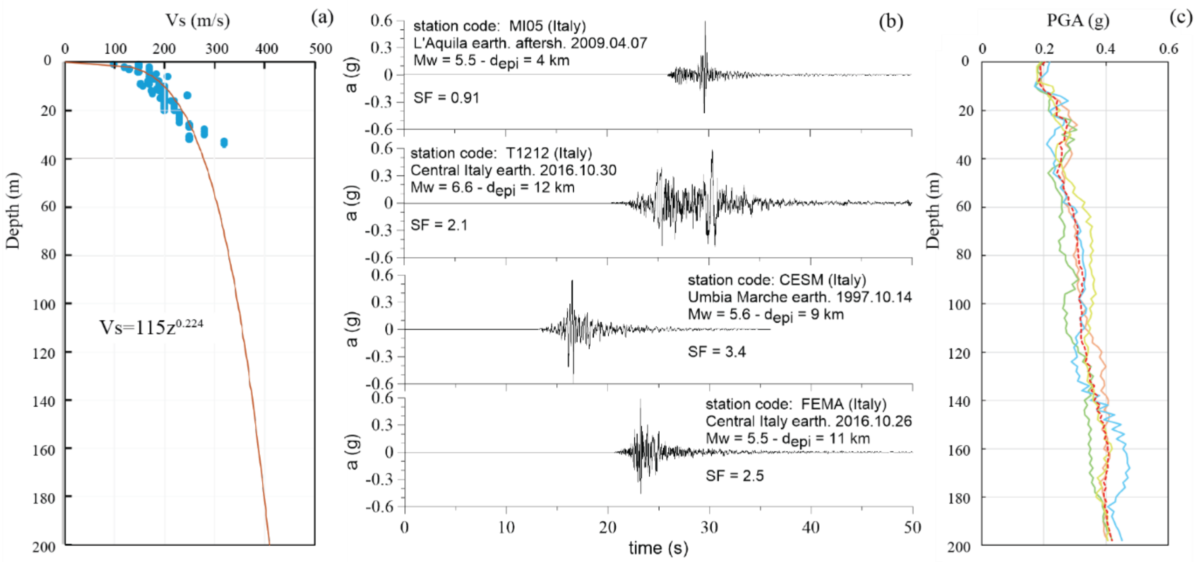

Fig. 4.14. a) Shear wave velocity profile assumed in site response analysis; blue points represent measured values; orange line represents the power function to extend the V_S values at depth. b) Natural accelerograms employed for site response analyses with main characteristics; d$_{epi}$ is the epicentral distance; SF is the scaling

factor; M_W is the moment magnitude c) Results in terms of PGA profile for each input motion applied and as average values (red dashed line).

4.2.2.2. Soil Liquefaction Assessment

Given the seismic input parameters, the liquefaction resistance of the sand site of the Cherry Hill Interchange was evaluated using both Cone Penetration Test (CPT) and Standard Penetration Test (SPT) blow count conducted close to abutment n. 2 and reported by Price et al. (2000). The comparison of the two tests made it possible to assess the liquefaction potential and to evaluate the expected lateral displacement value up to 20 m depth.

As suggested by Idriss and Boulanger (2008), the CPT and SPT blow count (q_c and N_{SPT} respectively) were first corrected considering an overburden correction factor, and then modified to the equivalent value for clean sand (fine content ≤5%), obtaining the $(q_{c1N})_{cs}$ and $(N_1)_{60cs}$ respectively. The Cyclic Stress Ratio (CSR) induced by the earthquake can be calculated as originally proposed by Seed and Idriss (1971), considering a PGA of 0.2 g, and the depth reduction factor as defined in Idriss et al. (1999). To make the data comparable regardless of the earthquake, M_W is standardized to the value of 7.5 using the MSF given by Idriss and Boulanger (2008) and a design magnitude of 7.4 (Rollins et al., 2012). The GWT was considered at 4 m depth, using an average value of measured GWT level in the area. The CRR and the FS were calculated as proposed by Idriss and Boulanger (2008) for both CPT and SPT, while the LPI is calculated as in Iwasaki (1978). The results are shown in Figure 4.15 b, c, and d.

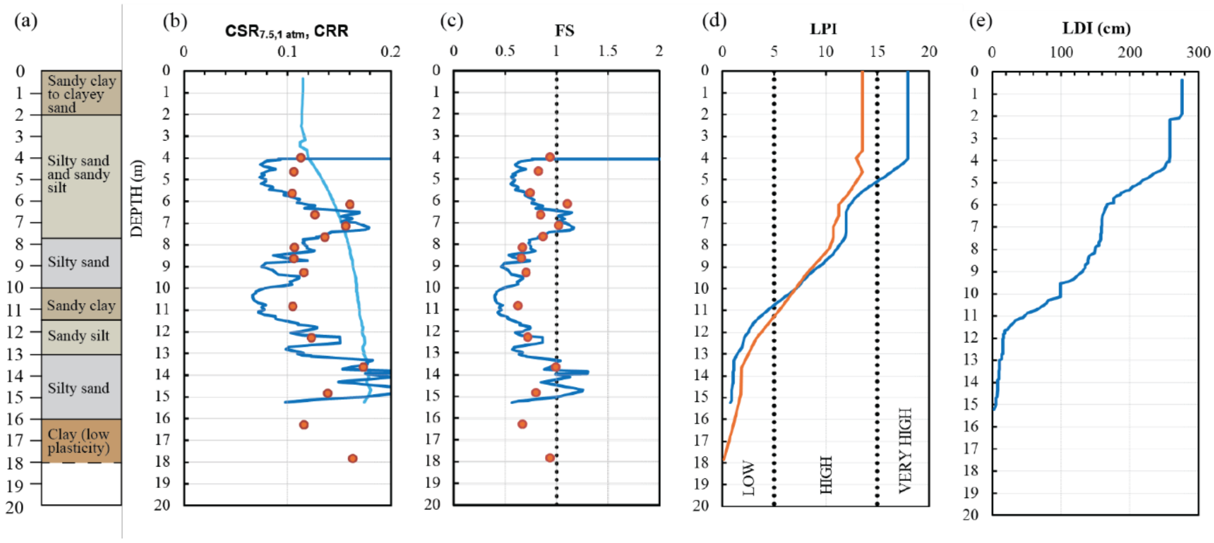

Fig. 4.15. a) Stratigraphic log of the first 18 m under the abutment n.2; b) plot of $CSR_{7.5}$ (cyan line) and CRR calculated from CPT (blue line) and SPT(orange points) versus depth; c) plot of FS calculated from CPT (blue line) and SPT (orange points) versus depth; d) plot of LPI calculated from CPT (blue line) and SPT (orange line), using the simplified methods proposed by Idriss and Boulanger (2008); e) plot of LDI calculated from CPT versus depth.

For a liquefiable layer measuring 14 m (estimated from SPT analysis), the potential lateral displacement was estimated using both the Lateral Displacement Index (LDI) as described by Zhang et al. (2004) and the predicted lateral displacement (D_H) proposed by Youd (2018). The resulting value ranged from 2.8 to 3.2 m, aligning with the findings of Price et al. (2000). It is important to note that the LDI (Fig. 4.14e) may underestimate the potential for lateral spread because the CPT was halted at a depth of 15 m, whereas analysis using the SPT indicates that the subsoil remains liquefiable at a depth of 18 m. The values of $(\mathrm{N}_1)_{60cs}$ acquired after the ground reinforcement and reported by Rollins et al. (2012) were used to repeat the evaluation of the liquefaction potential taking into account the variation in resistance to penetration of the subsoil. In this case, the LPI drops to 0 and, as a consequence of the absence of liquefiable layers, the D_H value obviously become 0.

4.2.2.3. Damage Assessment

The PGA and DH values were plotted in the fragility curves (Brandenberg et al., 2011) for the evaluation of damage on bridges in case of ground shaking and lateral spreading respectively, assuming that the PGD value is conceptually the same of D_H. The results are shown in Figure 4.16 a and b.

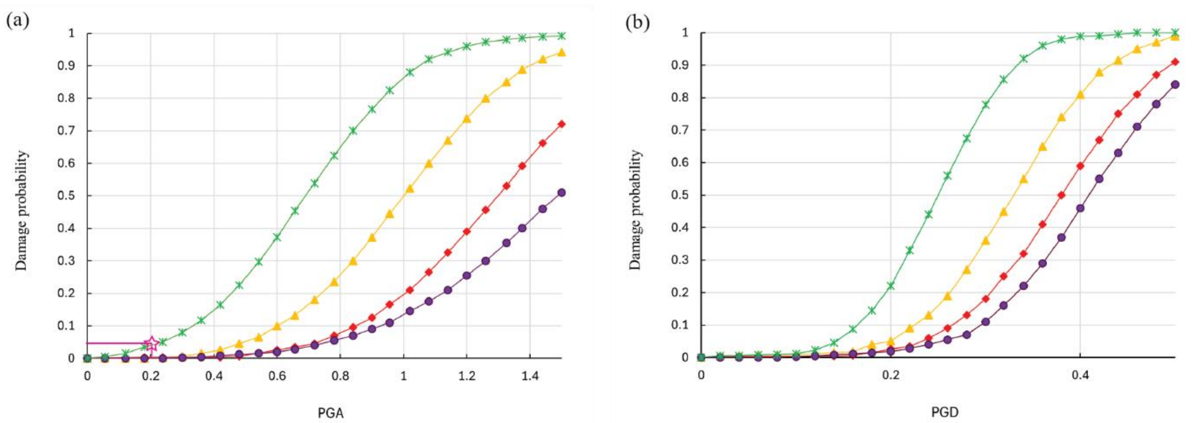

Fig. 4.16. Fragility curves for bridges with structural characteristics similar to Cherry Hill Interchange (modified from Brandenberg et al., 2011); green curves depict low damage, orange curves medium damage, red curves high damage and purple curves severe damage. a) damage probability versus PGA value; the pink star represents the value obtained from site response analysis. b) damage probability versus PGD; the value of the potential lateral displacement before the ground improvement is out of scale, so the damage probability is considered as 1 for each class of damage; conversely, after the reinforcement the damage probability drops to 0 for each curve.

4.2.3. Results

The input parameters for each class of damage (slight, moderate, extensive, collapse) before and after the ground improvement are reported in Table 3. After the soil reinforcement, the probability of damage due to liquefaction induced lateral-spreading went to 0, according to the results of liquefaction assessment made in Level 2 analysis.

Table 3. Input parameters for GETI before and after ground reinforcement

	$P(D_S)$	$P(D_{LQ})$	$\boldsymbol{P(D_H)}$ **before**	$\boldsymbol{P(D_H)}$ **after**	$P(D_R)$
Slight	0.04	0	**1**	**0**	0
Moderate	0.01	0	**1**	**0**	0
Extensive	0	0	**1**	**0**	0
Collapse	0	0	**1**	**0**	0

Before the soil treatment the main hazard is related to lateral spreading induced by liquefaction ($P(D_H) = 1$), while the effect of ground shaking is almost negligible ($P(D_S) = 0.04$). As outlined in the Level 1 analysis, the occurrence of a landslide in the studied area is not relevant due to the distance of the infrastructure from the mountain range, so the probability of damage derived from rockfall was setting to 0 ($P(D_R) = 0$).

The obtained values of damage were put into the equations 3.36a, 3.36b, 3.36c, 3.36d to calculate the GETI, as follows:

$$\boldsymbol{GETI_S} = 0.04 + 0 + 1 + \ 0 - 0.04 * 0 - 0.04 * 1 - 0.04 * 0 - 0 * 1 - 0 * 0 - 1 * 0 + 0.04 * 0 * 1 + 0.04 * 1 * 0 + 0 * 1 * 0 - 0.04 * 0 * 1 * 0 = 1 = \mathbf{100}\%$$

$$\boldsymbol{GETI_M} = 0.01 + 0 + 1 + \ 0 - 0.01 * 0 - 0.01 * 1 - 0.01 * 0 - 0 * 1 - 0 * 0 - 1 * 0 + 0.01 * 0 * 1 + 0.01 * 1 * 0 + 0 * 1 * 0 - 0.01 * 0 * 1 * 0 = 1 = \mathbf{100}\%$$

$$\boldsymbol{GETI_E} = 0 + 0 + 1 + \ 0 - 0 * 0 - 0 * 1 - 0 * 0 - 0 * 1 - 0 * 0 - 1 * 0 + 0 * 0 * 1 + 0 * 1 * 0 + 0 * 1 * 0 - 0 * 0 * 1 * 0 = 1 = \mathbf{100}\%$$

$$\boldsymbol{GETI_C} = 0 + 0 + 1 + \ 0 - 0 * 0 - 0 * 1 - 0 * 0 - 0 * 1 - 0 * 0 - 1 * 0 + 0 * 0 * 1 + 0 * 1 * 0 + 0 * 1 * 0 - 0 * 0 * 1 * 0 = 1 = \mathbf{100}\%$$

The GETI was calculated again considering the results of liquefaction-induced lateral spread assessment, as follows:

$$\boldsymbol{GETI_S} = 0.04 + 0 + 0 + \ 0 - 0.04 * 0 - 0.04 * 0 - 0.04 * 0 - 0 * 0 - 0 * 0 - 0 * 0 + 0.04 * 0 * 0 + 0.04 * 0 * 0 + 0 * 0 * 0 - 0.04 * 0 * 0 * 0 = 0.04 = \mathbf{4}\%$$

$$\boldsymbol{GETI_M} = 0.01 + 0 + 0 + \ 0 - 0.01 * 0 - 0.01 * 0 - 0.01 * 0 - 0 * 0 - 0 * 0 - 0 * 0 + 0.01 * 0 * 0 + 0.01 * 0 * 0 + 0 * 0 * 0 - 0.01 * 0 * 0 * 0 = 0.01 = \mathbf{1}\%$$

$$\boldsymbol{GETI_E} = 0 + 0 + 0 + \ 0 - 0 * 0 - 0 * 0 - 0 * 0 - 0 * 0 - 0 * 0 - 0 * 0 + 0 * 0 * 0 + 0 * 0 * 0 + 0 * 0 * 0 - 0 * 0 * 0 * 0 = 0 = \mathbf{0}\%$$

$$\boldsymbol{GETI_C} = 0 + 0 + 0 + \ 0 - 0 * 0 - 0 * 0 - 0 * 0 - 0 * 0 - 0 * 0 - 0 * 0 + 0 * 0 * 0 + 0 * 0 * 0 + 0 * 0 * 0 - 0 * 0 * 0 * 0 = 0 = \mathbf{0}\%$$

The results in terms of GETI index are finally shown in Table 4 before and after soil improvement, for each class of damage ($GETI_S$ is the index in case of slight damage; $GETI_M$ in case of moderate damage; $GETI_E$ in case of extensive damage; $GETI_C$ in case of collapse).

Table 4. Results after computing GETI for each class of damage before and after ground reinforcement

	$P(\mathrm{D})$ % before	$P(D)$% after
$GETI_S$	100	4
$GETI_M$	100	1
$GETI_E$	100	0
$GETI_C$	100	0

5. DISCUSSION AND CONCLUSIONS

Current international regulations (§2.3) on the assessment of natural risks potentially affecting linear infrastructures (e.g., road and highway bridges and viaducts) consider exclusively direct hydrological hazards, landslides, and seismic shaking, without taking into account the origin of the phenomena, their possible interactions, or their secondary effects. However, in recent years, a series of events caused by both seismic activity and the increasing frequency and intensity of extreme weather events has highlighted, in Italy and more generally worldwide (§2.3), the need for a multi-hazard approach (§2.1) that can account for all primary and secondary natural hazards that may interact with infrastructures and with each other. In this context, this thesis work is situated, introducing the development of a geological-geotechnical index called GETI which, using a hybrid statistical approach combining Bayesian Network and Fault Tree analysis, aims to provide an effective and practical tool for risk assessment of linear infrastructures.

The conceptualization of the index starts from a single primary hazard, seismic hazard, due to the geological characteristics of the Italian territory and, therefore, hazards with the greatest impact on local structures (§3). Further major hazards of significant relevance both in Italy and worldwide, such as those arising from extreme weather events and, more generally, from hydrogeological issues, will be the focus of further developments following this thesis work. In this sense, the concept of multi-hazard overlaps with that of cascade effect, with the definition of a primary hazard and the secondary hazards connected to it. The earthquake is therefore considered a primary hazard, which can lead to secondary effects such as landslides/rockfall, soil liquefaction/lateral spreading, and ground shaking (including amplification effects due to local geotechnical conditions), all of which can interfere with the structure and cause damage. A fundamental initial assumption made in structuring the index (§3.3) is that the secondary hazards act simultaneously on the structure, with effects that are clearly distinguishable and can be evaluated without overlapping. In this perspective, landslides and rockfall are treated as distinct hazards, recognizing that they are entirely separate physical events with unique predisposing factors and dynamics that do not intersect (§3.1.2.4).

Additionally, for rockfall, the geotechnical parameter used to assess potential structural damage is the impact velocity of the blocks, whereas for landslides, it is the horizontal movement of the foundation soil or piers. Consequently, the fragility curves for these two phenomena are different, reflecting the distinct physical processes involved, as the structural effects of horizontal displacement (landslide) and the direct impact of rock blocks (rockfall) are separate and identifiable (3.2.4). However, in the case of liquefaction-induced lateral spread and certain earthquake-induced landslides, there can be an overlap due to their simultaneous and combined effects on bridge foundations. This overlap is addressed in the model by employing a fragility surface that evaluates the concurrent occurrence of both phenomena, using the same parameter defined as the permanent horizontal displacement.

To take into account this kind of issue, a hybrid statistical approach using Bayesian methods and fault tree analysis has been chosen. The application of a hybrid BN-FTA model, proposed and validated by Kwang et al. (2017, 2018), allows us, through the use of the minimal cut-set (Eq. 3.31), to maintain the condition of independence of the effects and, therefore, to apply conditional probability to calculate the expected damage to a structure in the event of an earthquake. It is important to highlight that the damage index cannot be defined as a risk index sensu stricto, since the earthquake is considered with a fixed scenario, i.e. a prescribed value of peak ground acceleration or acceleration response spectra associated to the value of the return period selected for the seismic safety assessment of the structure. Furthermore, the probability of occurrence of secondary hazards is not evaluated: secondary earthquake hazards are considered present/absent using the susceptibility of the area and the likelihood of the phenomenon occurring based on charts and, therefore, on historical data at level 1 or via numerical/simplified quantitative methods at level 2.

The difficulties of a statistical approach to risk assessment in the case of earthquakes, especially in light of the "cascading effect", are many. First and foremost, not all seismogenic sources are known, there is no certain information on the return periods of characteristic earthquakes, and not all failure mechanisms are understood. Most importantly, the probability of an earthquake occurring at a specific moment is essentially close to zero, which would mean that the probability of occurrence of secondary effects, and therefore of damage, drops to extremely low and thus negligible values. These extremely low values can lead to misunderstood underestimation of the real seismic risk to which an infrastructure is exposed. This becomes even more evident if one calculates the probability of interaction between a secondary hazard and a given structure. On the other hand, the normative approach guarantees a realistic earthquake occurrence scenario within the considered time interval. Moreover, the adopted scenario makes it possible to have a percentage value of damage in the event of a seismic event that is easy to read and immediately interpret as is related to the even assumed for the design or the seismic safety assessment of the infrastructure.

The objective behind the development of the index is to provide road and highway network managers with an effective and easy-to-use tool for assessing seismic risk, from a multi-hazard perspective, on bridges and viaducts, as well as to establish a scale of priority for mitigation actions. The contributions of individual secondary effects to the probability of damage to the structure can, in fact, indicate to managers which intervention is most suitable to reduce the likelihood of damage. For example, if the main contribution comes from shaking, it may be appropriate to intervene on the superstructure, whereas in the case of ground instability phenomena (landslides and/or liquefaction), it may be advisable to allocate economic resources to ground consolidation or reinforcement interventions.

To test the correct functionality of GETI, two case studies were considered, one Italian and one international. The motivation lies in verifying that the index can be used under different conditions and with varying levels of knowledge. It is important to emphasize that, since this is a statistical index, validation through the selected case studies was not carried out as a back-analysis, but solely to evaluate the actual applicability and usefulness of the procedure, as well as its sensitivity to changing ground conditions.

The first case study considered in this work is the viaduct in Avezzano (Central Italy), selected for its location near a heavily fractured mountain slope in a high seismicity area, its proximity to active and capable faults, and a subsoil composed of alternating recent lacustrine deposits and slope/landslide deposits (§4.1). Despite the absence of landslide hazard indications for the area in the relevant national catalogs, Level 1 analysis highlighted the occurrence in the past of landslide phenomena along the southern part of the slope near the viaduct, with block sizes sometimes exceeding 2 meters in diameter. The analysis of the stratigraphy from boreholes conducted near the piers during the construction of the viaduct, as well as the morphological analysis of the slope using a 1-meter resolution DTM derived from LiDAR data, allowed the identification of probable past landslide events even in the area of interest.

The information obtained in Level 1 was then used in the more in-depth studies of Level 2, starting with the site response analysis, considering a return period of 712 years, an expected acceleration value of 0.28 g was applied at the outcropping bedrock. A PGA value at foundation level of 0.34 g was calculated by site response analyses, which indicates an amplification of seismic motion due to the characteristics of the soil, largely composed of recent and therefore soft lacustrine sediments (§4.1.2.1). The obtained PGA value was used to calculate the value of horizontal velocity for a rockfall analysis to determine the block runout as well as the impact velocity of the blocks on the structure.

The PGA values and block impact velocities on the structure obtained in this way were used as input parameters in the fragility curves developed by Brandenberg et al. (2011) and Xie et al. (2020) for the assessment of damage resulting from ground shaking and rockfall impact, respectively. In this step, one of the critical issues of the index in its application to real cases emerged: the curves developed by Xie et al. (2020) are limited to two types of piers: those with a circular cross-section and those with a square cross-section. The case study, in which the structure could potentially be affected by rockfall, was carried out by approximating the piers as having a square cross-section, even though in reality they have a rectangular cross-section, and are therefore potentially more resistant to the lateral impacts considered in the simulation. This may have evidently led to a potential overestimation of the damage to the structure resulting from rockfall.

The second case study considered is that of the Cherry Hill Interchange, a viaduct located in Farmington, Utah (USA), a few kilometers north of Salt Lake City. The main feature of this structure is first and foremost its position, very close to the surface trace of the Wasatch fault, which is considered an active and capable listric fault, dipping to the southwest with a near-vertical slope for at least the first 2 km of depth. This means that the viaduct stands on a considerable thickness of lacustrine-alluvial deposits, with the uppermost 200 meters towards the surface being of recent deposition and, therefore, soft and generally loose (§ 4.2). The level 1 analysis made it possible to reconstruct the tectonic and stratigraphic framework at a level of detail that is sufficiently accurate and thorough to allow for advanced level 2 analyses without the need for further on-site investigations.

The site, susceptible to lateral spreading induced by liquefaction, underwent ground reinforcement beneath the viaduct by means of gravel columns installed in the layers identified as liquefiable in studies conducted after the structure's construction. To assess the applicability of the index to real-world cases, it was interesting to observe that, in level 2 analyses conducted with parameters prior to the reinforcement intervention, there is a clear predominance of ground horizontal displacement, estimated at about 3 meters, caused by lateral spreading induced by liquefaction at depths between 4 and 16 meters, while the contribution from shaking is negligible. Conversely, when the analyses are repeated using the penetration resistance values measured after the installation of the gravel columns, the contribution from liquefaction drops to zero, leaving the damage attributable solely to shaking. This demonstrates how the GETI is able to highlight the contributions of individual hazards to the total earthquake-induced damage, allowing for a simple and immediate understanding of which hazard is actually and predominantly impacting the structure. The index is therefore also well-suited to quantifying the reduction in the probability of damage resulting from the implementation of an intervention to reduce the vulnerabilities of the structure-foundation-soil system.

Both case studies show how the estimation of expected damage, carried out for each individual damage level and considered as a standalone scenario, yields plausible and consistent results (Tab. 5.1 e 5.2). In areas with limited coverage from literature studies, mapping, and official catalogs, correctly estimating the presence of hazards, susceptibility, and, consequently, the expected damage becomes complex and requires integration with newly conducted investigations. This means that the fewer reliable data and information are available for a given structure and for the geological and geotechnical context in which it is located, the greater the difficulties in applying the index and the higher the costs required to achieve a reasonably accurate output. In general, it is important to keep in mind that, for an accurate assessment of the expected damage to a linear structure in the event of an earthquake, it is always necessary to supplement data collected from previous studies with new, specifically conducted investigations. This is especially true for advanced level 2 analyses, which lead to the final calculation of the index.

A limitation of the index is its applicability, in its current formulation, only to the seismic field. As explained in the introductory chapters, this limitation stems from a necessary simplification for the development of the model within the scope of this doctoral thesis. Another assumption required for simplifying the problem and for developing the index is to consider the damaging effects of independent hazards, as these are assumed to act simultaneously on the structure. This is not always true in reality; consider, for example, the triggering of landslides, which sometimes occurs (especially in clayey soils) a significant amount of time after an earthquake and is sufficient to make their effects on the structure no longer act in parallel, but in series. Future developments will allow these issues to be addressed and, presumably, resolved, extending the index to a true multi-hazard context. Moreover, as highlighted in the first case study, it seems necessary to develop ad hoc fragility curves for the hazards considered in the index, in order to overcome the limitations of overly generic curves and provide results as close as possible to the reality of the structure in question.

Despite of that, the two case studies allow us to conclude that the GETI, in its current formulation (§3.3), achieves the goal of determining the expected percentage of damage in the event of an earthquake, taking into account possible damage caused by its secondary effects (ground shaking, soil liquefaction, lateral spreading, landslide/rockfall). Furthermore, the index makes it possible to rank these effects, thus providing an effective tool for network managers to plan interventions.

REFERENCES

Ambraseys N.N. (1988). *Engineering Seismology*. Earthquake Engineering and Structural Dynamics, 17, 1-105. https://doi.org/10.1002/eqe.4290170101

Andrews D.C.A., Martin G.R. (2000). *Criteria for Liquefaction of Silty Soils*. Proceedings of the 12th World Conference on Earthquake Engineering (WCEE), 1-8.

Andrus R.D., Stokoe K.H. (2000). *Liquefaction Resistance of Soils from Shear-Wave Velocity.* Journal of Geotechnical and Geonvironmental Engineering, 126 (**11**), 1015-1025.

ASCE (2017). *Infrastructure Report Card: A Comprehensive Assessment of America's Infrastructure.* American Society of Civil Engineers (ASCE). https://www.infrastructurereportcard.org/wp-content/uploads/2016/10/2017-Infrastructure-Report-Card.pdf

Ashayer P. (2007). *Application of rigid body impact mechanics and discrete element modeling to rockfall simulation*. PhD Thesis. University of Toronto (Canada).

Aubry D., Modaressi A. (1996). *GEFDYN – Manuel Scientifique.* Ecole Centrale Paris. France

Bardet J.P., Ichii K., Lin C.H. (2000). *EERA - A computer program for Equivalent-linear Earthquake site Response Analyses of layered soil deposits*. Department of Civil Engineering, University of Southern California, USA.

Bensi M., Der Kiureghian A., Straub D. (2011). *Bayesian network modeling of correlated random variables drawn from a Gaussian random field*. Structural Safety, 33 (**6**), 317-332.

Blevins R.L, Aubertin G.M., Holowaychuk N. (1968). *A Technique for Obtaining Undisturbed Soil Samples by Freezing in Situ.* Soil Science Society of America Journal, 32 (**5**), 741-742. https://doi.org/10.2136/sssaj1968.03615995003200050045x

Blitzstein J.K., Hwang J. (2015) *Introduction to Probability*. Texts in Statistical Science Series. Chapman & Hall/CRC Press, Taylor and Francis Group, 570 pp.

Boncio P., Amoroso S., Vessia G., Francescone M., Nardone M., Monaco P., Famiani D., Di Naccio D., Mercuri A., Manuel M.R., Galadini F., Milana G. (2018). *Evaluation of liquefaction potential in an intermountain Quaternary lacustrine basin (Fucino basin, central Italy)*. Bulletin of Earthquake Engineering, 16, 91-111. https://doi.org/10.1007/s10518-017-0201-z

Boncio P., Amoroso S., Galadini F., Galderisi A., Iezzi G., Liberi F. (2020). *Earthquake-induced liquefaction features in a late Quaternary fine-grained lacustrine succession (Fucino Lake, Italy): Implications for microzonation studies*. Engineering Geology, 272, 105621. https://doi.org/10.1016/j.enggeo.2020.105621

Boulanger R.W., Idriss I.M. (2014). *CPT and SPT based liquefaction triggering procedure*. Report No. UCD/CGM-14/01, Center for eotechnical Modelling, Department of Civil and Enviromentally Engineering, Univ. California, California, 134 pp., https://doi.org/10.1061/(ASCE)GT.1973-5606.0001388 .

Bozorgnia Y, K. W. Campbell K. W. (2016). *Ground Motion Model for the Vertical-toHorizontal (V/H) Ratios of PGA, PGV, and Response Spectra.* Earthquake Spectra, 32 (**2**). https://doi.org/10.1193/100614eqs151m

Brandenberg S.J., Zhang J., Kashigahndi P., Huo Y., Zhao M. (2011). *Demand Fragility Surfaces for Bridges in Liquefied and Laterally Spreading Ground*. Berkeley, CA, US: Pacific Earthquake Engineering Research Center, University of California. PEER Report 2011/01, pp 162.

Brando G., De Matteis G., Spacone E. (2017). *Predictive model for the seismic vulnerability assessment of small historic centres: Application to the inner Abruzzi Region in Italy*. Engineering Structures, 153, 81-96. https://doi.org/10.1016/j.engstruct.2017.10.013

Bray J.D., Sancio R.B. (2006). *Assessment of the Liquefaction Susceptibility of Fine-Grained Soils*. J. Geotech. Geoenviron. Eng., 132,1165-1177. https://doi.org/10.1061/(ASCE)1090-0241(2006)132:9(1165)

BRP (2003). *Recommendations for Bridge and Tunnel Security*. Prepared by The Blue Ribbon Panel (BRP) on Bridge and Tunnel Security for The American Association of State Highway and Transportation Officials (AASHTO), 64 pp. Available at: https://www.fhwa.dot.gov/bridge/security/brp.pdf

Cao Z., Youd T.L. & Yuan X. (2011). *Gravelly soils that liquefied during 2008 Wenchuan, China earthquake, Ms=8*. Soil Dyn. Earthq. Eng., 31, 1132-1143, https://doi.org/10.1016/j.soildyn.2011.04.001

Cao Z., Youd T.L. & Yuan X. (2013). *Chinese dynamic penetration test for liquefaction evaluation in gravelly soils*. J. Geotech. Geoenviron. Eng., 139(8), 1320-1333, https://doi.org/10.1061/(ASCE)GT.1943-5606.0000857 .

Cao Z., Liu Z., Xu G., Lin H., Li X., Nikitas N. (2024). *Risk assessment and prevention for typical railway bridge pier under rockfall impact*. Structures, 62, 106178. https://doi.org/10.1016/j.istruc.2024.106178

Castilla R.A., Audemard F.A. (2007). *Sand blows as a potential tool for magnitude estimation of pre-instrumental earthquakes*. Journal of Seismology, 11, 473-487. https://doi.org/10.1007/s10950-007-9065-z

Chang W.L., Smith R.B., Meertens C.M., Harris R.A. (2006). *Contemporary deformation of the Wasatch Fault, Utah, from GPS measurements with implications for interseismic fault behavior and earthquake hazard: Observations and kinematic analysis*. J. Geophy. Res., 111, B11405

Chávez-García F.J., Bard P. (1994). *Site effects in Mexico City eight years after the September 1985 Michoacan earthquakes*. Soil Dynamics and Earthquake Engineering, 13, 229-247.

Chen G., Zheng L., Zhang Y., Wu J. (2013). *Numerical Simulation in Rockfall Analysis: A Close Comparison of 2-D and 3-D DDA*. Rock Mechanics Rock Engineering, 46, 527-541. https://doi.org/10.1007/s00603-012-0360-9

Chinese Design Code (2021). Design code for buildings foundation of Chengdu region. DB51/T5026-2001, Administration of Quality and Technology, Chengdu, China. [In Chinese].

Crespellani T., Madiai C., Vannucchi G. (1998). *Earthquake destructiveness potential factor and slope stability*. Géotechnique, 48 (**3**), 411- 419.

Crespellani T., Facciorusso J. (2010). *Dinamica dei terreni per le applicazioni sismiche*. Flaccovio Editore. pp 380. ISBN 978-8857900421.

CS450 (2021). *Highway Structures & Bridges Inspection & Assessment CS 450 Inspection of highway structures.* Highways England, UK.

CSRS16 (2023). *Infrastrutture: focus con Anas sul ponte di Rotella. Commissario Straordinario Ricostruzione Sisma 2016*, Presidenza del Consiglio dei Ministri 2023, https://sisma2016.gov.it/2023/09/05/infrastrutture-focus-con-anas-sul-ponte-di-rotella/

Cubrinovsky M., Bray J.D., de la Torre C., Olsen M., Bradley B., Chiaro G., Stocks E., Wotherspoon L., Krall T. (2018). *Liquefaction-induced damage and CPT characterization of the reclamations at CentrePort, Wellington*. Bull. Seismol. Soc. Am., 108(3B), 1695-1708, https://doi.org/10.1785/0120170246

Darendeli M.B. (2001). *Development of a New Family of Normalized Modulus Reduction and Material Damping Curves*. Ph.D. Dissertation, University of Texas at Austin, 362 pp

DEEPSOIL V7.1 (2024). *A nonlinear and Equivalent Linear Seismic Site Response of 1-D Soil Columns*, User Manual. Board of Trustees of University of Illinois at Urbana-Champaign, Urbana, IL.

De Matteis G., Brando G., Corlito V. (2019). *Predictive model for seismic vulnerability assessment of churches based on the 2009 L'Aquila earthquake*. Bulletin of Earthquake Engineering, 17, 4909-4936. https://doi.org/10.1007/s10518-019-00656-7

Descoeudres F., Zimmermann T. (1987). *Three-dimensional dynamic calculation of rockfalls*. In Sixth international congress on rock mechanics. International Society for Rock Mechanics, Montreal. 337–342

Dilley M., Chen R. S., Deichmann U., Lerner-Lam A. L., Arnold M. (2005). *Natural Disaster Hotspots – A Global Risk Analysis*. Disaster Risk Management Series, World Bank, Washington, DC. http://hdl.handle.net/10986/7376 license:CC BY 3.0 IGO

Di Naccio D., Famiani D., Liberi F., et al. (2020). *Site effects and widespread susceptibility to permanent coseismic deformation in the Avezzano town (Fucino basin, Central Italy): constraints from detailed geological study*. Eng Geol., 270, 105583. https://doi.org/10.1016/j.enggeo.2020.105583

EduPro Civil System (1998). *ProShake – Ground Response Analysis Program*. EduPro Civil Systems, Inc. Sammamish, Washington (US)

FEMA (2023). *National Risk Index technical documentation.* U.S. Department of Homeland Security, United States of America.

FHWA (2009). *Risk Management Strategy for Bridges and Structures – Final Report.* Pennsylvania Department of Transportation, Bureau of Planning and Research, for The Federal Highway Administration, 160 pp. Available at: https://rosap.ntl.bts.gov/view/dot/39393/Email

Field E. H. (2015). *Computing Elastic‐Rebound‐Motivated Earthquake Probabilities in Unsegmented Fault Models: A New Methodology Supported by Physics‐Based Simulators*. Bulletin of the Seismological Society of America, 105 (**2A**), 544–559. https://doi.org/10.1785/0120140094

Fiore A., Ottaviani V. (2018). *Rischio sismico in Italia: analisi e prospettive per una prevenzione efficace in un Paese fragile*. Supplemento a Geologia dell'Ambiente, SIGEA, 1.

Galadini F., Galli P. (1999). *The Holocene paleoearthquakes on the 1915 Avezzano earthquake faults (central Italy): implications for active tectonics in the central Apennines*. Tectonophysics. 308,143–170

Galli P., Ferreli L. (1995). *A methodological approach for historical liquefaction research*. In "Perspectives in Paleoseismology", L. Serva and D.B. Slemmons, Eds. AEG Special Publication N.6, pp. 35-48.

Galli P. (2000). *New empirical relationships between magnitude and distance for liquefaction*. Tectonophysics, 324, 169–187.

Gardoni P., Der Kiureghian A., Mosalam K.M. (2002). *Probabilistic Models and Fragility Estimates for Bridges Components and Systems*. Berkeley, CA, US: Pacific Earthquake Engineering Research Center (PEER), University of California. Report 2002/13; pp 164.

Gatto M.P.A., Lentini V., Montrasio L., Castelli F. A. (2023). *Simplified semi-quantitive procedure based on the SLIP model for landslide risk assessment: the case study of Gioiosa Marea (Sicily, Italy)*. Landslides, 20, 1381–1403. https://doi.org/10.1007/s10346-023-02040-8

Gill J. C., Malamud B. D. (2014). *Reviewing and visualing the interactions of natural hazards*. Rev. Geophys., 52, 680-722. https://doi.org/10.1002/2013RG000445

Greiving S., Fleischhauer M., Luckenkotter J. (2006). *A methodology for an integrated risk assessment of spatially relevant hazards*. J. Environ. Planning and Management, 49 (**1**), 1-19. https://doi.org/10.1080/09640560500372800

Groholski D.R., Hashash Y.M.A., Kim B., Musgrove M., Harmon J., Stewart J.P. (2016). *Simplified Model for Small-Strain Nonlinearity and Strength in 1D Seismic Site Response Analysis.* Journal of Geotechnical and Geoenvironmental Engineering, 142 (**9**). https://doi.org/10.1061/(ASCE)GT.1943-5606.0001496

Guzzetti F., Malamud B.D., Turcotte D.L., Reichenbach P. (2002). *Power-law correlations of landslide areas in central Italy*. Earth and Planetary Science Letters, 195 (3–4), 169-183. https://doi.org/10.1016/S0012-821X(01)00589-1

Hanks J.C., Kanamori H. (1979). *A Moment Magnitude Scale*. Journal of Geophysical Research, 84 (**B5**), 2348-2350. https://doi.org/10.1029/JB084iB05p02348

Hart W.S., Quade J., Madsen D.B., Kaufman D.S., Oviatt C.G. (2004). *The 87Sr/86Sr ratios of lacustrine carbonates and lake-level history of the Bonneville paleolake system*. Geological Society of America Bulletin 116 (**9/10**), 1107-1119

Hashash Y.M.A., Park D. (2001). *Non-linear one-dimensional seismic ground motion propagation in the Mississippi embayment*. Engineering Geology, 62 (**1–3**), 185-206. https://doi.org/10.1016/S0013-7952(01)00061-8

HAZUS (2024). *Hazus Earthquake Model Technical Manual - Hazus 6.1*. Federal Emergency Management Agency (FEMA), USA. 477 pp

Hewitt K., Burton I. (1971). *The hazardousness of a place: a regional ecology of damaging events*. University of Toronto Press, 84 pp.

Hudson M., Idriss I.M., Beikae M. (1994). *QUAD4M: a computer program to evaluate the seismic response of soil structures using finite element procedures and incorporating a compliant base*, Dpt. of Civil and Envir. Eng., Univ. of California Davis, Davis (US)

Hunt C.B., Varnes H.D., Thomas H.E. (1953). *Lake Bonneville: Geology of Northern Utah Valley, Utah*. Geological Survey Professional Paper 257-A, United States Government Printing Office, Washington (USA).

Hwang H., Liu J.B., Chiu Y. (2001). *Seismic Fragility Analysis of Highway Bridges*. Sponsored by Mid-America Earthquake Center Technical Report MAEC RR-4 Project, Prepared by Center for Earthquake Research and Information University of Memphis (US), 127 pp.

ICSU (2012). *ICSU International Council for Science annual report 2012*. Printed by Agit Berlin, 40 pp. ISBN: 978-0-930357-90-0

Idriss I.M., Lysmer J., Hwang R., Seed H.B. (1973). *QUAD-4: A computer Program for Evaluating the Seismic Response of Soil Structures by Variable Damping Finite Element Procedures*, Earthquake Engineering Research Center, Report N. EERC 73-16, University of California, Berkeley (US).

Idriss I.M., Sun J.I. (1992). *SHAKE91 – A computer program for Conducting Equivalent Linear Seismic Response Analysis of Horizontally Layered Soil Deposits*. Center of Geotechnical Modeling, University of California, Davis, California (US).

Idriss I.M., Boulanger R.W. (2008). *Soil liquefaction during earthquakes*. Earthquake Engineering Research Institute (EERI), Oakland, California, USA. 237 pgg

IPCC (2022). *Climate Change 2022: Impacts, Adaptation and Vulnerability. Contribution of Working Group II to the Sixth Assessment Report of the Intergovernmental Panel on Climate Change* H.-O. Pörtner, D.C. Roberts, M. Tignor, E.S. Poloczanska, K. Mintenbeck, A. Alegría, M. Craig, S. Langsdorf, S. Löschke, V. Möller, A. Okem, B. Rama (eds.). Cambridge University Press. Cambridge University Press, Cambridge, UK and New York, NY, USA, 3056 pp., https://doi.org/10.1017/9781009325844

IRPI (2023). *Frane e fenomeni alluvionali in Italia settentrionale*. Istituto di Ricerca per la Protezione Idrogeologica (IRPI), Consiglio Nazionale delle Ricerche (CNR). https://polaris.irpi.cnr.it/frane-e-fenomeni-alluvionali-in-italia-settentrionale/

Iwasaki T., Tatsuoka F., Tokida K. & Yasuda S. (1978). *A practical method for assessing soil liquefaction potential based on case studies at various sites in Japan*. 2nd International Conference on Microzonation for Safer Construction Research and Application, 885-896. https://doi.org/10.1016/0261-7277(84)90027-5

Ji J., Cui H., Zhang T., Song J., Gao Y. (2022*). A GIS-based tool for probabilistic physical modelling and prediction of landslides: GIS-FORM landslide susceptibility analysis in seismic areas*. Landslides, 19, 2213–2231. https://doi.org/10.1007/s10346-022-01885-9

Kaklamanos J., Bradley B.A., Thompson E.M., Baise L.G. (2013). *Critical Parameters Affecting Bias and Variability in Site-Response Analyses Using KiK-net Downhole Array Data*. Bulletin of the Seismological Society of America, 103 (**3**), 1733–1749. https://doi.org/10.1785/0120120166

Kameshwar S., Padgett J.E. (2014). *Multi-hazard risk assessment of highway bridges subjected to earthquake and hurricane hazards*. Engineering Structures, 78, 154-166. https://doi.org/10.1016/j.engstruct.2014.05.016

Kappes M.S. (2011). *Multi-Hazard Risk Analyses: a Concept and its Implementation*. PhD Thesis, Vien University.

Kappes M.S., Keiler M., von Elverfeldt K., Glade T. (2012). *Challenges of analyzing multi-hazard risk: a review*. Nat. Hazards, 64, 1925-1958, https://doi.org/10.1007/s11069-012-0294-2

Keefer D.K. (1984). *Landslides caused by earthquakes*. GSA bulletin, 95 (**4**), 406-421. https://doi.org/10.1130/0016-7606(1984)95<406:LCBE>2.0.CO;2

Kefeer D.K. (2002). *Investigating Landslides Caused by Earthquakes – a Historical Review*. Surveys in Geophysics, 23, 473–510. https://doi.org/10.1023/A:1021274710840

Khakzad N., Khan F., Amyotte P. (2011). *Safety analysis in process facilities: Comparison of fault tree and Bayesian network approaches*. Reliability Engineering and System Safety, 96, 925-932. https://doi.org/10.1016/j.ress.2011.03.012

Kleber E.J., McKean A.P., Hiscock A.I., Hylland M.D., Hardwick C.L., McDonald G.N., Anderson Z.W., Bowman S.D., Willis G.C., Erickson B.A. (2021). *Geologic Setting Effects, and Proposed structural Model for the 18 March 2020 MW 5.7 Magna, Utah, Earthquake*. Seismol. Rese. Lett. 92(2A), 710-724

Kondner R.L. (1963). *Hyperbolic Stress-Strain Response: Cohesive Soils*. Journal of the Soil Mechanics and Foundations Division, 89 (**1**). https://doi.org/10.1061/JSFEAQ.0000479

Koks E.E., Rozenberg J., Zorn C., Tariverdi M., Vousdoukas M., Fraser S.A., Hall J.W., Hallegatte S. (2019). *A global multi-hazard risk analysis of road and railway infrastructure assets*. Nat. Commun., 10, 2677. https://doi.org/10.1038/s41467-019-10442-3

Kokusho T., Yoshida Y. (1997). *SPT N-Value and S-Wave Velocity for Gravelly Soils with Different Grain Size Distribution*. Soils and Foundations, 37 (**4**), 105-113. https://doi.org/10.3208/sandf.37.4_105

Kottke A.R., Rathje E. (2008). *Technical Manual for Strata*. Pacific Earthquake Engineering Research Center PEER Report 2008/10. University of California, Berkeley (US)

Kramer S.L, Stewart J.P. (2025). *Geotechnical Earthquake Engineering*. CRC Press, Taylor and Francis Group, 1042 pp. ISBN 978-1032842745

Kwang S., Gupta A. (2017). *Probabilistic risk assessment framework for structural systems under multiple hazards using Bayesian statistics*. Nuclear Engineering and Design, 315, 20-34. http://dx.doi.org/10.1016/j.nucengdes.2017.02.009

Kwang S., Gupta A., Dinh N. (2018). *Probabilistic risk assessment based model validation method using Bayesian network*. Reliability Engineering and System Safety, 169, 380-393. https://doi.org/10.1016/j.ress.2017.09.013

Lay T., Wallace T.C. (1995). *Modern Global Seismology*. Academic Press, San Diego, California, USA, 535 pp. ISBN 978-0-12-732870-6.

Lemons D.R., Chan M.A. (1999). *Facies Architecture and Sequence Stratigraphy of Fine-Grained Lacustrine Deltas Along the Eastern Margin of Late Pleistocene Lake Bonneville, Northern Utah and Southern Idaho*. American Association of Petroleum Geologists Bulletin 83(**4**), 635-665

Liao S.S.C., Venaziano D., Whitman R.V. (1988). *Regression models for evaluating liquefaction probability*. J. Geotech. Eng., 114 (**4**), 389-411, https://doi.org/10.1061/(ASCE)0733-9410(1988)114:4(389)

Locati M., Camassi R., Rovida A., Ercolani E., Bernardini F., Castelli V., Caracciolo C.H., Tertulliani A., Rossi A., Azzaro R., D'Amico S., Antonucci A. (2022). *Database Macrosismico Italiano (DBMI15), versione 4.0 [Data set].* Istituto Nazionale di Geofisica e Vulcanologia (INGV). https://doi.org/10.13127/dbmi/dbmi15.4

López-Saavedra M., Martí J. (2023). *Reviewing the multi-hazard concept. Application to volcanic islands*. Earth-Science Reviews, 236, 104286. https://doi.org/10.1016/j.earscirev.2022.104286

Lo Presti D.C.F., Pallara O., Froio F., Rinolfi A., Jamiolkowski M. (2006). *Stress-strain-strength behaviour of undisturbed and reconstituted gravelly soil samples*. Rivista Italiana di Geotecnica, 1, 9-27.

Machette M.N., Personius S.F., Nelson A.R. (1991). *The Wasatch fault zone, Utah-segmentation and history of Holocene earthquakes*. J. Struct. Geol., 13(2), 137-149

Marzocchi W., Garcia-Aristizabal A., Gasparini P., Mastellone M.L., Di Ruocco A. (2012). *Basic principles of multi-risk assessment: a case study in Italy.* Nat. Hazards, 62 (**2**), 551-573. https://doi.org/10.1007/s11069-012-0092-x

Masing G. (1926). *Metallographische Mitteilungen*. Naturwissenschaften, 14, 142-144. https://doi.org/10.1007/BF01507300

Matasović N. (1993). *Cyclic Characterization of Liquefiable Sands*. Journal of Geotechnical Engineering. 119, 11. https://doi.org/10.1061/(ASCE)0733-9410(1993)119:11(1805)

Matasović N., Ordóñez G.A. (2010). *D-MOD2000: A computer program for seismic response analysis of horizontally layered soil deposits, earthfill dams, and solid waste landfills, User's Manual.* GeoMotions, LLC, Lacey, Washington, D.C. (US)

Maurer B.W., Green R.A., Quigley M.C., Bastin S. (2015). *Development of magnitude-bound relations for paleoliquefaction analyses: New Zealand case study.* Engineering Geology, 197, 253-266. https://doi.org/10.1016/j.enggeo.2015.08.023

Maurer B.W. (2017). *Field-testing liquefaction models based on geospatial vs. geotechnical data*. Proceedings of the 6th International Young Geotechnical Engineers' Conference (iYGEC6), Seoul, Korea. Published by the International Society of Mechanics and Geotechnical Engineering (ISSMGE).

Mayne P.W., Coop M.R., Springman S.M., Huang A. & Zornberg J.G. (2009). *Geomaterial behavior and testing*. Proceedings of the 17th International Conference on Soil Mechanics and Geotechnical Engineering, 2777-2873

Mayoral J.M., Asimaki D., Tepalcapa S., Wood C., Roman-de la Sancha A., Hutchinson T., Franke K, Montalva G. (2019). *Site effects in Mexico City basin: Past and present.* Soil Dynamics and Earthquake Engineering, 121,369-382. https://doi.org/10.1016/j.soildyn.2019.02.028

McCalpin J.P. (2009). *Paleoseismology*. Elsevier, London. ISBN: 978-0-12-373576-8

McDonald G.N., Ashland F.X. (2008). *Earthquake site-conditions map for the Wasatch front urban corridor, Utah*. Special Study 125 Utah Geological Survey, Salt Lake City, Utah (USA)

MIMS (2022). *Linee Guida per la Classificazione e Gestione del Rischio, la Valutazione della Sicurezza ed il Monitoraggio dei Ponti Esistenti*. Ministero delle Infrastrutture e della Mobilità Sostenibili Consiglio Superiore dei Lavori Pubblici.

Montrasio L., Gatto M.P.A., Miodini C. (2023). *The role of plants in the prevention of soil-slip: the G-SLIP model and its application on territorial scale through G-XSLIP platform*. Landslides, 20, 1149–1165. https://doi.org/10.1007/s10346-023-02031-9

Moore I.D., Grayson R.B., Ladson A.R. (1991). *Digital Terrain Modelling: A Review of Hydrological, Geomorphological, and Biological Applications*. Hydrological Processes, 5, 3-30. https://doi.org/10.1002/hyp.3360050103

NCHRP (2016). *Assessing Risk for Bridge Management Final Report*. American Association of State Highway and Transportation Official (AASHTO) National Cooperative Highway Research Project (NCHRP) 20-07, Task 378, 121 pp. Available at: https://www.tpm-portal.com/document/assessing-risk-for-bridge-management-nchrp-20-07-378/

Newmark, N.M. (1965). *Effects of Earthquakes on Dams and Embankments*. Geotechnique, 15, 139-160. http://dx.doi.org/10.1680/geot.1965.15.2.139

NTC (2018). *Aggiornamento delle "Norme tecniche per le costruzioni".* D.M. 17 gennaio 2018, pubblicato sul Supplemento ordinario alla Gazzetta Ufficiale, n.42 del 20 febbraio 2018, Serie generale. 372 pp

Obermeier S.F. (1996). *Use of liquefaction-induced features for paleoseismic analysis — An overview of how seismic liquefaction features can be distinguished from other features and how their regional distribution and properties of source sediment can be used to infer the location and strength of Holocene paleo-earthquakes*. Engineering Geology, 44 (**1-4**), 1-76. https://doi.org/10.1016/S0013-7952(96)00040-3

Odeh J.D. (2002). *Natural Hazards Vulnerability Assessment for Statewide mitigation Planning in Rhode Islend*. Nat. Hazards Rev., 3 (**4**), 177-187. https://doi.org/10.1061/(ASCE)1527-6988(2002)3:4(177)

Pagliaroli A. (2018). *Key issues in Seismic Microzonation studies: lessons from recent experiences in Italy.* Rivista Italiana di Geotecnica, 1, 5-48. https://doi.org/10.19199/2018.1.0557-1405.05

Pang G., Koper K.D., Mesimeri M., Pankow K.L., Baker B., Farrell J., Holt J., Hale J.M., Robertson P., Burlacu R., Pechmann J.C., Whidden K., Holt M.M., Allam A., DuRoss C. (2020). *Seismic Analysis of the 2020 Magna, Utah, Earthquake Sequence: Evidence for a Listric Wasatch Fault*. Geophys. Res. Lett. 47, e2020GL089798

Parsons, T. (2006). *Chapter 7 The Basin and Range Province*. Dev. Geotect. 25, 277-324.

Park D., Hashash Y.M.A. (2004). *Soil damping formulation in nonlinear time domain site response analysis*. Journal of Earthquake Engineering, 8 (**2**), 249-274. https://doi.org/10.1142/S1363246904001420

Pei T., Qiu T.. (2024). *Landslide susceptibility mapping using physics guided machine learning: a case study of a debris flow event in Colorado Front Range*. Acta Geotechnica, 19, 6617–6641. https://doi.org/10.1007/s11440-024-02384-y

Piattelli V. (2024). *Analisi Della Suscettività Da Frane Da Crollo Nel Contesto Di Aree Sismiche E Valutazione Della Pericolosità: Casi Di Studio In Ambienti Montani, Collinari E Costieri (Regione Abruzzo, Italia Centrale)*. Doctorate thesis. University "G. d'Annunzio" of Chieti-Pescara (IT)

Pisanò F., Jeremić B. (2014). *Simulating stiffness degradation and damping in soils via a simple visco-elastic–plastic model*. Soil Dynamics and Earthquake Engineering, 63, 98-109. https://doi.org/10.1016/j.soildyn.2014.02.014

Price B.E., Stilson M., Hansen M., Bischoff J., Youd L. (2000). *Liquefaction and Lateral Spread Evaluation and Mitigation for Highway Overpass Structure*. Transportation Research Record 1736, 00-1735, Utah Department of Transportation, Salt Lake City, UT (USA)

Régnier J. et al. (2016). *International Benchmark on Numerical Simulations for 1D, Nonlinear Site Response (PRENOLIN): Verification Phase Based on Canonical Cases*. Bulletin of the Seismological Society of America, 106 (**5**), 2112–2135. https://doi.org/10.1785/0120150284

Reynolds, J. M. (1997). *An Introduction to Applied and Environmental Geophysics*. Chichester: John Wiley and Sons Ltd. 796p.

Rodriguez-Pascua M.A., Calvo J.P., De Vicente G., Gomez-Gras D. (2020). *Soft sediment deformation structures interpreted as seismites in lacustrine sediments of the Prebetic Zone, SE Spain, and their potential use as indicators of earthquake magnitudes during the Late Miocene*. Sediment. Geol., 135, 117-135, https://doi.org/10.1016/S0037-0738(00)00067-1

Rollins K.M., Price B.E., Dibb E., Higbee J.B. (2012*). Liquefaction Mitigation of Silty Sands in Utah using Stone Columns with Wick Drains*. Ground Modification and Seismic Mitigation, GSP 152.

Rollins K.M., Roy J., Athanasopoulos-Zekkos A., Zekkos D., Amoroso S., Cao Z. (2021). *A New Dynamic Cone Penetration Test-Based Liquefaction Triggering Assessment of Gravelly Soils*. J. Geotech. Geoenviron. Eng., 147 (**12**), 04021141. https://doi.org/10.1061/(ASCE)GT.1943-5606.0002686

Rollins K.M., Roy J., Athanasopoulos-Zekkos A., Zekkos D., Amoroso S., Cao Z., Milana G., Vassallo M., Di Giulio G. (2022). *A New VS-Based Liquefaction-Triggering Procedure for Gravelly Soils*. J. Geotech. Geoenviron. Eng., 148 (**6**), 04022040. https://doi.org/10.1061/(ASCE)GT.1943-5606.0002784

Roy J., Rollins K.M. (2022). *Effect of hydraulic conductivity and impeded drainage on the liquefaction potential of gravelly soils*. Can. Geotech. J., 59 (**11**). https://doi.org/10.1139/cgj-2021-0579

Salvatore N., Pizzi A., Rollins K.M., Pagliaroli A., Amoroso S. (2022). *Liquefaction assessment of gravelly soils: the role of in situ and laboratory geotechnical tests through the case study of the Sulmona basin (Central Italy)*. Ital. J. Geosci., 141 (**2**), 216-229, https://doi.org/10.3301/IJG.2022.18

Salvatore N., Pagliaroli A., Brando G. (2025). *A Novel Quantitative Approach for Multi-hazard Risk Assessment of Linear Infrastructure: a Geological-Geotechnical Index*. Int. J. Bridge Eng., Manage. Res., 2 (**2**), 21424000. https://doi.org/10.32604/ijber.2025.00024

Sanò T. (1996). *BESOIL, Un programma per il calcolo della propagazione delle onde sismiche*. Servizio Sismico Nazionale, rapporto tecnico ssn/rt.

Schnabel P., Bolton Seed H., Lysmer J. (1972). *Modification of seismograph records for effects of local soil conditions*. Bulletin of the Seismological Society of America. 62 (**6**), 1649-1664. https://doi.org/10.1785/BSSA0620061649

Seed H.B., Idriss I.M. (1971). *Simplified Procedure for Evaluating Soil Liquefaction Potential.* Journal of the Soil Mechanics and Foundations Division, 97 (**9**).https://doi.org/10.1061/JSFEAQ.0001662

Sica S. (2001). *Analisi dinamica di dighe in terra.* Dottorato di Ricerca in Ingegneria Geotecnica, Consorzio delle Università di Roma la Sapienza e Napoli Federico II, pp 276.

Stein S., Wysession M. (2003). *An Introduction to Seismology, Earthquakes, and Earth Structure*. Blackwell Publishing, Oxford, UK. 507 pp. ISBN 0-86542-078-5

Stucchi M., Meletti C., Montaldo V., Crowley H., Calvi G.M., Boschi E. (2011). *Seismic Hazard Assessment (2003–2009) for the Italian Building Code*. Bulletin of the Seismological Society of America, 101 (**4**), 1885–1911. https://doi.org/10.1785/0120100130

Sun K., Xu J., Tian Y. (2023). *Dynamic behavior investigation of reinforced concrete bridge under multi-hazard effect of rockfall impact and material corrosion*. Structures, 58, 105557. https://doi.org/10.1016/j.istruc.2023.105557

Tilloy A., Malamud B.D., Winter H., Joly-Laugel A. (2019). *A review of quantification methodologies for multi-hazard interrelationships*. Earth-Science Reviews, 196, 102881. https://doi.org/10.1016/j.earscirev.2019.102881

Tosun J., Howlett M. (2021) *Managing low onset events related to climate change: the role of public bureaucracy*. Curr. Opin. Environ. Sustain, 50, 43-53. https://doi.irg/10.1016/j.cosust.2021.02.003

Tsuchida H., Hayashi S. (1971). *Estimation of liquefaction potential of sandy soils*. Proceedings of the 3rd Joint Meeting, US‑Japan Panel on Wind and Seismic Effects, May 1971. UJNR, Tokyo, 91-109

Twiss R.J., Moores E.M. (2007). *Structural Geology*. W.H. Freeman and Company, New York, NY, USA. 742 pp. ISBN 978-0-7167-4951-6

UNCED (1992). *Agenda 21*. United Nations Conference on Environment & Development, Rio de Janeiro, Brazil, 3 to 14 June 1992

UNISDR (2017). *UNISDR Annual Report 2017*. United Nations Office for Disaster Risk Reduction, Geneva, Switzerland, 62 pp.

Verrucci L., Pagliaroli A., Lanzo G., Di Buccio F., Biasco A.P., Cucci C. (2022). *Damping formulations for finite difference linear dynamic analyses: Performance and practical recommendations*. Computers and Geotechnics, 142, 104568. https://doi.org/10.1016/j.compgeo.2021.104568

Wang, W. (1979). *Some findings in soil liquefaction*. Earthquake Engineering Department, Water Conservancy and Hydroelectric Power Scientific Research Institute. Beijing: pp. 1-17

Wang J., He Z., Weng W. (2020). *A review of the research into the relations between hazards in multi-hazard risk analysis*. Natural Hazards, 104, 2003-2026. https://doi.org/10.1007/s11069-020-04259-3

Worden C. B., Gerstenberger M. C., Rhoades D. A., Wald D. J. (2012). *Probabilistic Relationships between Ground-Motion Parameters and Modified Mercalli Intensity in California*. Bulletin of the Seismological Society of America, 102 (**1**), 204–221. https://doi.org/10.1785/0120110156

Xie R., Fan W., Liu B., Shen D. (2020). *Dynamic behavior and vulnerability analysis of bridge columns with different cross-sectional shapes under rockfall impacts*. Structures, 26, 471–486. https://doi.org/10.1016/j.istruc.2020.04.042

Yeats R.S., Sieh K., Allen C.R. (1997). *The Geology of Earthquakes*. Oxford University Press, Oxford, 568 pp. ISBN 978-0195078275

Youd T.L., Idriss I.M. (2001). *Liquefaction Resistance of Soils: Summary Report From the 1996 NCEER and 1998 NCEER/NSF Workshops On Evaluation of Liquefaction Resistance of Soils.* J. Geotech. Geoenviromental Eng., 127 (**4**). https://doi.org/10.1061/(ASCE)1090-0241(2001)127:4(297)

Youd T.L. (2018). *Application of MLR Procedure for Prediction of Liquefaction-Induced Lateral Spread Displacement*. J. Geotech. Geoenviron. Eng., 144(**6**), 04018033. https://doi.org/10.1061/(ASCE)GT.1943-5606.0001860

Zaghi A. E., Padgett J. E., Bruneau M., Barbato M., Li Y., Mitrani-Reiser J., McBride A. (2016). *Establishing Common Nomenclature, Characterizing the problem, and Identifying Future Opportunities in Multihazard design*. J. Struct. Eng., 142 (**12**). https://doi.org/10.1061/(ASCE)ST.1943-541X.0001586

Zhang G., Robertson P.K., Brachman R.W.I. (2002). *Estimating liquefaction-induced ground settlements from CPT for level ground*. Can. Geotech. J., 39, 1168-1180. https://doi.org/10. 1139/T02-047

Zhang G., Robertson P.K., Brachman R.W.I. (2004). *Estimating Liquefaction-Induced Lateral Displacements Using the Standard Penetration Test or Cone Penetration Test*. J. Geotech. Geoenviron. Eng., 130 (**8**), 861-871. https://doi.org/10.1061/(ASCE)1090-0241(2004)130:8(861)

Zhu J., Daley D., Baise L.G., Thompson E.M., Wald D.J., Knudsen K.L. (2015). A Geospatial Liquefaction Model for Rapid Response and Loss Estimation. Earthquake Spectra, 31 (3). https://doi.org/10.1193/121912EQS353M

Zhu J., Baise L.G., Thompson E.M. (2017). An Updated Geospatial Liquefaction Model for Global Application. Bull. Seismol. Soc. Am., 107 (3). https://doi.org/10.1785/0120160198

Zuzak C., Mowrer M., Goodenough E., Burn J., Ranalli N., Rozelle J. (2022). The national risk index: establishing a nationwide baseline for natural hazard in the US. Natural Hazards, 114, 2331-2355. https://doi.org/10.1007/s11069-022-05474-w